Bioengineered Tissue Mechanics: Experimental Characterization and a Multi-Component Model

A DISSERTATION
SUBMITTED TO THE FACULTY OF THE GRADUATE SCHOOL
OF THE UNIVERSITY OF MINNESOTA
BY

Kwok Yin Victor Lai

IN PARTIAL FULFILLMENT OF THE REQUIREMENTS
FOR THE DEGREE OF
DOCTOR OF PHILOSOPHY

Professor Victor H. Barocas, Professor Robert T. Tranquillo

August 2013

Acknowledgments

To my parents: Thank you for the huge sacrifices you made so that I could pursue my dreams of graduate school (and life) in the US. I know this was not an easy decision, I am forever grateful for this opportunity you have given me.

To my advisors, Dr. Victor Barocas and Dr. Robert Tranquillo: I could not have asked for two better co-advisors. Thank you for taking the big risk of accepting someone without a biology or computational background to this research project, and having the faith in me to excel under such circumstances. I hope I have done you proud. Both of you have profoundly impact my life, not just academically and professionally, but also in life, through my personal interactions with you. It has indeed been a great honor to have been mentored by you – thank you.

To the folks in the Barocas and Tranquillo groups, both past and present: Thank you all for being an integral part of my life over the past 5 years. I have enjoyed immensely the opportunities to interact with each and every one of you. Special mention to Dr. Faisal Hadi and Dr. Sara Jouzdani – two amazing individuals who journeyed with me through the highs and lows of graduate school life. Also, to Dr. Spencer Lake: not only have I learned much from you professionally, but am also very thankful for our friendship.

To my friends and family here in the US: thank you for all your love and support over the years; this work would not have been possible without all of you. To the Burchell family: thank you for "adopting" me as one of your own. It means a lot to me to have a family here, to have a safe and quiet place to go home to when I need rest, and a family to spend the holidays with. Also, thank you to the folks in my bible study, who have repeatedly (and patiently) helped me to keep things in perspective when I was stressed out.

Lastly, but most importantly, to God be the glory. This work is possible only because of the gifts and talents God has given me. I pray that I was always be humbled by His blessings in my life and His love for me on the Cross, and never grow arrogant from any success.

Abstract

In the last few decades, tissue engineering has emerged as an interdisciplinary field of research which holds much promise as a complement to clinical medicine towards the overall improvement of personal health. Despite significant advances in this field, much work in TE continues to rely on an Edisonian approach of employing *ad hoc* methods to engineer tissues with desired properties without fundamental knowledge of the problem at hand. This thesis presents the development of a comprehensive model that predicts the mechanical properties of bioengineered tissue equivalents (TEs) based on its structure and composition, to enhance the understanding of the contribution of various biological components (e.g. biopolymeric fibers, cells, etc) to macroscopic mechanical properties of a tissue at different stages of tissue growth. The project framework considered bioengineered tissues as being composed of three components: fibrous networks, an interstitial matrix, and cells. The following interactions between different components were investigated: (a) multiple fiber networks, (b), fiber network + interstitial matrix, and (c) fiber network + cells.

Experimentally, mechanical tests such as stress relaxation and tensile stretch to failure were coupled with electron microscopy, confocal microscopy, and biochemical analyses to probe tissue microstructure and composition. Constructs were formulated with varying compositions of the different components in a TE. These experimental results guided the development of the theoretical model. Modeling work built upon an existing single-component microstructural model by incorporating other components and morphological features as observed from experiment. Improvements to the model combined two approaches: (1) a microstructural approach via incorporation of morphological features observed from micrographs, and (2) a phenomenological approach using constitutive relations commonly employed for various biological structures. Model validation was done by comparing model predictions of mechanical behavior with experimental results; agreements and discrepancies alike shed insight into the complex interactions between different components the comprise a TE. Overall, the work presented in this thesis represented significant improvements to the predictive capabilities of our computational model, and established the foundation for further modifications to capture better the microstructure and mechanics of different components within a TE.

Table of Contents

iii

List of Tables

List of Figures

1. Introduction

Tissue engineering, formally defined as "an <u>interdisciplinary</u> field that applies the principles of engineering and life sciences toward the development of biological substitutes that restore, maintain, or improve tissue function or a whole organ [1]," has become an attractive area of research which holds enormous potential for advances in the field of regenerative medicine and improvement of personal health. More recently, the notion of functional tissue engineering has emerged, combining the goals of biocompatibility with tissue functionality [2]. These twin goals serve as the guiding principles for *in vitro* development of soft tissue replacements such as blood vessels, heart valves, skin and cartilage. While significant advances have been made on the research and development of clinically significant products, important gaps in the fundamental knowledge underlying tissue engineering still exist. One such deficiency is in understanding how the macroscopic mechanical properties of bioengineered tissues are governed by its microstructure. Often, the microstructure of a native or bioengineered tissue is a complex arrangement of several different components (e.g. collagen) that interact with each other to give a tissue its overall properties. It is well known that the mechanical function of an engineered tissue is inextricably linked to tissue structure. For example, in engineered valvular constructs, replicating alignment properties of native valves is essential in achieving mechanical strength required for their desired

Tissue Level (10⁻²m) **Cellular Level (10⁻⁴m)** **Microstructural Level (10⁻⁶m)**
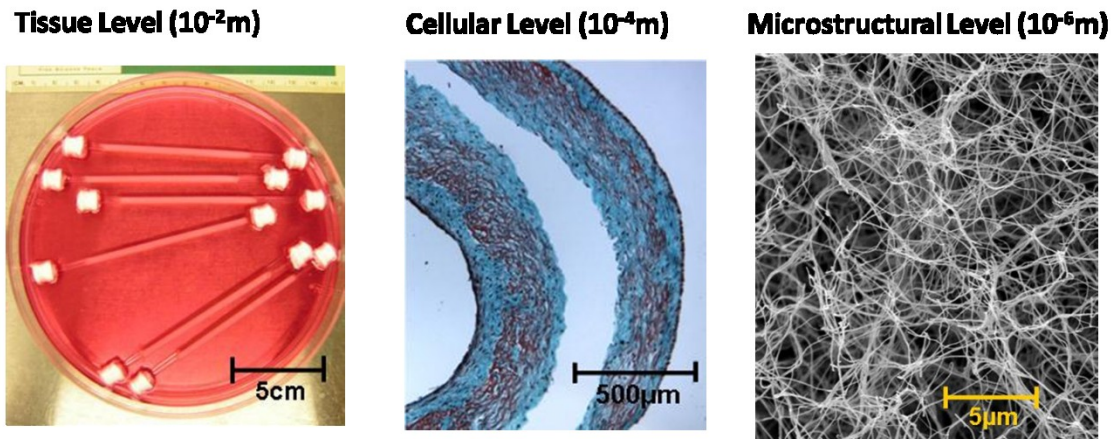
Figure 1-1. Representative images of a bioengineered tissue at different length scales. Left: tissue equivalents of bioengineered arteries. Middle: Histological image showing the various components in a tissue equivalent: collagen (red), fibrin (blue), and cells (black). Right: SEM image of a collagen network. Our goal is to relate structure and composition at the cellular and microstructural level to overall properties on the tissue level.

functionalities [3,4]. Microstructural complexities are further compounded by the dynamic cell interactions with the extracellular matrix (ECM), which is composed of fibrous networks such as collagen. The fundamental challenge for functional tissue engineering lies in understanding how structure and composition translates to overall macroscopic properties of the engineered tissue (Figure 1-1). To meet this need,

The purpose of this research is to develop a comprehensive model to predict the overall mechanical properties of an engineered tissue based on structure and composition.

Prior to describing our proposed work, we will briefly review current methods used in tissue engineering.

Current Methods In Tissue Engineering

In general, bioengineered tissues (also known as tissue equivalents (TE)) are composed of three main components: fibrous networks (or ECM), cells, and an interstitial material containing other biomacromolecules such as glycosaminoglycans. The

fundamental process in fabricating bioengineered tissues involves entrapping cells within a three-dimensional polymeric scaffold of either natural biopolymers (such as Type I collagen) or synthetic polymers (such as poly(L-lactic) acid [5]), and inducing cellular remodeling of the tissue via chemical or mechanical stimulants. Natural biopolymers offer several advantages over synthetic polymers, such as having natural binding sites for cells and enzymatic mechanisms that promote growth and remodeling of the overall tissue equivalents. Our group [6] and others [7,8] use fibrin as the starting scaffold for fabricating tissue equivalents. Fibrin is the main component found in blood clots; during the wound-healing process, fibrin clots are slowly degraded and replaced with cell-derived ECM. When fibrin is used as the starting scaffold material, a process much akin to the wound-healing process occurs, whereby the fibrin network is degraded and entrapped cells replace the underlying matrix with newly-synthesized collagen. In addition to the dynamic remodeling of the underlying ECM, cells also exert forces on the surrounding matrix that result in compaction of the overall tissue, which increases its overall strength and stiffness. While development of a TE with mechanical properties comparable to native tissue is a crucial step in conferring functionality, a majority of tissue engineering studies do not have a systematic method to predict the overall mechanical properties of a TE as the tissue undergoes growth and remodeling. In many cases, understanding of structure-function relations is limited to qualitative conclusions drawn by correlating mechanical data with compositional results from histology and biochemical analysis [9,10]. As a result, there is little understanding of how the structure and composition of a TE affect its overall mechanical function.

3
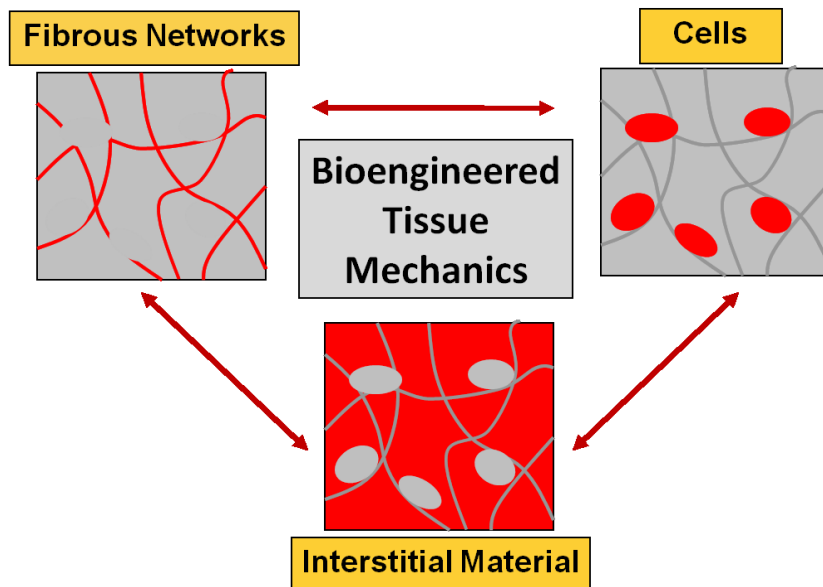
Figure 1-2. Schematic representation of the project framework. The central hypothesis is that the overall mechanics of a bioengineered tissue can be predicted by considering direct contributions of each component and the interactions between them. Experiments on tissue equivalents will be complimented with theoretical modeling to better understand the contributions of respective components to overall tissue properties.

Early notable works in developing predictive structural models of tissues include those by Lanir [11], who modeled tissues as fibers within a continuous interstitial matrix. More recently, several groups such as those led by Zahalak [12] and Elson [13] have developed models for cells entrapped within a continuous matrix. Our group has developed a micro-model of a single-component network to predict engineered tissue mechanics [14]. Despite these advances in modeling, much work remains to be done to accurately capture the complexities and dynamic changes involved in the growth and remodeling processes in engineered tissues.

This project framework is comprised of the three main components that make up a bioengineered tissue (Figure 1-2). The central hypothesis is that the overall mechanics of a bioengineered tissue can be predicted by considering direct contributions of each component and the interactions between them. The critical areas investigated in this

4

thesis, aimed at better understanding structure-function relationships in bioengineered tissues and improving the predictive capabitilies of our model, are described in further detail below.

Multiple Fiber Networks: The ECM of TEs consists of a mixture of collagen and fibrin at different compositions at various intermediate stages of tissue growth. Chapters 2 and 3 involved a combination of experimental and computational work to investigate structure-function-composition relationships in acellular collagen-fibrin co-gels. Tensile mechanical properties obtained from uniaxial tensile tests were correlated with collagen/fibrin microstructure probed from scanning electron microscopy and confocal microscopy. Possible interactions between the collagen and fibrin networks were explored computationally via modification of an existing microscale network to include of a second network, and comparing experimental data with model predictions.

Fiber Network + Interstitial Matrix: In collaboration with Dr. Mark Shephard at Renssellaer Polytechnic Institute (RPI), the effects of fiber network / interstitial matrix interactions were studied via comparison between simulation results from a lumped ("parallel") model, and a microstructurally coupled model (Chapter 4). In addition, Chapter 5 outlined the successful development of a collagen-hyaluronic acid TE to induce pre-stress within a collagen network, to replicate the *in vivo* stress state of many native tissues.

Fiber Network + Cells: Chapter 6 represented a major improvement to our multiscale model by the inclusion of a major component of tissues: cells. Simulation results using our multiscale model were compared to analytical composite theory for rigid inclusions

within a homogeneous matrix [15]. Further improvements to cellular microstructure were made by simulating the actin network and addition of a cytosolic pressure, and the effects of the relative stiffness between the cell and extra-cellular matrix investigated.

2. Multiple Fiber Networks I: Model Development and Validation Using Collagen-Fibrin Co-Gels

The content of this chapter was published in the Journal of Biomechanical Engineering (Jan 2012) as *"Mechanical Behavior of Collagen-Fibrin Co-gels Reflects Transition from Series to Parallel Interactions with Increasing Collagen Content"*.

2.1 Introduction

Type I collagen and fibrin are important extracellular matrix proteins. Collagen I is the predominant load-bearing component in many tissues, such as skin and tendon, while fibrin provides mechanical strength and integrity in blood clots. In addition, these naturally occurring biopolymers are commonly used in tissue engineering applications [16–19] because of their biocompatibility and their ability to interact with cells and elicit functional cellular responses. In vivo, collagen and fibrin can be found together in granulation tissue during the wound healing process. In vitro, co-existence of reconstituted collagen and fibrin matrices/fibril networks is seen in our tissue-engineered heart valve and media tissue equivalents (TEs), as the embedded cells gradually degrade the initial fibrin matrix and replace it with cell-derived collagen [6,20]. Extensive work has been done on the mechanical properties of fibrin [21–24] and collagen I [25–29] matrices separately, but there have been few studies on collagen-fibrin composite systems investigating how the two fibril networks interact to give the co-gel its macroscopic mechanical properties. Notable work includes that of Stegemann and co-workers [8,30,31], who observed that cell-seeded collagen-fibrin matrices exhibited higher modulus but intermediate ultimate tensile stress compared to pure fibrin and pure collagen gels of the same overall protein concentration. However, the interpretation of

these results is complicated by the inclusion of cells. Earlier efforts investigating possible interactions between collagen and fibrin networks include a study [32] that found evidence suggesting chemical cross-linking between collagen and fibrin via Factor XIII, a plasma enzyme that crosslinks fibrin. These findings, however, were refuted by others [33,34] who were unable to replicate the results. Thus, in spite of considerable efforts, there remains incomplete understanding of how collagen and fibrin fibril networks interact to confer overall mechanical properties. As tissue engineers strive to design tissues with mechanical properties comparable to native counterparts by creating multi-component fiber networks (e.g. [8]), knowledge of such interactions is an important first step towards understanding better how multiple ECM components influence the mechanical strength and stiffness of the overall tissue, allowing for more rational choices of scaffold components and culture conditions into the design. For example, in our fibrin-based TEs, an understanding of how the tissue stiffness changes with remodeling allows us to predict better the amount of compaction occurring in the tissues, which impacts overall fiber alignment – a factor that is crucial for conferring anisotropic mechanical properties akin to native tissues. In this study, we employ a combination of experimental and computational techniques to characterize and predict the mechanical behavior of acellular collagen-fibrin co-gels. Experimentally, we formulated collagen-fibrin co-gels in Teflon ring molds at 9 different concentrations and performed tensile tests to failure to obtain material properties of ultimate tensile stress (UTS), tangent modulus, strain energy density and strain at failure. These experimental results were compared to computational predictions from two hypothetical models for the co-gel: (a) independent, non-interacting

networks ("parallel"), and (b) a single network of alternating collagen and fibrin elements ("series").

2.2 Materials and Methods

2.2.1 Preparation of Collagen, Fibrin, and Collagen-Fibrin Co-gels

Collagen gels were formed by reconstituting acid-solubilized rat-tail collagen Type I (Invitrogen, Carlsbad, CA, 5.0mg/mL) with an alkaline solution consisting of 1M NaOH (Sigma, St. Louis, MO) supplemented with 10x MEM (Sigma), 6% FBS (HyClone, Logan, UT), 200mM L-glutamine (Invitrogen), 0.1% penicillin-streptomycin (Invitrogen), and 250μg/mL fungizone (Invitrogen). To make fibrin gels, stock solutions of fibrinogen and thrombin were first prepared. Bovine fibrinogen (Sigma) was dissolved in 20mM HEPES buffer saline (Mediatech, Manassas VA; 1M stock diluted in 0.9% NaCl). A fibrinogen solution was made by mixing 1 part stock fibrinogen with 5 parts 20mM HEPES buffer saline. A thrombin/Ca^{2+} solution was made by supplementing 1x DMEM (Mediatech) with 2.5% of 25U/mL thrombin and 0.2% 2N Ca^{2+} (Sigma). Fibrin gels were formed by adding 2 parts fibrinogen solution to 1 part thrombin/Ca^{2+} solution.

Collagen-fibrin co-gels were made at seven different collagen concentrations by adapting the procedure developed in [8], at volumetric proportions of 12.5%, 25%, 37.5%, 50%, 62.5%, 75%, and 87.5% of collagen formulation. Appropriate amounts of each solution corresponding to the target collagen concentration were mixed in the following order: the alkaline solution was first mixed with the thombin/Ca^{2+} solution, followed by addition of fibrinogen solution, and lastly, the addition of the collagen I stock solution. All gel solutions were cast into Teflon annular ring molds (15.5mm OD,

11.5mm ID) and incubated overnight at 37°C. Actual concentrations of collagen and fibrin in the co-gels were determined via biochemical analysis (see below), and respective compositions were computed from these results.

2.2.2 Quantification of Collagen and Fibrin Concentrations

Collagen content in each of the collagen-fibrin co-gels was measured using the hydroxyproline assay [35]. Fibrin content was measured by digesting the collagen-fibrin samples with human plasmin (Sigma) and quantifying the amount of fibrin degradation product (FDP) using ELISA [36].

2.2.3 Scanning Electron Microscopy (SEM)

Sample preparation for SEM was performed as follows: gels were fixed with 2.5% glutaradehyde (Sigma), followed by post-fixation staining with 1% osmium tetroxide. The samples were sequentially dehydrated in 30%, 50%, 70%, 80%, and 95% ethanol solutions, and freeze-fractured in liquid nitrogen before a final dehydration step in 100% ethanol. The dehydrated gels were further dried using a Tousimis 780A critical point dryer (Tousimis Corp, Rockville, MD) before being mounted on aluminum shims and sputter-coated with platinum for 10 minutes. High resolution imaging was performed a Hitachi S-900 Field Emission Gun Scanning Electron Microscope (Hitachi High Technologies America Inc, Pleasanton, CA) at a beam voltage of 2kV.
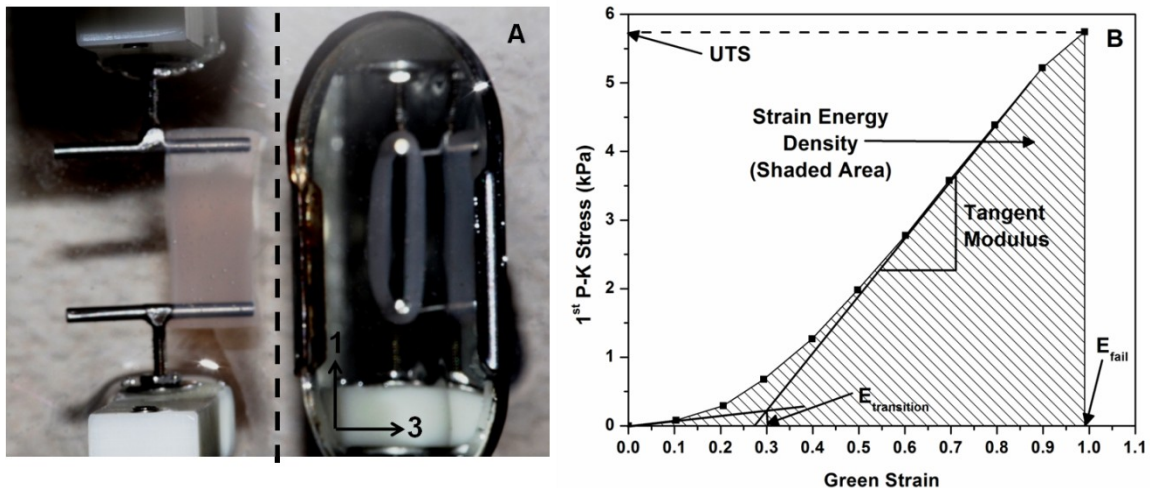
Figure 2-1. (A) Image showing the mechanical testing setup for collagen-fibrin rings, taken during pre-strain. A mirror (right of dotted line) is used to visualize the gel in the 1-3 plane. Dimensions of the gels are measured from these images to calculate the initial area, which is used to convert the force data to 1st Piola-Kirchhoff Stress. (B) Representative stress-strain plot of a collagen-fibrin co-gel (50%C), showing how each parameter is determined.

2.2.4 Mechanical Testing

Tensile tests to failure were performed on each gel ring using an Instron 8848 MicroTester (Instron, Norwood, MA) with a 5N load cell. The rings were mounted over T-bar grips looped through the annulus and were submerged in 1x PBS (Mediatech) throughout the duration of the test (Figure 2-1A). Each ring was initially stretched to a grip-to-grip length of 14.5mm for 5 seconds before stretching to failure at a strain rate of 0.13mm/s. The initial dimensions of the samples were captured using a digital camera during the 5-second pre-strain. Force-displacement data were converted to 1st Piola-Kirchhoff Stress (1st PK) versus Green's strain (E) to generate stress-strain curves for each sample. From the stress-strain profiles, the following quantities were computed and compared across compositions: ultimate tensile stress (UTS), Green strain at failure (E_{fail}), toe-to-linear transition ($E_{transition}$), tangent modulus, and strain energy density

11

(Figure 2-1B). The apparent Poisson's ratio at a stretch ratio of 1.5 was also computed for each co-gel using the following expression [37]:

$$\nu = -\frac{\ln \lambda_2}{\ln \lambda_1} \qquad (2\text{-}1)$$

Where λ_1 and λ_2 are the stretch ratios in the 1 and 2 directions respectively, as defined in Figure 2-1A. λ_2 was calculated using gel widths in the 2-direction, obtained from digital images taken at test points when $\lambda_1 = 1.0$ (start of test) and $\lambda_1 = 1.5$. The non-linear expression of equation 1-1 reduces to the standard definition of Poisson's ratio at infinitesimal strain, but remains equal to 0.5 for incompressible materials even at large strain.

2.2.5 Computational Model

We previously developed a multi-scale modeling framework that incorporated a single-component microstructural network to predict the overall mechanical properties of an engineered tissue [14,38,39]. Briefly, the model couples the macroscopic scale (representing the functional tissue level) with the microscopic scale (representing the fiber network) via volume-averaging. Each Gauss point of the finite element mesh is surrounded by a representative volume element (RVE), which defines the fiber network. Force balances within each RVE are solved instead of a stress-strain constitutive equation. On the microscopic scale, each RVE contains a network of randomly oriented fibrils. A fibril is defined as the straight line segment between two cross-links, and its mechanical behavior is described using an exponential force-strain constitutive relation [4,40]:

12

$$F = \frac{A}{B}\left(exp(BE_f) - 1\right)$$
<div align="right">(2-2)</div>

where F is the force on the fiber, and A, B are material constants representing the fiber. The pre-exponential constant A is a measure of the stiffness of the fiber, while B represents the degree of non-linearity of the fiber. E_f is the fiber Green strain computed from its fiber stretch ratio λ_f:

$$E_f = 0.5\left(\lambda_f^2 - 1\right)$$
<div align="right">(2-3)</div>

It should be emphasized that E_f is the Green strain of *individual fibers* in the RVE. As fibers rotate into the direction of stretch, a distribution of fiber Green strains will be obtained, with the largest possible value of E_f corresponding to the macroscopic strain at the gel level, for fibers perfectly oriented in the stretch direction. The average Cauchy stress for each RVE, σ_{ij}, can be shown [39] to be given by

$$\sigma_{ij} = \frac{1}{V} \sum_{\substack{boundary \\ cross-links}} x_i F_j$$
<div align="right">(2-4)</div>

where V is the volume of the RVE, and x_i and F_j are the ith-component of the position and jth-component of the force exerted for each boundary cross-link respectively. A boundary cross-link is defined whenever a fibril intersects an RVE boundary. To relate the RVE scale to the macroscopic scale, a scale factor, x, is computed based on the total fiber volume and the fiber volume fraction (see [39] for derivation):

$$x = \sqrt{\frac{LA_f}{\theta_0}}$$
<div align="right">(2-5)</div>

where the numerator is the total fiber volume given by the product of total fiber length (L) with fiber cross-sectional area (A_f), and θ_0 is the fiber volume fraction.
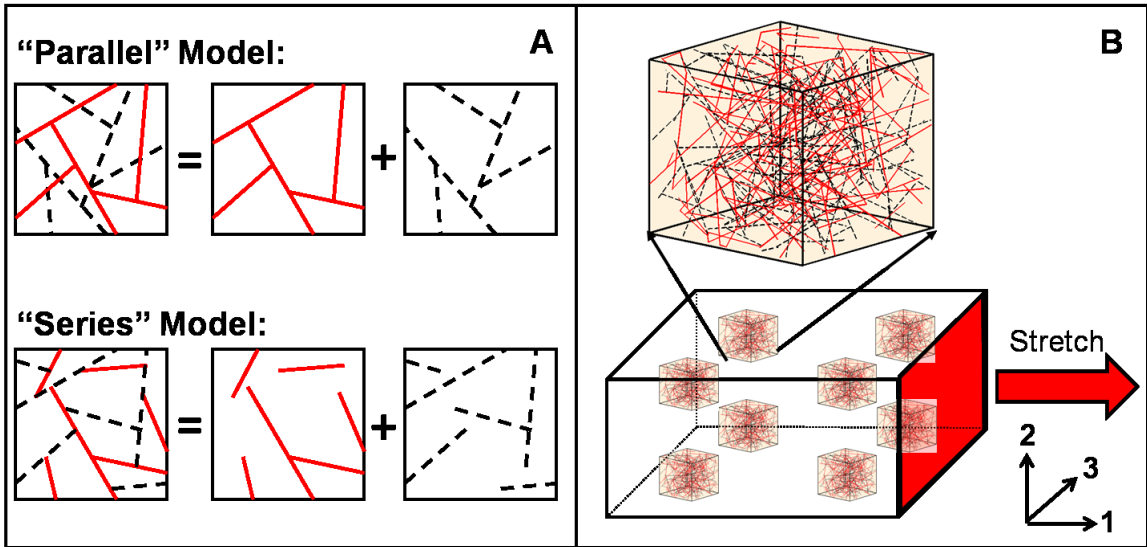
Figure 2-2. (A) Schematic representation of the parallel and series models of interactions in the two-network cases. (B) Model predictions of mechanical behavior in the networks generated using a single finite element with 8 Gauss points; each Gauss point is surrounded by a network RVE.

The strategy for modeling collagen-fibrin co-gels was as follows. Material constants *A* and *B* for collagen and fibrin were first determined by fitting theoretical predictions from our single-network model to experimental data for pure collagen and fibrin gels. We then modified our algorithm to model a two-network system and considered two different forms of interactions between the two networks (Figure 2-2A):

- Parallel Model: For the parallel model, the co-gel was modeled as two distinct, interpenetrating but not interacting networks. Two independent networks, one representing each component, were generated for each RVE, stress was calculated for each network independently, and the sum of the two component stresses was used as the stress of the co-gel. Differences in protein concentration (hence fiber volume fraction θ_0 in equation 2-5) were modeled by changing the scale factor *x* between each RVE and the macroscopic scale.

- <u>Series Model:</u> In the series model, the co-gel was modeled as a single network with some collagen and some fibrin fibrils. The two-component network was evaluated as a single interconnected network of randomly alternating collagen and fibrin fibrils, by randomly prescribing respective material constants *A* and *B* for collagen and fibrin to each fibril according to the desired compositions. Differences in concentration were modeled by adjusting the fraction of fibrils with each set of properties.

Because the ring test approximates simple uniaxial extension when, as in our study, the wall thickness of the ring is much smaller than its radius, a single finite element with 8 Gauss points was used to model this simple tensile test (Figure 2-2B), using RVEs containing approximately 700 fibrils each. Model-predicted stress-strain curves were generated by stretching each element to the respective failure strains observed experimentally. The apparent Poisson's ratio was computed in a similar fashion to the experiment, averaged between the 1-2 and 1-3 directions (as defined in Figure 2-2B). Because each network RVE was generated in a random manner, different networks of the same composition gave slightly different mechanical behavior. For each composition, at least 6 networks were generated, and averaged data were computed from the model results.

2.3 Results

2.3.1 Biochemical Results and SEM

Figure 2-3 shows a comparison between actual fibrin and collagen concentrations in the gels compared to expected concentrations calculated from our stock concentrations of fibrinogen and collagen. In general, with the exception of the pure fibrin gels (0%C),
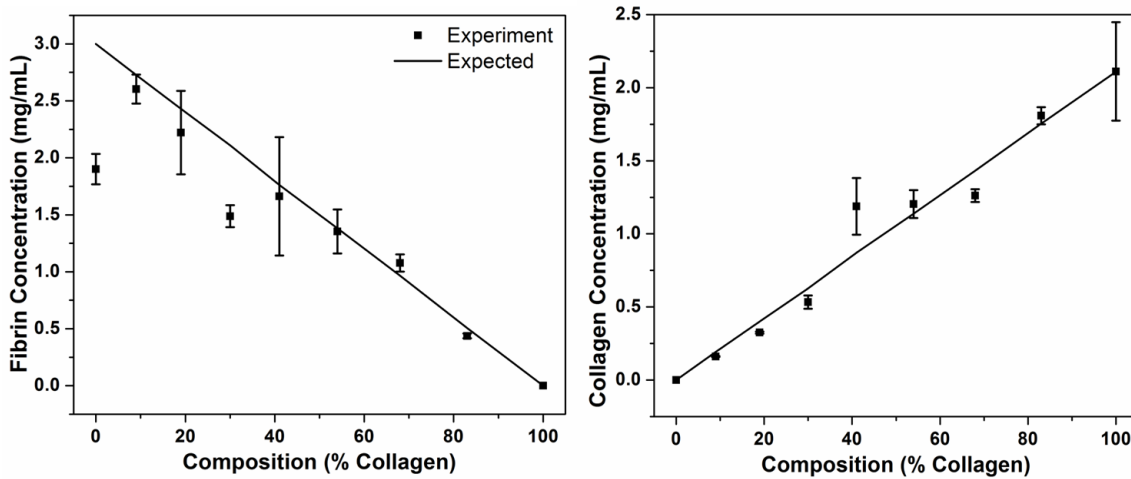
Figure 2-3. Results from ELISA and hydroxyproline assays to quantify fibrin and collagen concentrations respectively in the gels. In general, no significant loss in either fibrin or collagen is observed in the co-gels. A significant loss in fibrin is observed in the pure fibrin gels; this loss is also observed macroscopically in gel shrinkage and left-over liquid (containing unaggregated fibrinogen) when removed from the Teflon molds.

there was good agreement between the actual and expected fibrin and collagen concentrations, which indicates no significant loss of either protein in the co-gels during the casting process. The difference between the expected fibrin concentration (3mg/mL) and the actual concentration (1.9mg/mL) in the pure fibrin gels was also usually observed, where there was significant liquid loss and gel shrinkage when pure fibrin gel samples were removed from the Teflon molds. This protein loss was due to unaggregated fibrinogen left in the liquid. From these experimental data, the compositions of the 7 co-gels were calculated to be 9%, 19%, 30%, 41%, 50%, 68% and 83% collagen respectively. An expected linear decrease in total protein concentration with increasing collagen content was observed, as the co-gels were made by mixing volumetric proportions of 2.1mg/mL collagen formulation with 3.0mg/mL fibrin formulation.

SEM images of the fibrin and collagen gels (Figure 2-4) showed similar network microstructure between the pure networks, with fibril diameters on the order of 100nm.

16
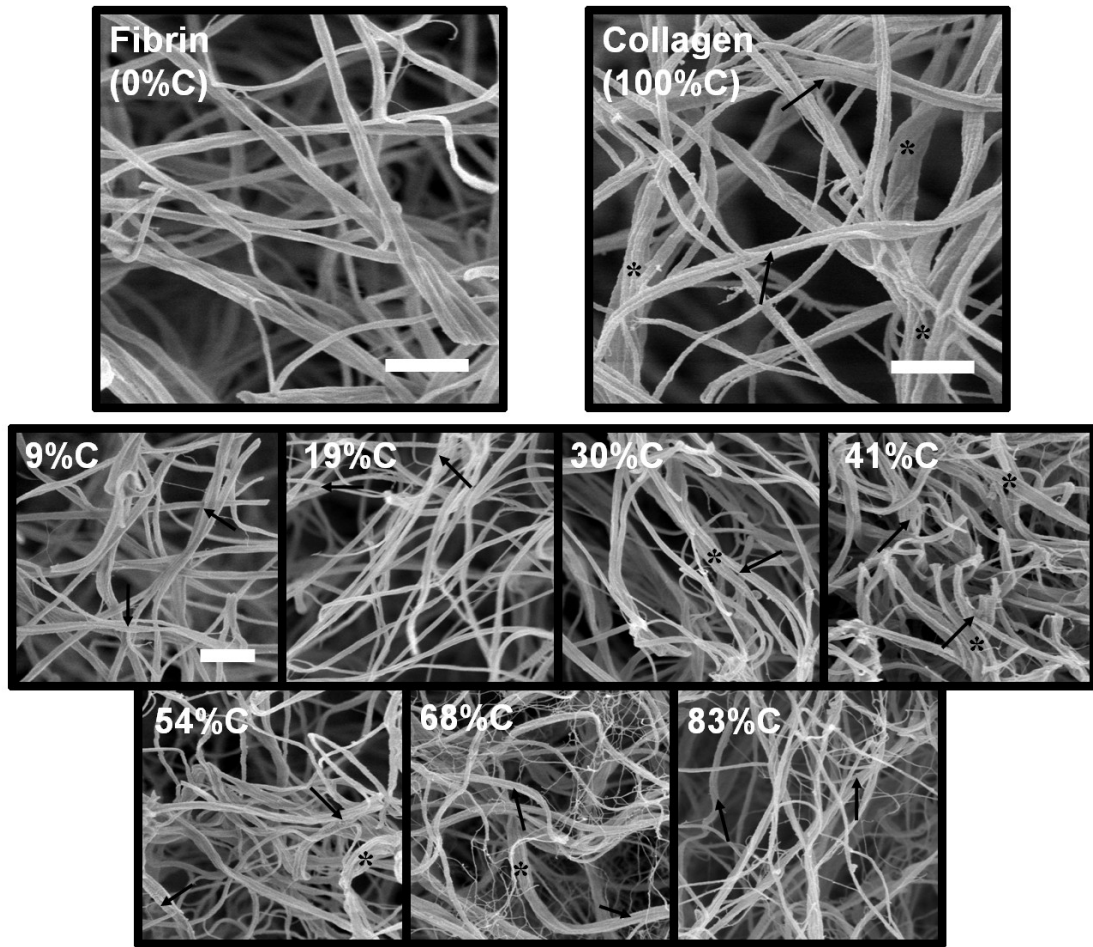
Figure 2-4. SEM images taken at 30,000x of pure fibrin and collagen gels (top) and collagen-fibrin co-gels (bottom). Collagen fibers can be differentiated from fibrin fibers by their characteristic banding pattern (arrows) on and bundling of (*) the fibers. At higher collagen compositions (68%C, 83%C), wispier, web-like fibrin structures are observed. Scale bars = 1 μm; scale bar in 9%C image representative for all co-gel images.

Characteristic banding patterns of collagen fibrils can be observed in the collagen images (marked with arrows), as well as bundling of fibrils (marked with *) to form thicker collagen fibers. These two characteristics of the collagen network, absent in the fibrin network, allow identification of collagen fibrils in the co-gels. It should be emphasized that while bundled and/or banded fibrils are collagen, the unbanded, unbundled fibrils could belong to either network. From the co-gel images, composite fiber networks comprised of interpenetrating collagen and fibrin fibrils can be seen, with more banded

17
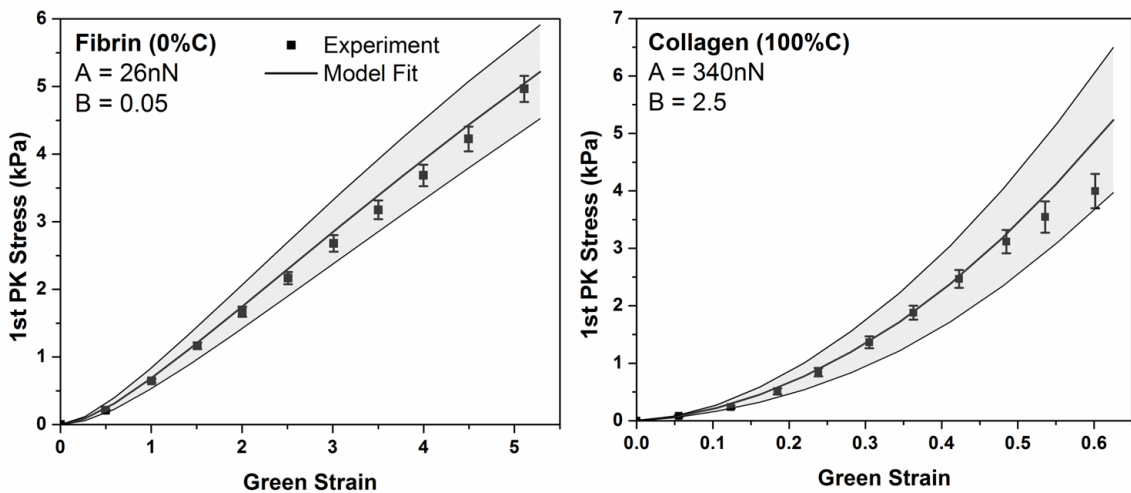
Figure 2-5. Model fits to experimental data to obtain material parameters *A* and *B* for fibrin and collagen respectively. Collagen shows much higher stiffness (in *A* value) and larger degree of non-linearity (*B* value) than fibrin. Error bars on experimental data represent 95%CI, n ≥ 7 for both collagen and fibrin. Error bands on model fits represent 95%CI, generated from 4 different networks for each.

and bundled fibrils observed with increasing collagen composition. At high collagen compositions (68%C and 83%C), a fine network of wispy fibers is observed to form around the thicker fibrils. Most of the thicker fibrils at these compositions appear banded, indicating that they are collagen; furthermore, fibrin is known to form such wispy structures depending on gelation conditions [7]. Hence the fine network seen at higher collagen compositions is likely to be fibrin. Collectively, these images confirm that a composite network of collagen and fibrin fibrils is formed in our co-gels; however, it should be noted that no inference on the *nature of interactions* between collagen and fibrin can be made from these images.

2.3.2 Mechanical Properties

Using the protein concentrations of the pure gels determined experimentally (1.9mg/mL for fibrin, 2.1mg/mL for collagen) and a fibril diameter of 100nm for both fibrin and collagen as observed from SEM images, the single-network model was fitted to
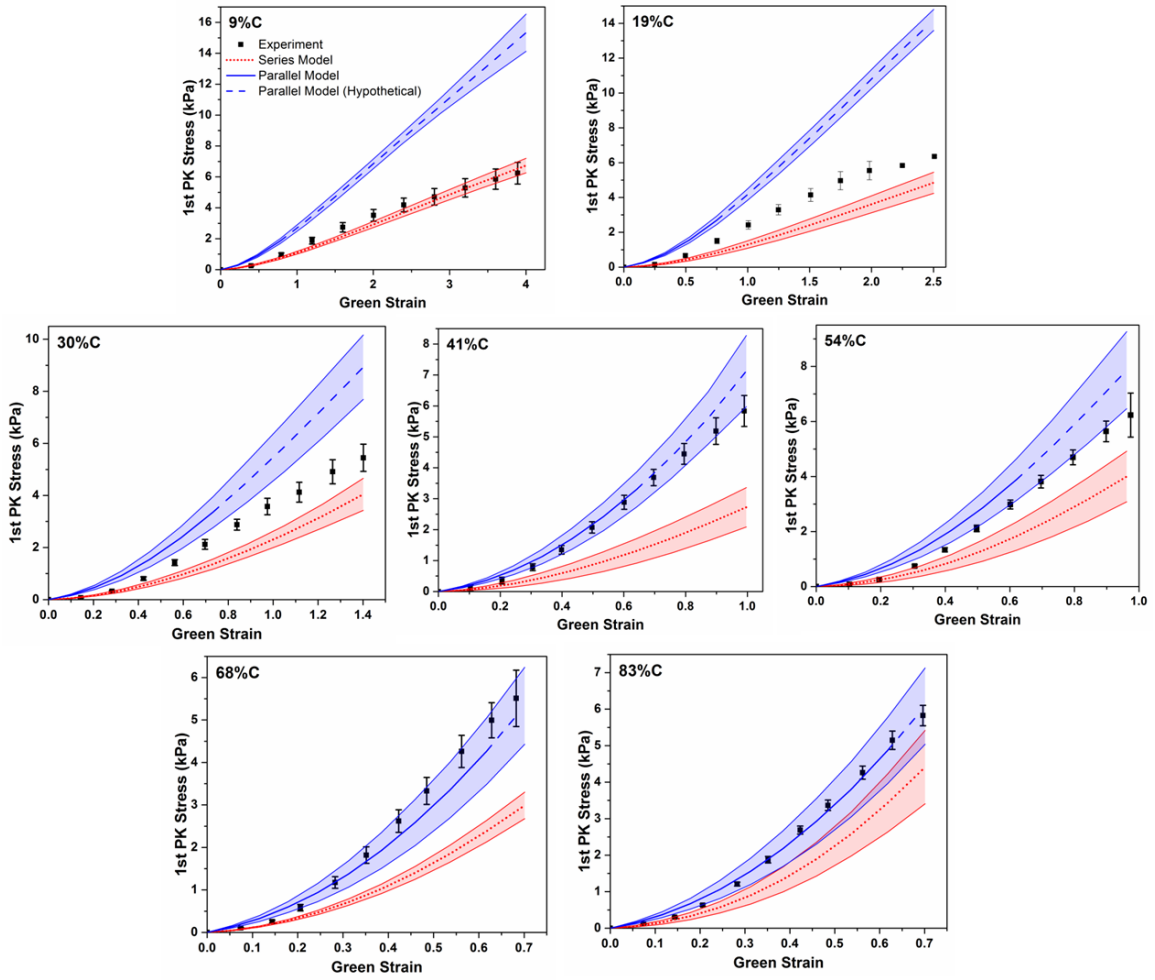
Figure 2-6. Model predictions from the parallel and series models compared with experiment (■) across all 7 compositions of co-gels. In the parallel model, the dashed lines represent hypothetical stress-strain regions after the failure strain of pure collagen, above which the collagen network is expected to have failed catastrophically. In all cases, the parallel and series models provide upper and lower bounds to the experimental data. The series model shows better agreement to experiment at low collagen content (9%C), while the parallel model shows better agreement at high collagen contents (68%C and 83%C). Error bars represent 95%CI; n ≥ 5 gels for experiments, n ≥ 6 networks for models.

experimental data to obtain material parameters *A* and *B* for idealized fibrin and collagen

fibers (Figure 2-5). The relative linearity of the stress-strain curve for fibrin is reflected in

the small fitted *B* value. This fit suggests that the mechanical behavior of fibrin fibrils is

largely linear; a small toe region in the overall stress-strain curve is still observed,

however, which arises from reorganization and rotation of the fibrils as the gel is
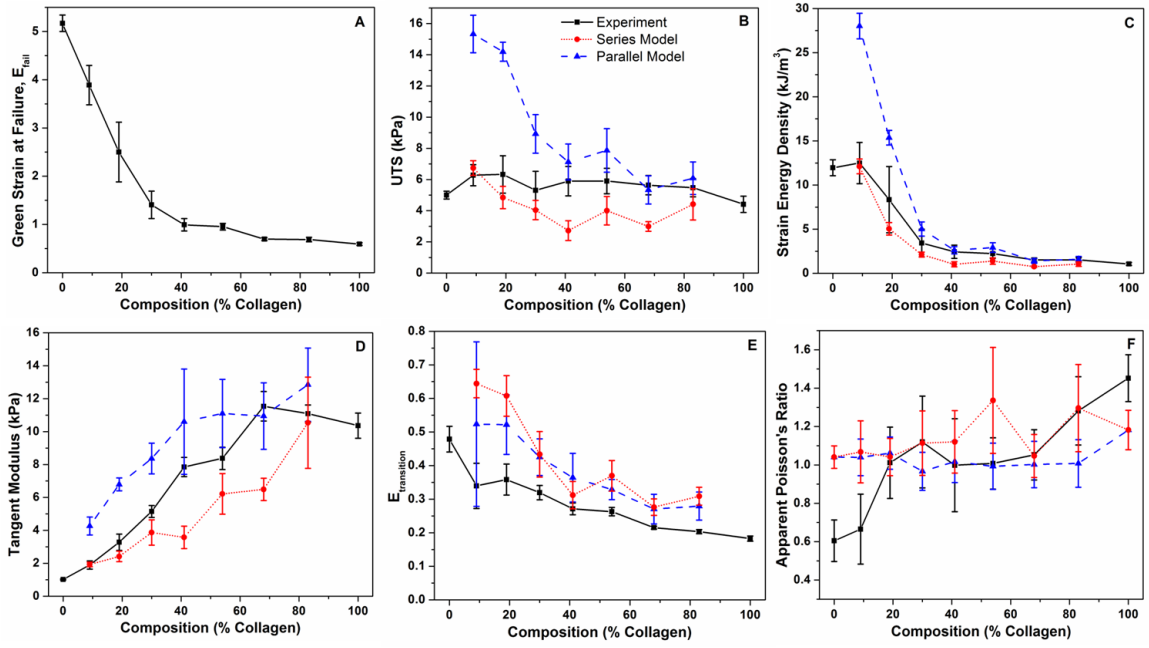
Figure 2-7. Material properties of co-gels from experiment (■, solid lines) compared with model predictions from the parallel (▲, dashed lines) and series (●, dotted lines) models. Parallel models reflect properties in the hypothetical region (defined in Figure 6) beyond the failure strain of collagen. In general, both models are able to predict trends in strain energy density, tangent modulus and transition strain. Experimental data is bracketed by the parallel and series models in UTS, strain energy density and tangent modulus. Models predict apparent Poisson's ratio on the same order of magnitude as experiment. Error bars represent 95%CI; n ≥ 5 gels for experiments, n ≥ 6 networks for models.

stretched. That collagen is a much stiffer fiber than fibrin (hence a larger *A* value) is

reflected in the similar stress scales for both fibers but much lower strain range for

collagen.

Using these fitted parameters for fibrin and collagen, model predictions for the

tensile behavior at the seven intermediate compositions were made using the parallel and

series models of interactions as explained above (Figure 2-6) and compared to sample

averaged stress-strain curves from experiment. At all compositions, the model elements

were stretched to the respective experimental strains at failure (Figure 2-7A) to simulate

the experiments. Dotted lines for the parallel model in Figure 2-6 represent hypothetical

20

model stress-strain behavior beyond the failure strain of a pure collagen network. These regions are physically unrealistic, since the collagen network in such a parallel network system would fail and could not continue to carry load. Across all compositions, the experimental curves were found to fall between or within the two models, with the parallel model providing the upper bound, and the series model the lower bound. At the lowest collagen co-gel concentration (9%C), the series model appears to capture the tensile behavior of the composite network well. A transition towards the parallel model occurs with increasing collagen content, such that a good agreement between the parallel model and experimental data was observed at high collagen concentrations of 68%C and 83%C.

A comparison of material properties of the co-gels across compositions extracted from experimental data is provided in Figure 2-7. In terms of failure behavior, a rapid decrease in strain at failure is observed as collagen content increases (Figure 2-7A), while UTS of the co-gels remain relatively constant across compositions (Figure 2-7B). Accordingly, strain energy density (Figure 2-7C) decreases while tangent modulus (Figure 2-7D) increases with increasing collagen composition. Similar to observations from the stress-strain curves, the experimental data for strain energy density, UTS, and tangent modulus were found to be bracketed by the parallel and series model predictions. Transition strain (Figure 2-7E) can be considered as an estimate of the amount of strain needed for the fibrils to reorganize, rotate, and straighten into the direction of stretch. While both the parallel and series models over-predict this transition strain, they are able to capture the general trend of decreasing transition strain with increasing collagen

composition (Figure 2-7E). Experimentally, the apparent Poisson's ratio (Figure 2-7F) exhibited an increasing trend from 0.6 to 1.5 as collagen content increased from 0% to 100% (p value < 0.05 for the null hypothesis that the slope of the linear regression equals zero). While the same regression analysis performed on both parallel and series models predicted constant apparent Poisson's ratios (i.e. p > 0.05 in both cases, such that the null hypothesis could not be rejected at the 95% confidence level) across all compositions, the values were of similar order of magnitude to experimental data.

2.4 Discussion

Analysis of experimental data coupled with model predictions provides insight into how mechanical properties change with composition and the forms of interactions that exist between fibrin and collagen in these co-gels. That fibrin is a very compliant biomaterial is well documented [41,42], and our results are consistent with these findings that fibrin networks can have extensibilities beyond 200%. Addition of collagen to fibrin led to intermediate mechanical properties (strain at failure, UTS, tangent modulus); non-linear trends with increasing collagen concentration showed that these properties could not be predicted by the simple rule of mixtures. As collagen content increased, the macroscopic stiffness of the gel increased at the expense of extensibility; however, failure was observed at strains well beyond the failure strain of pure collagen, an effect especially pronounced at low collagen concentrations. The lack of an abrupt transition in properties indicates that plastic failure of the stiffer collagen network did not occur in the co-gels. Additional experiments on 41%C co-gels, in which the gels were first pre-stretched to the failure strain of pure collagen, showed statistically similar failure

properties (UTS, strain at failure) to gels that were not pre-stretched, with a small effect (~15%) on tangent modulus (data not shown). These results further confirm absence of plastic failure in the stiffer collagen network. Collectively, these results suggest that the co-gels were not dominated solely by either network, but rather that complex interactions between the networks gave rise to intermediate properties. Complementary contributions to overall mechanical behavior by both networks occur in the co-gels: the fibrin network gives extensibility by bearing stretch, while the collagen network provides stiffness by bearing load.

Across all compositions, the collagen-fibrin co-gels exhibited large apparent Poisson's ratios above the incompressibility limit. Since these gels are largely composed of water (>99 vol%), it is not surprising that significant shrinkage occurs during stretch, where liquid is squeezed out of the gel between the fibrils as they rotate into the direction of stretch [43]. While an increase in apparent Poisson's ratio with increasing collagen composition is observed, it is unclear whether this effect is due to a decrease in fibril density with increasing collagen content in our co-gels, or fibrin is better able to retain water within its network. Similarly, it is unclear whether the decrease in transition strain with increasing collagen content is due to rotational hindrances from higher fibril densities, or an inherent non-linear behavior of the respective networks.

The conventional preparation techniques for SEM used in this study has been shown to introduce artifacts in the microstructure compared with cryo-SEM preparation techniques, such as substantial shrinkage of the sample resulting in smaller fibril diameters and smaller void spaces [44], and collapse and clumping of fibrils [45].

Nevertheless, our SEM images provide important information on the overall morphology of the co-gels at different concentrations, showing co-existing networks of collagen and fibrin in co-gels, as well as changes in fibrin network architecture at higher collagen concentrations. An average fibril diameter of 100nm based on our SEM images was used as input into our model to relate the RVE to the macroscopic scale in equation 2-5. While a different fibril diameter would quantitatively change the fitted material parameters A and B for collagen and fibrin, the key qualitative results from these model fits remain unchanged: that collagen is stiffer (larger A value) and exhibits a greater degree of non-linearity (larger B value) than fibrin. The effect of fibril diameter is fully subsumed in the alteration of A and B parameters – subsequent model predictions using these altered parameters will give the same qualitative and quantitative results as presented in this paper.

The parallel and series models presented here were meant as gross idealizations of interactions and were not intended to describe actual interactions in our co-gels. However, comparison of our simulations with experimental data provides some insight. Figure 2-8 illustrates differences in fibril stretch and fibril force distributions between the parallel and series models. In the parallel model, both networks experience equal stretches (Figure 2-8A), while the overall load is unevenly distributed between the networks according to their relative properties; hence, in this model, the overall mechanical behavior is largely dominated by the stiffer collagen network (Figure 2-8B). This phenomenon is demonstrated by the uncharacteristically high stresses observed when the parallel two-fiber networks are stretched beyond the failure strain of pure
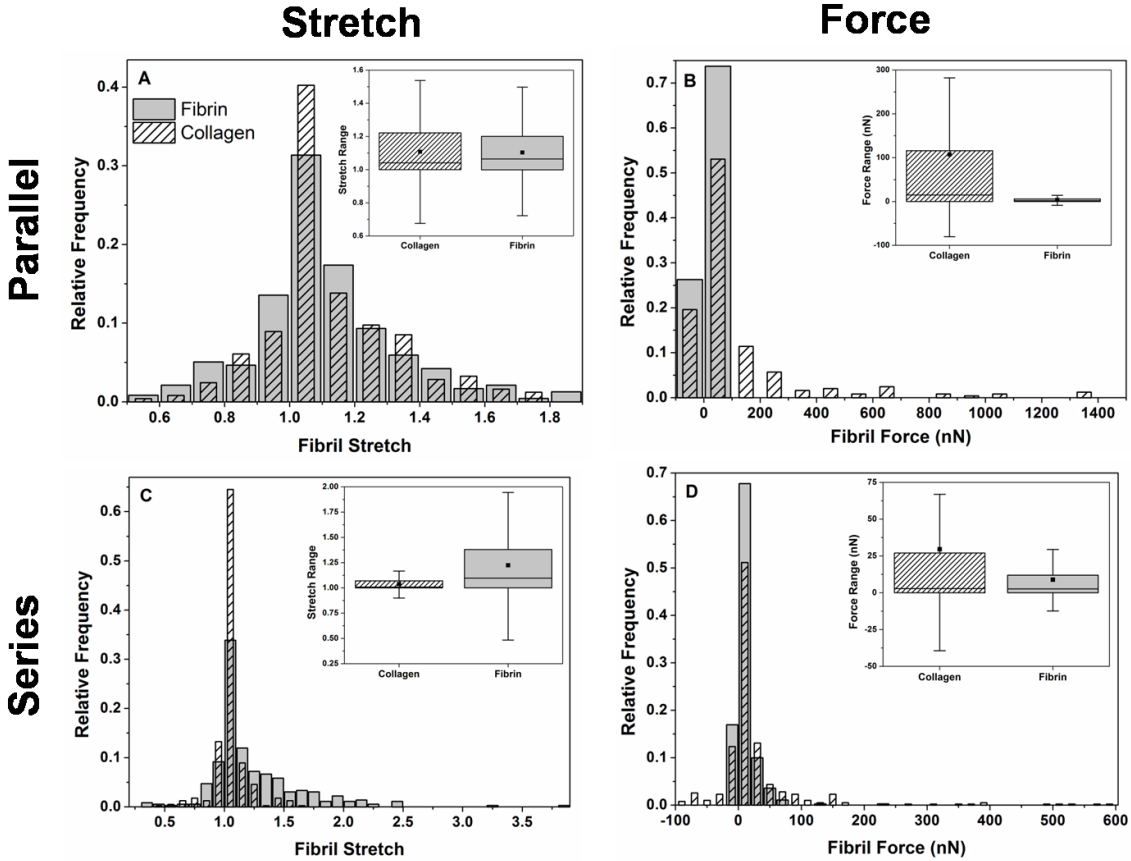
Figure 2-8. Fibril stretch and fibril force distributions in the parallel and series models after macroscopic stretch. In the parallel model, the collagen and fibrin networks exhibit similar fibril stretch distributions, but forces in the collagen fibrils are much larger than those in fibrin fibrils. In the series model, a much smaller difference between collagen and fibrin fibril force distributions is observed, but fibrin fibrils bear a larger proportion of macroscopic stretch. Distributions are of 54%C networks, taken from an RVE at a Gauss point after the final stretch step. ∎ in box plots represent distribution mean, whiskers represent outliers within the interquartile range.

collagen at low collagen content (9%C) in the hypothetical region (Figure 2-6, Figure 2-7B). In the series model, the macroscopic strain is disproportionately distributed among the two fibril populations according to their relative stiffness (Figure 2-8C), while the overall load is borne equally by fibrils from both networks (Figure 2-8D). While we are unable to observe definitively parallel-like or series-like interactions between collagen and fibrin fibrils from our SEM images, inferences can be made from comparison of our

25

model predictions with experimental data. At low collagen content, close agreement between experimental data and the series model suggests the sparse collagen fibrils do not form a percolating collagen network, but are dispersed among a fibrin-dominant network, i.e. "islands" of collagen fibrils are present in a series-like manner with the extensive fibrin matrix. While these sparse collagen structures contribute to overall gel stiffness, they bear a lower proportion of the strain such that macroscopically, the gel can be strained beyond the failure strain of pure collagen; the macroscopic strain of the gel is dominated by the fibrin network. At high collagen content (68%C and 84%C), the parallel model provides a good fit to the experimental data, suggesting a collagen-dominated network. In these cases where the gel is largely composed of the stiffer collagen network, the strain is dictated by this stiffer matrix. The overall mechanical behavior appears additive in a parallel-like fashion, where the smaller contribution to load-bearing by fibrin adds to that of the stiffer collagen network. In addition, the failure strain is largely dictated by the extensive collagen network, while the slight increase in the experimental failure strain may be attributed to sparsely distributed fibrin fibrils associated with the collagen network. At intermediate compositions, the parallel and series models provide bounds for the experimental data, which suggest a mixture of such interactions. Conceivably, both collagen and fibrin form respective independent interconnected networks in a parallel fashion, but individual fibrils from each network can be associated with each other across the networks, forming series connections. In addition, more inter-fibril mechanical connections may be formed as the gel is stretched and as fibrils from each network rotate and reorganize with each other. While our results

strongly indicate interactions between collagen and fibrin, it remains unclear whether these interactions are chemical (i.e. chemical bonds between fibrils) or mechanical (physically entangled fibrils) in nature. Work is in progress to understand the nature of these interactions by digestion of either network in the co-gels.

Previous studies on collagen-fibrin co-gels have focused on cellular responses (gel compaction, cell proliferation) on collagen-fibrin scaffolds of different compositions and concentrations for applications in cardiovascular tissue engineering [8,30]. Our work expands on these studies by exploring the fundamental structure-function-composition relationships in these collagen-fibrin composite networks, allowing a better understanding of the mechanical environments that cells experience in such tissue-engineered constructs. In addition, a progression in composition occurs in our tissue-engineered media equivalents (MEs): with cells initially seeded in a fibrin gel, the MEs undergo compositional changes during the growth and remodeling process, transitioning from a pure fibrin-based construct at casting to a largely collagen-based construct after weeks of culture [46]. That the cells in our MEs experience changes in the mechanical environment throughout the remodeling process may have implications on the cellular responses elicited at different stages of growth and remodeling.

One of the key goals in tissue engineering is to design tissue equivalents with mechanical properties comparable to the native tissues. Efforts towards this goal have included modifying or manipulating the ECM content, such as stimulating production of collagen to improve tissue strength and stiffness [6], or directly incorporating elastin to confer tissue compliance [17]. While tissue engineers understand the importance of

27

different ECM components towards overall mechanical behavior and function, our work emphasizes the *complexity of interactions* between multiple ECM components in conferring mechanical properties. This work is a step forward towards understanding better the complexities of how tissues behave mechanically due to the presence of various components within the tissue, allowing for more rational design for bioengineered tissues. In addition, a vast majority of multi-component models of native tissue mechanics (e.g. [47,48]) rely on parallel-type interactions, adding up contributions from the different components. Our results for the collagen-fibrin model system strongly suggest that alternative approaches may be needed for some tissues.

2.5 Conclusions

This current work offers new insights into how collagen and fibrin fibril networks interact with each other, and furthers the understanding of fundamental structure-composition-function relationships in collagen-fibrin co-gels. Comparison of model results with experiments suggests complex interactions between collagen and fibrin networks that vary with composition, with a series model bring better for collagen-poor gels and a parallel model better for collagen-rich gels. This study demonstrates that purely parallel (i.e. additive) models may not be adequate to describe tissue mechanics.

3. Multiple Fiber Networks II: Microstructure and Mechanics of Digested Collagen-Fibrin Co-Gels

The content of this chapter was published in Acta Biomaterialia (Nov 2012) as *"Microstructural and Mechanical Differences Between Digested Collagen-Fibrin Co-Gels and Pure Collagen and Fibrin Gels"*.

3.1 Introduction

Naturally occurring biopolymers such as collagen and fibrin play an important role in the physiological and mechanical function of various systems and processes in the human body. Collagen, the most abundant protein in the human body, is divided into many different types that are structurally distinct from one another, with type I being most prevalent [49]. Fibrin is the main matrix component found in a blood clot and early granular tissue during the wound healing process. These extracellular matrix (ECM) components are also commonly used as scaffolds for tissue engineering applications, including in combination with one another or other proteins, e.g. collagen-fibrin [8], collagen-elastin [17]. Understanding how various ECM components interact with each other to confer overall mechanical behavior is important in more rational design in tissue engineering. The choice of initial scaffold material(s) for seeding cells is a critical aspect in fabricating tissues with structural integrity and biochemical functionality akin to those of native tissues because cells respond differently according to their mechanical and biochemical environments. For example, our group has found that seeding vascular smooth muscle cells (SMCs) in a fibrin gel promotes cellular production of collagen I, hence improving the mechanical strength of the overall tissue equivalent (TE) [20]. Regardless of the initial choice of scaffold material, engineered tissues, like native

tissues, almost always contain a combination of different ECM components. For example, compositional changes in the ECM occur in fibrin-based constructs during the growth and remodeling process where the fibrin matrix is gradually degraded and replaced by a cell-derived collagen matrix [46,50,51], a process akin to wound healing. While the structure and mechanics of individual ECM components (e.g. collagen, fibrin, elastin) have been studied extensively [22,23,26,28,42,52–55], understanding of composite ECM systems is still lacking. Previous studies on interpenetrating network systems, both in synthetic polymer blends [56,57] and natural biopolymer [30,58,59] mixtures, have shown complex mechanical responses, indicating complex interactions between the networks that are not well understood.

Specifically for collagen-fibrin co-gels, previous studies on interactions between these two ECM components have reported conflicting results, with some [33,34] refuting the presence of chemical bonding between these proteins as reported in [32]. Our group is interested in understanding how network architectures and interactions in interpenetrating ECM systems influence overall mechanics and in developing a computational model that can adequately capture the mechanics of such systems based on their respective microstructural and mechanical details. That network morphology and mechanical behavior of *individual* collagen and fibrin networks can be altered by varying gelation conditions has been well documented. For fibrin, seminal studies by Ferry and co-workers investigated effects of fibrinogen and thrombin concentrations as well as pH, temperature and ionic strength of the solutions [60]; this work was followed by similar studies conducted by other groups, (e.g. [61–65]). More recent work by our group [66]

and others (e.g. [7,19,67,68]) has included studies with cells entrapped in the fibrin gel which are more relevant to tissue engineering. Similarly, studies performed on collagen gels have given insight into the effect of gelation conditions (e.g. temperature, pH) on the collagen microstructure and mechanics [26,69,70]. However, the mechanism by which fibrin and collagen network microstructure and mechanical behavior are changed when formed in the presence of each other, as well as how these ECM networks interact with each other to confer overall mechanical properties to engineered tissue, remains poorly understood. Collagen and fibrin have different gelation mechanisms. Fibrin assembly is initiated by thrombin-catalyzed cleavage of fibrinopeptides from fibrinogen, exposing sites for intermolecular associations between fibrinopeptides to form fibrils [71]. In contrast, collagen fibrils are formed by self-assembly of triple-helical proto-collagen molecules (on the order of 300nm in length) in a staggered formation [72]. Fibrin-collagen composite systems are relevant both physiologically (in the context of wound healing and atherosclerosis [73]) and in bioengineered tissues. Specifically in wound healing, collagen and fibrin play distinct roles: a fibrin clot forms a provisional matrix to stop bleeding, while the process of wound repair involves deposition of newly-synthesized collagen by fibroblasts [74]. Our previous work on collagen-fibrin co-gels [59] focused on the *composition-function* relationship between the two networks, showing non-linearity in mechanical behavior with increasing collagen concentration. In addition, comparison of mechanical behavior between experimental data and predictions from our computational model showed a transition in collagen-fibrin interactions from series behavior to parallel mechanical behavior as the volume fraction of collagen

increased. While the previous study gave some insight into how collagen and fibrin interact in co-gels, those results also raised the question of whether collagen and/or fibrin architecture changes when formed in the presence of each other, and how such changes in morphology alter the mechanics of the co-gels. The purpose of the current study is to investigate the effect of altering network architecture on collagen and fibrin mechanical properties, thereby elucidating *structure-composition-function* relationships between collagen and fibrin in co-gels. We hypothesize that the overall mechanics of collagen-fibrin co-gels is influenced not only by its composition, but also by changes in network architecture of both collagen and fibrin, arising from co-gelation with each other. Specifically, this study investigates changes in microstructure of collagen and fibrin when gelled individually (i.e. in its pure form without a secondary network present) compared to gelation in the presence of each other, and seeks to relate these microstructural changes to alterations in mechanical behavior. To do so, collagen-fibrin co-gels were formed and subsequently subjected to digestion to remove either collagen (with collagenase) or fibrin (with plasmin), while leaving the other network intact. The microstructure and mechanical behavior of these resultant networks were compared with those of their pure counterparts. Scanning Electron Microscopy (SEM) and confocal microcsopy to probe network morphology were coupled with tensile tests to failure to aid in understanding the mechanical behavior of these gels.

3.2 Materials and Methods

3.2.1 Preparation and Digestion of Collagen, Fibrin, and Collagen-Fibrin Co-gels

The methods for casting collagen, fibrin, and collagen-fibrin co-gels were adapted from [8]. Briefly, 1mL of collagen formulation was comprised of 660μL acid-solubilized rat-tail collagen type I (Life Technologies Corporation - Invitrogen, Grand Island, NY) neutralized with 26 μL of 1M NaOH (Sigma-Aldrich Co. LLC, St Louis, MO), supplemented with 100 μL 10x Minimum Essential Medium (MEM, Sigma-Aldrich), 60 μL fetal bovine serum (Thermo Fisher Scientific Inc. – Hyclone, Logan, UT), 10 μL L-glutamine (Invitrogen), and 1 μL each of penicillin-streptomycin (Invitrogen) and fungizone (Invitrogen). The fibrin formulation consisted of bovine fibrinogen (Sigma-Aldrich) dissolved in 0.02M HEPES buffer (Mediatech Inc, Manassas, VA) in saline (constituting 66% by volume of formulation), polymerized by mixing with a solution containing 0.83%vol thrombin, 0.06%vol Ca^{2+} (Sigma-Aldrich), and 33%vol of 1x DMEM (Mediatech). Collagen-fibrin co-gels ("CG") were made by mixing 50% by volume of collagen and fibrin formulation. To make pure collagen gels ("C") with the same collagen concentration as in the co-gels, the above collagen formulation was diluted with an equal amount of 0.5M HEPES buffer (Mediatech). Similarly, pure fibrin gels ("F") were made by diluting the fibrin formulation with an equal amount of 0.02M HEPES buffer. The gel solutions were cast either into Teflon ring molds (15.5mm OD, 11.5mm ID) for mechanical testing, or Lab-Tek Chambered coverglass slides (Thermo Scientific Inc – Nunc, Rochester, NY) for confocal microscopy. Gels were incubated at 37°C overnight before application of different digestion media.

Table 3-1. Summary of samples cast and their respective digestion treatments.

Sample	Network in Gel		Digestion Treatment	Comments
	Collagen	Fibrin		
C in PBS	•		1x PBS	Collagen control
C in Pn	•		0.02 U/ml Plasmin	Negative control for plasmin
CG in Pn	•	○	0.02 U/ml Plasmin	Resulting collagen network after fibrin digestion in co-gel
CG in PBS	•	•	PBS	Co-gel control
CG in Cs	○	•	1U/ml Collagenase	Resulting fibrin network after fibrin digestion in co-gel
F in Cs		•	1U/ml Collagenase	Negative control for collagenase
F in PBS		•	1x PBS	Fibrin control

*Positive controls were carried out by digesting collagen in collagenase and fibrin in plasmin. These gels were fully digested.

Legend:
C: Pure collagen gel Pn: 0.02U/mL Plasmin
F: Pure fibrin gel Cs: 1U/mL Collagenase
CG: Collagen-fibrin co-gel PBS: 1x Phosphate-Buffered Saline
•: network present before and after digestion ○: network initially present, but digested with treatment

The digestion protocols are summarized in Table 1. Gels were treated with either 0.02U/mL plasmin ("Pn") (Sigma-Aldrich), 1U/mL high purity collagenase ("Cs") (Sigma-Aldrich), or 1x Phosphate-Buffered Saline ("PBS") (Mediatech). Positive controls to verify the efficacy of the enzymes were performed on pure collagen and pure fibrin gels. All digestion treatments were left overnight at 37°C before further testing or preparation.

3.2.2 Scanning Electron Microscopy (SEM)

Gels were prepared for SEM after digestion treatment using the protocol described in [59]. Briefly, the gels were fixed with 2.5% glutaraldehyde (Electron

Microscopy Services, Hatfield, PA), followed by post-fixation staining with 1% osmium tetroxide (Electron Microscopy Services) before sequential dehydration with increasing concentrations of ethanol. The dehydrated samples were freeze-fractured in liquid nitrogen before critical point drying (Tousimis 780A, Tousimis Corp, Rockville, MD) and sputter-coating with platinum. Imaging was performed on a Hitachi S-900 Field Emission Gun SEM (Hitachi High Technologies America Inc, Pleasanton, CA) using a beam voltage of 2kV.

3.2.3 Mechanical Testing

The gel rings were looped over T-bar grips and uniaxially stretched to failure on an Instron 8848 MicroTester (Instron Worldwide Headquarters, Norwood, MA) equipped with a 5N load cell. Before stretch to failure, each ring was stretched to a grip-to-grip length of 14.5mm for 5s. Tensile stretch to failure was performed at a rate of 0.13mm/s. The 1st Piola-Kirchhoff stress (1st PK) was computed by dividing the force data by the cross-sectional area of each gel, estimated based on the volume of gel cast into each ring mold. From plots of 1st PK versus Green strain, the following material properties were calculated: ultimate tensile stress (UTS), Green strain at failure, tangent modulus, and transition strain. At least 6 gels from each digestion condition were tested. How each property is calculated from the stress-strain curve are reported previously [59].

3.2.4 Confocal Microscopy

Indirect immunofluorescence was used to stain the collagen fibrils for confocal microscopy. After the digestion treatments, gels were fixed in 4% paraformaldehyde (Electron Microscopy Services) for 10 minutes, followed by a blocking step with 5%

normal donkey serum (Jackson ImmunoResearch, West Grove, PA) for 2 hours. Application of a 1.0mg/mL collagen primary antibody (Novus Biologicals, Littleton, CO) was done overnight at 4°C, at a dilution of 1:100. The next day, gels were incubated with a secondary antibody (Dylight 488, Jackson ImmunoResearch) conjugated with green fluorescent dye at room temperature for one hour. Confocal imaging was performed on a Zeiss Cell Observer SD Spinning Disk Confocal Microscope (Carl Zeiss MicroImaging LLC, Thornwood, NY) with a 100x oil immersion objective. Emission was measured at 488nm, with resolution set at 512 x 512 pixels in-plane and a z-spacing of 0.2μm. The resulting dimensions of the confocal stacks were 133μm x 133μm in-plane with height ranging from 8μm to 10μm in the z-direction.

3.2.5 3-D Network Reconstruction

The confocal image stacks were first deconvoluted using the Huygens software (Scientific Volume Imaging B.V., Netherlands). 3-D reconstructions of the collagen networks in our samples were then generated using the FIbeR Extraction (FIRE) algorithm of [75]. Briefly, image stacks were smoothed using a Gaussian filter to reduce noise, and each pixel was binarized. The threshold value for binarization was determined by the Huygens software by specifying an average background area, i.e. an average pore size. Next, a custom Matlab distance function was used to compute the smallest distance from each fibril pixel to a background pixel. Using the pixels with the largest distance values as nucleation points, fibrils were constructed by tracing from these nucleation points along the maximal ridges of the distance function. From the reconstructed networks, the following network characteristics were analyzed: fiber length, fiber

tortuosity, and connectivity around each cross-link. From the total number of fibers (ranging from 2300 to 2900 fibers) and total number of cross-links (1750 to 2650 cross-links), average quantities were also computed. A length-average fiber length, L_L, was also calculated:

$$L_L = \frac{\sum L_i^2}{\sum L_i} \tag{3-1}$$

where L_i is the length of fiber i. This measure of the average fiber length weights longer fibers more heavily, which captures better the contribution of longer fibers in a non-normal distribution of fiber lengths. It should be noted that collagen *fibrils* cannot be distinguished from collagen *fibers* (from fibril bundling) in these confocal images; hence the term "fiber" refers to both collagen fibrils and fibers in these confocal results.

3.2.6 Statistical Analysis

Statistical comparisons of material properties and network parameters were performed using a 1-way ANOVA F-test, coupled with multiple comparisons using the Bonferroni procedure. Analyses were done using the commercial statistical package in Origin (OriginLab Corporation, Northampton, MA).

3.3 Results

3.3.1 Mechanical Testing Results

Figure 3-1 shows the average failure points of each gel condition after digestion treatments. The data show that failure points are grouped according to their respective network present in the gels: collagen gels (C in PBS, C in Pn, CG in Pn) are clustered in the range of low Green strains around 0.5 to 1, while fibrin gels (F in PBS, F in Cs, CG in Cs) are clustered at higher Green strains between 2.5 to 3.5. That the digested co-gels

37
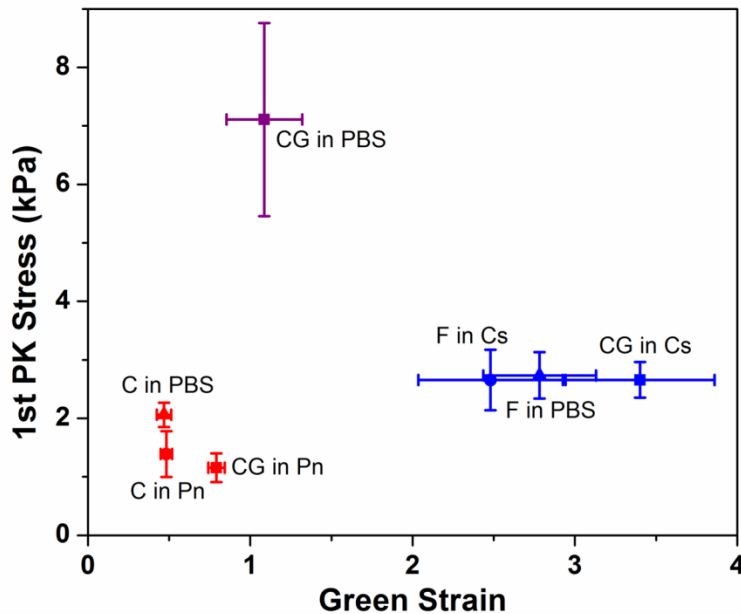
Figure 3-1. Failure points of stress-strain curves for all samples with different digestion conditions. Clustering of failure points for each network (collagen networks at lower strains, fibrin networks at higher strains) indicate that digestion with collagenase or plasmin was effective in eliminating the target network. The un-digested co-gel (CG in PBS) exhibited significantly higher failure stress because it contained twice the protein concentration compared to all other gels. Error bars represent 95% confidence intervals, n ≥ 6 for all samples.

exhibit similar failure properties to their pure counterparts strongly suggest that the digestion treatments with collagenase and plasmin were effective in eliminating the target network, to the extent that any residual undigested fibrils could not contribute significantly to overall mechanical behavior of the resultant network. The undigested co-gel (CG in PBS) exhibits higher UTS compared to pure collagen and fibrin gels, which is expected since the undigested co-gels have overall protein concentrations that are twice those of the pure gels. More importantly, while the digested co-gels (CG in Pn and CG in Cs) are derivatives of this undigested gel, the failure properties of the undigested gel (CG in PBS) cannot be derived from the sum of the properties of these digested gels.

While the clustering of failure points for each network suggests that both collagen and fibrin retain their general mechanical behavior regardless of gelation condition (i.e.

38
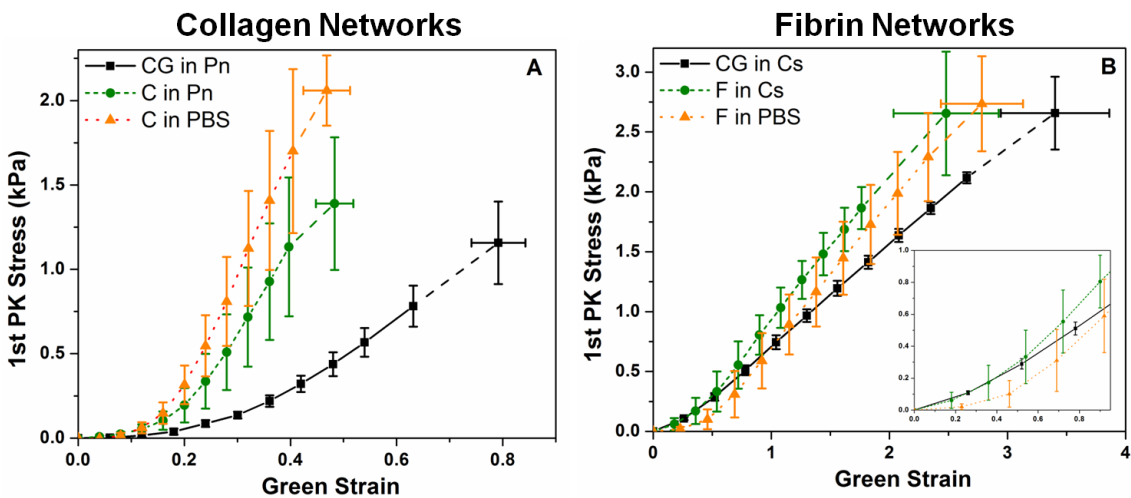
Figure 3-2. Stress-strain curves of (A) collagen, and (B) fibrin networks. Fibrin networks fail at much higher strains than collagen networks; inset in (B) shows the magnification of the fibrin curves up to the failure strains of the collagen networks. Both networks formed from digestion of co-gels (CG in Pn, CG in Cs) exhibited higher failure strains compared to their pure counterparts. Collagen PBS control (C in PBS) shows higher failure stress than gels in plasmin (C in Pn, CG in Pn). Error bars represent 95% confidence intervals, n ≥ 6 for all samples.

as a pure gel versus in a co-gel) or digestion treatment following gelation, subtle differences are evident when comparing the stress-strain behavior for each network (Figure 3-2). For the collagen curves (Figure 3-2A), the digested co-gel (CG in Pn) exhibits a larger toe region and fails at higher strain compared to the pure collagen controls. In addition, a difference was observed between the controls, with the PBS controls (C in PBS) failing at similar strains but significantly higher stresses compared to the negative controls (C in Pn). Comparison of the fibrin curves (Figure 3-2B) shows similar stress-strain characteristics for all three digestion conditions, with the digested co-gel (CG in Cs) failing at higher strains but similar stresses compared to the controls. Figure 3-3 shows further comparison of the mechanical behavior of the various gels in terms of their Green strains at failure (Figure 3-3A), UTS (Figure 3-3B), tangent modulus (Figure 3-3C) and transition strain (Figure 3-3D). The longer toe region seen in the
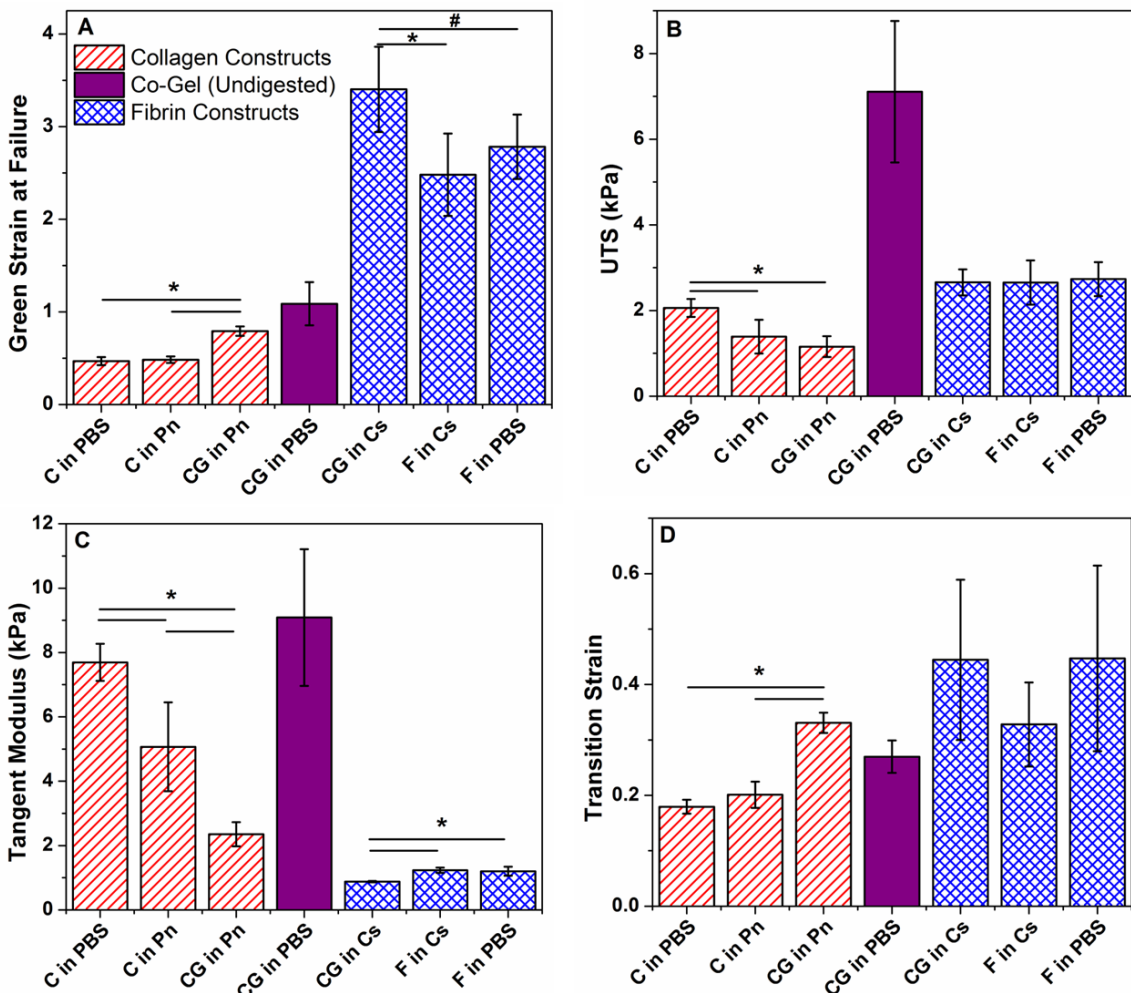
Figure 3-3. Comparison of material properties of (A) Green strain at failure, (B) ultimate tensile stress (UTS), (C) tangent modulus, and (D) transition strain between collagen and fibrin networks under different digestion conditions. In general, collagen and fibrin networks obtained from co-gel digestion exhibited similar UTS, but higher failure strains and lower tangent modulus when compared to their pure counterparts. Material properties of the undigested co-gel (CG in PBS) cannot be derived from the sum of properties of the digested co-gels (CG in Pn, CG in Cs), showing the the rule of mixtures does of apply to these collagen-fibrin systems. Error bars represent 95% confidence intervals, $n \geq 6$ for all samples. * and # represent statistical significance at the 95% and 90% levels respectively.

collagen network after co-gel digestion (CG in Pn) from Figure 3-2A is shown by the larger transition strain compared to controls (Figure 3-3D). In addition, the higher stresses seen in the collagen PBS controls are manifested in statistically significant differences in UTS and tangent modulus when compared to the negative controls (C in

Pn). Overall, similar statistical trends were observed for both collagen and fibrin: the digested co-gels exhibited higher failure strains, similar UTS, and lower tangent modulus when compared to their pure component counterparts (both PBS and negative controls). These comparisons are statistically significant at the 95% confidence level, with the exception of Green strain at failure for fibrin between the digested co-gel (CG in Ce) and PBS control (F in PBS) which is significant at the 90% level (p-value = 0.067).

3.3.2 Microstructural Results

Figure 3-4 shows SEM images of the gels after digestion. Images of the negative controls of pure collagen (C in Pn) and pure fibrin (F in Cs) appear similar to their respective PBS controls (C in PBS and F in PBS), which suggests that the network microstructures were not affected by the digestion media. Comparison of the pure collagen and pure fibrin networks show that both protein matrices qualitatively exhibit similar diameters; closer inspection of these images (see Supplementary Material for larger images) revealed characteristic banding on the collagen fibrils, absent in the fibrin fibrils. The co-gel control (CG in PBS), however, exhibits distinct differences in fibril diameters: finer, wisp-like structures can be seen in addition to the fibrils of similar thickness to those observed in the pure collagen and fibrin images (representative fibril diameters shown by arrows → ←). These wispy, web-like structures are still prevalent after the collagen had been digested (CG in Cs), strongly indicating that these structures are fibrin fibrils. Qualitatively, the distribution of fibril diameters of collagen appears similar in the digested co-gel (i.e. CG in Pn) compared to the pure collagen gels, although less bundling is observed (denoted by * in images) between the fibrils such that *fiber*

41
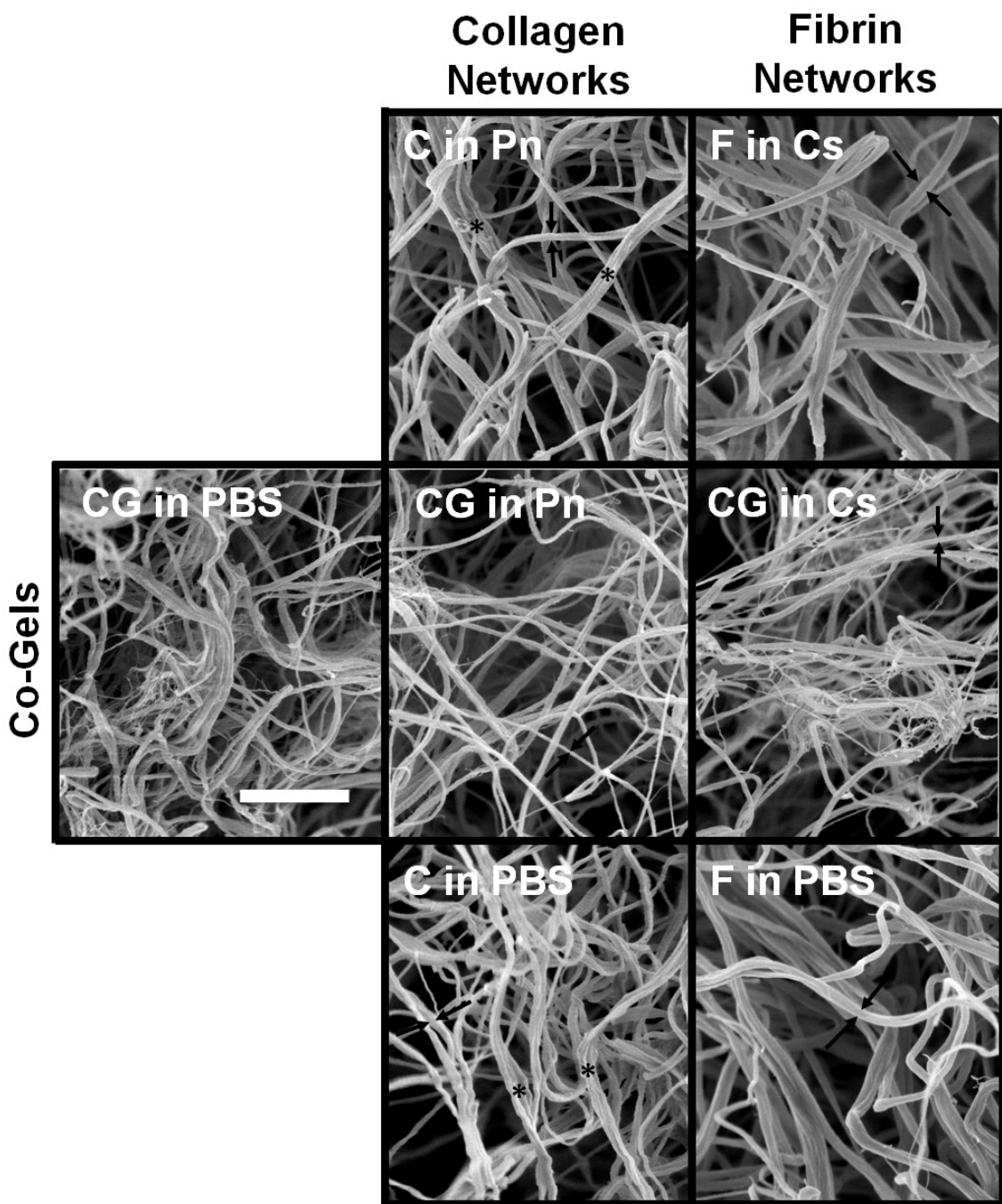
Figure 3-4. SEM images taken at 30,000x of collagen (2nd column) and fibrin (3rd column) networks under different digestion conditions; samples obtained from co-gels showed in middle row. The collagen network from co-gel digestion (CG in P) showed less fibril bundling (indicated with * on images) than the pure collagen gels, and have slightly smaller average fibril diameters The fibrin network from co-gel digestion (CG in Cs) contained wispy, web-like structures absent in the pure fibrin gels. Arrows (→ ←) on images denote representative fibril diameter for each gel. Scale bar = 1µm and is representative for all images.
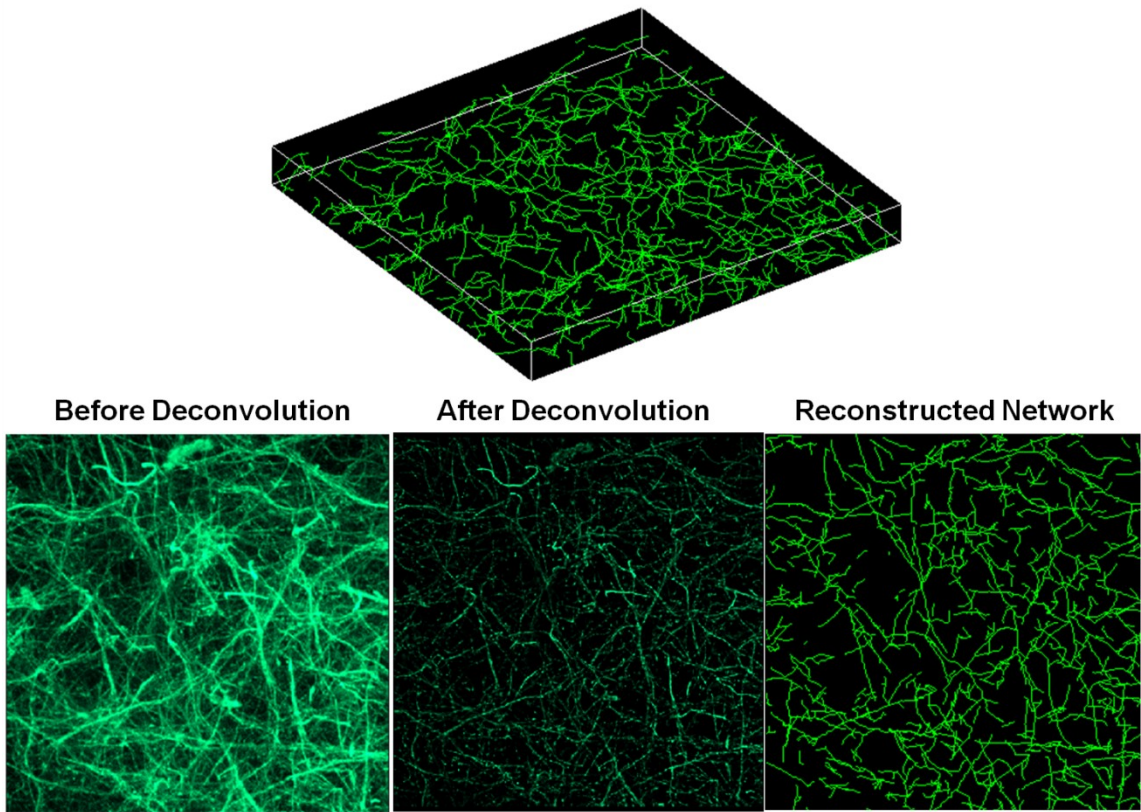
Figure 3-5. Example images of a reconstructed collagen network (C in Pn). Top: Example image of the 3-D reconstructed network; final dimensions for all samples are 133μm x 133μm in-plane, with height ranging from 8 - 10μm in the z-direction. Bottom: 2-D projections of the collagen network comparing the raw collapsed z-stack image from confocal microscopy (left), the same collapsed image after deconvolution (middle), and the reconstructed network using the FIRE algorithm (right).

diameters appeared smaller in these digested co-gels. Finer fibrils can also be seen in the CG in Pn co-gel, albeit much less prevalent than in the fibrin-remaining co-gel (CG in Cs). While we are unable to discern whether these finer fibrils are collagen or fibrin, we believe that they are primarily residual fibrin fibrils that were not digested. Collectively, comparison of SEM images suggests that both collagen and fibrin network morphologies are altered when formed in the presence of each other: fibrin fibril diameter decreases, and collagen fibrils exhibit less bundling.

To analyze further network differences in the collagen networks, 3-D reconstruction of these networks using confocal image stacks of the collagen gels were performed. Figure 3-5 shows a representative 3-D image of a reconstructed collagen network (C in Pn) (top), as well as the comparison between the collapsed confocal image stack (bottom) before deconvolution (left), after deconvolution (middle), and the reconstructed network (right). It should be reiterated that collagen fibrils cannot be differentiated from collagen fibers (bundled fibrils) in these confocal images, such that the term "fiber" refers collectively to both fibrils and bundled fibers. Comparison of the collapsed images before and after deconvolution indicates that while the deconvolution process makes fibers more distinct by removing the spread in fluorescence, fibers also appear more fragmented as a result. These fragmented fibers are re-connected during the network reconstruction process via the FIRE algorithm, where fiber segments of similar orientation are extended as the same fiber. Comparison between the reconstructed network and deconvoluted network shows good qualitative agreement, in general, in network morphology. Results analyzing network morphologies of the different conditions are shown in Figure 3-6, comparing total fiber length per volume (A), average connectivity around a cross-link (B), average *segment* length and tortuosity (C and D), and average *fiber* length and tortuosity (E and F). A *segment* is defined as the spacing between cross-links, while a *fiber* can be comprised of multiple adjacent segments of similar orientation (see Figure 3-7 for an illustration). The minimum value allowable between 2 segments to be considered part of the same fiber (i.e. angle α in Figure 3-7) was set at 120°. This value was determined via a sensitivity analysis examining the effect

44
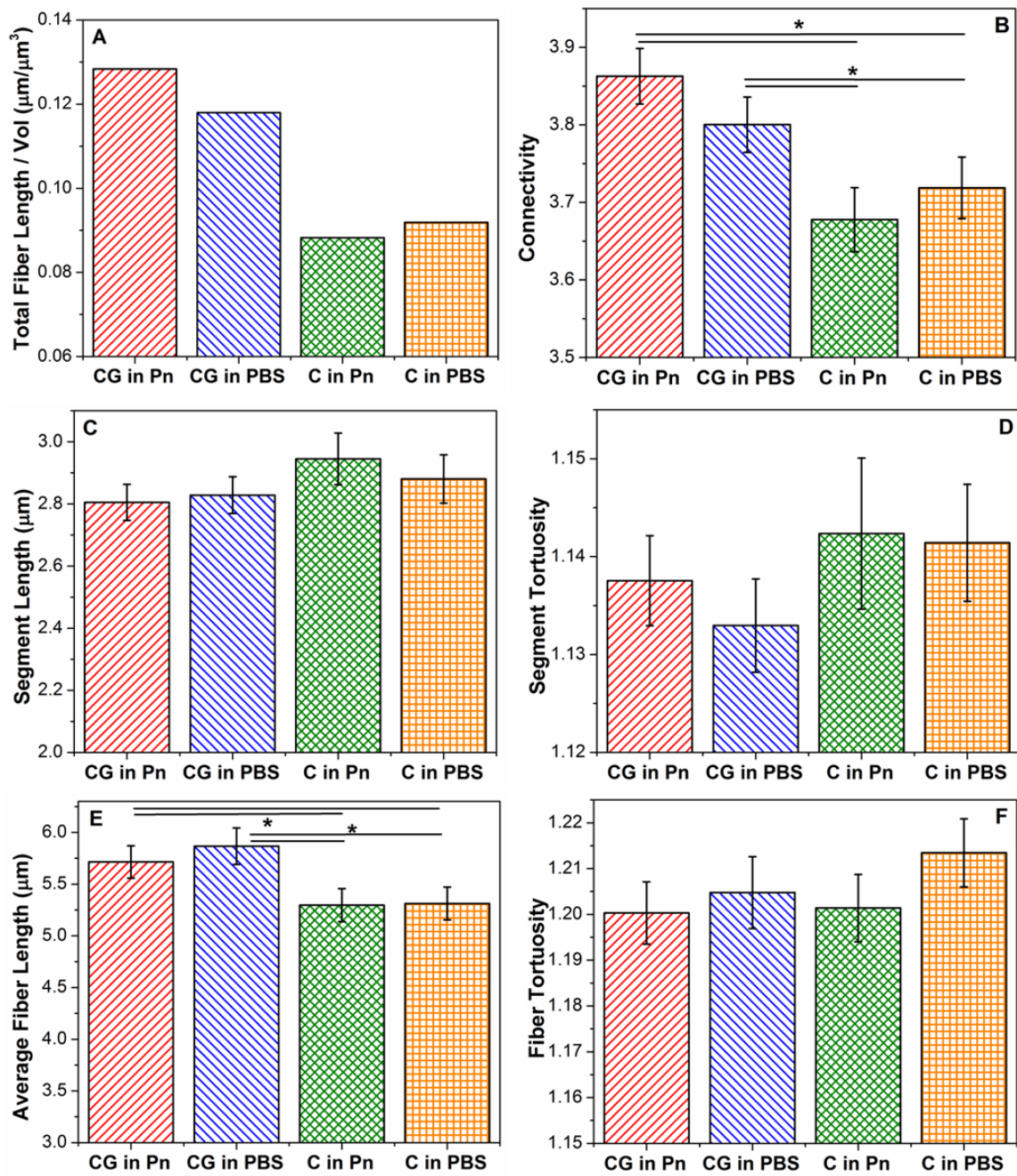
Figure 3-6. Comparison of network parameters of (A) total fiber length per volume, (B), connectivity, (C) segment length, (D) segment tortuosity, (E) fiber length, and (F) fiber tortousity between collagen networks obtained under different digestion conditions. Collagen networks obtained from co-gels (CG in PBS, CG in Pn) show high connectivities and longer average fiber lengths. Error bars represent 95% confidence intervals. * represents statistical significance at the 95% level. Note: The y-axes of these plots do not start at "0".
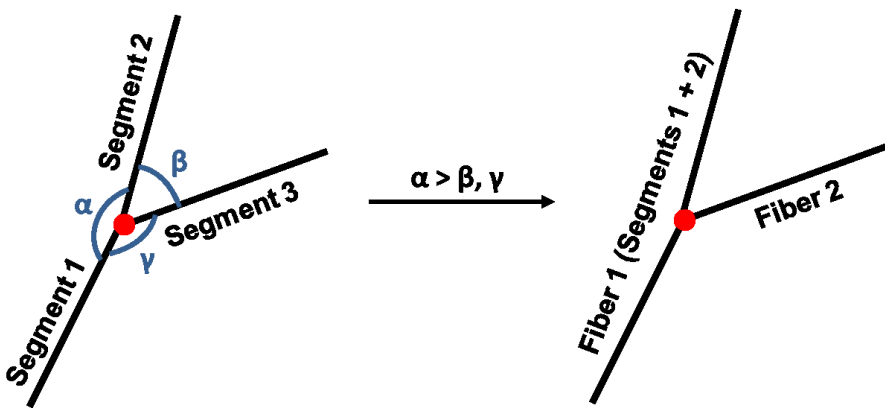
Figure 3-7. Schematic representation of the definition of a segment and of a fiber in the FIRE algorithm. Each length between adjacent cross-links are defined as a segment; fibers can comprise of several segments, where segments with a similar orientation are considered part of the same fiber. α was set at 120° from sensitivity analysis.

of varying α on the total number of cross-links with connectivity of only 2 (data not shown). Since cross-links of connectivity of 2, formed by contact between two fibril ends, were expected to be very uncommon, a large jump in the number of such cross-links (which occurred between 120° and 130°) suggested at α values greater than 120°, several fibers had been artificially broken up into two fibers. In general, no significant differences in network characteristics were observed between samples formed under the same gelation condition, but placed in different digestion medium (i.e. CG in Pn vs CG in PBS, and C in Pn vs C in PBS). Assuming the same collagen density for all samples, the total fiber length per volume (Figure 3-6A) provides a crude measure of fiber diameter, with the higher values in the co-gels (CG in P, CG in PBS) indicating *smaller* average fiber diameters compared to the pure gels (C in Pn, C in PBS). In addition, the collagen networks formed in the co-gels also exhibited higher average connectivities (Figure 3-6B) compared to the pure gels (* indicates statistical significance at the 95% level). While no significant differences were observed in average segment length (Figure 3-6C) and average segment tortuosity (Figure 3-6D) between the co-gels and pure gels, the
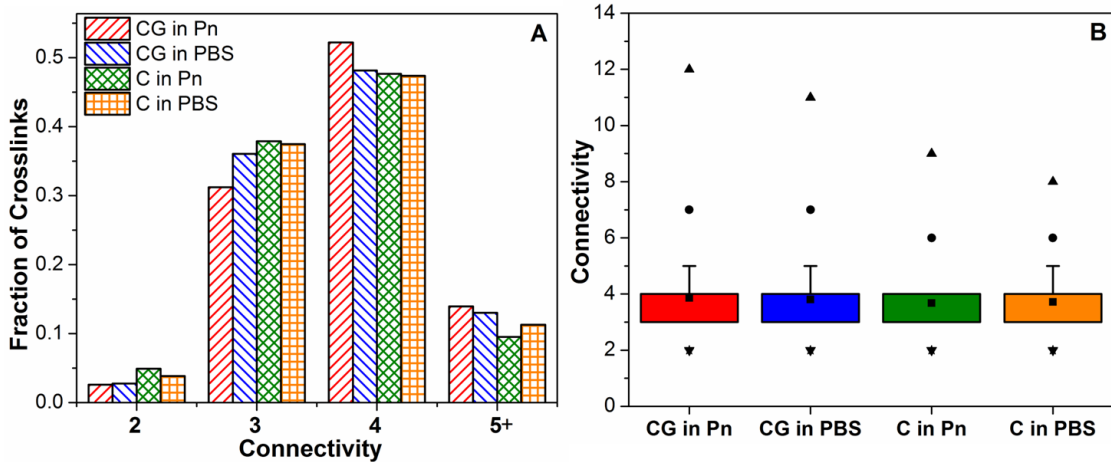
Figure 3-8. Comparison of connectivity distributions in collagen networks from different casting and digestion conditions. (A) shows that >80% of cross-links contain connectivities of 3 or 4 in all samples. Box-plot in (B) shows that the collagen networks from co-gels exhibit slightly higher maximum connectivities (▲) and higher connectivities at the 99% level (●).

collagen network in co-gels exhibited longer average fiber lengths (Figure 3-6E) but similar fiber tortuosities (Figure 3-6F) than the networks in the pure gels.

To investigate these differences in connectivities and fiber lengths further, their distributions were analyzed in Figures 3-8 and 3-9, respectively. The distribution of connectivities comprises integer values which spanned a narrow range from 2 to 12. Figure 3-8A shows similar overall distributions of connectivities across all samples, with more than 80% of crosslinks having connectivities of 3 or 4. The collagen networks from co-gels (CG in Pn, CG in PBS) exhibiting a slightly higher proportion of crosslinks with connectivities 5 or greater. The box-plot in Figure 3-8B shows that key differences in connectivity distributions occur only above the 90th percentile (top of whisker): the collagen networks in co-gels exhibited higher connectivities at the 99th (●) percentile and had larger maximum connectivity values (▲). Collectively, these results explain the higher average connectivities in the co-gels (CG in P, CG in PBS): these networks have
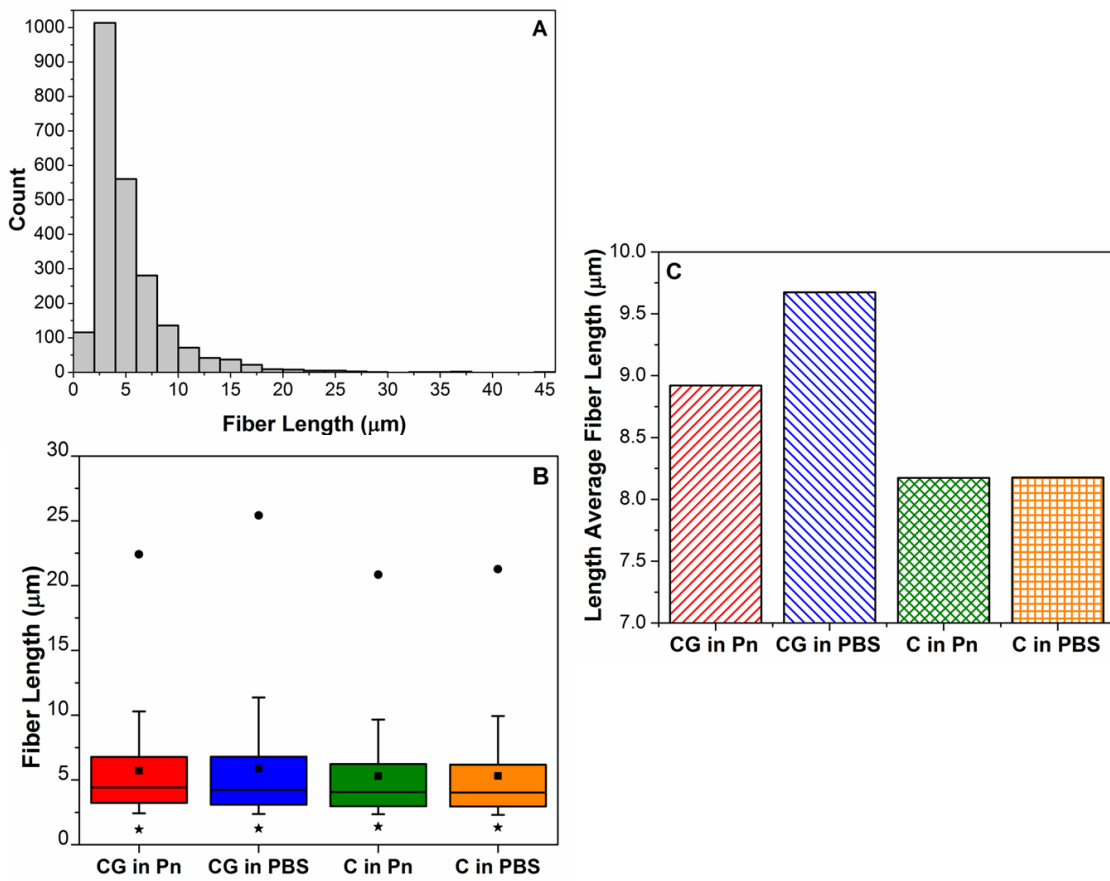
Figure 3-9. Analysis of fiber lengths and their distributions in the collagen networks from different casting and digestion conditions. (A): Example of the non-normal distribution of fiber lengths in a collagen network (C in Pn). (B) Box-plot comparing fiber distributions; whiskers represent 10th to 90th percentile, ■ represents the mean, * and ● represent 1st and 99th percentile respectively. Co-gels have longer fiber lengths at 90th and 99th percentile, indicating presence of very long fibers vs. pure gels. (C) Higher length-average fiber lengths in the co-gels confirm the presence of very long fibers in the co-gels compared to the pure collagen counterparts.

more crosslinks that have higher connectivities. Figure 3-9 shows similar analysis for the

fiber length distributions in the collagen networks, with Figure 3-9A showing an example

of the non-normal distribution of fiber lengths. The right-skewed distribution in all the

samples is evidenced by the lower median value (middle line in box) compared to the

mean (■) in the box-plot in Figure 3-9B. While all four samples showed similar fiber

lengths at the 25th, 50th and 75th percentiles (i.e. in the box region), longer fiber lengths at

the 90th (top of whisker) and 99th percentile (●) were observed for the networks in the co-gels compared to those in the pure gels. These results suggest that the longer average fiber lengths in the networks from co-gels (Figure 3-6F) are not due to a general increase in length of all fibers, but due to the *presence of very long fibers* in the co-gel networks. Comparison of the length-average fiber length (Figure 3-9C) confirms this result, as the difference in fiber lengths between the networks in co-gels vs networks in pure gels is further accentuated when longer fibers are weighted more heavily.

3.4 Discussion

This study investigated the effect of collagen-fibrin co-gelation on the network morphologies of each network, and how such changes in network architecture influenced overall mechanical behavior. Upon digestion of the collagen-fibrin co-gels with either plasmin or collagenase, a network of the undigested ECM remained in the gel. This observation suggests extensive end-to-end crosslinking between collagen and fibrin fibrils or monomers did not occur; instead, each biopolymer formed its own network that interpenetrated with the other in a "parallel" fashion. In addition, results showed effects on microstructure and mechanics of both collagen and fibrin when these ECM are co-gelated in the presence of each other (as summarized in Table 2):

Fibrin: Microstructural results from SEM images showed a finer network containing web-like/wispy structures, which apparently are fibrin fibrils, when the fibrin network is co-gelated with collagen. This observation is consistent with previous studies which showed that fibrin morphology was sensitive to gelation conditions such as thrombin and Ca^{2+} concentrations [7,61,66]. Furthermore, we had also shown

49

Table 3-2. Summary of results of changes in microstructure and mechanics of collagen and fibrin in collagen-fibrin co-gels, compared to their pure counterparts. Arrows represent direction of change in each characteristic for the ECM in co-gel compared to the pure gel; — means characteristic was unchanged. X for fibrin microstructure indicates these parameters were not measured.

		Collagen in Co-gel vs. Pure Collagen	Fibrin in Co-gel vs. Pure Fibrin
Microstructure	Fibril Diameter	↓	↓
	Fibril bundling	↓	N/A
	Average Fiber Length	↑	X
	Network Connectivity	↑	X
Mechanics	Strain at Failure	↑	↑
	UTS	—	—
	Tangent Modulus	↓	↓
	Transition Strain	↑	—

previously the existence of such finer fibrin fibrils in collagen-fibrin co-gels, although these were only observed at higher collagen concentrations [59]. Mechanically, fibrin formed in the co-gels exhibited similar failure strength, lower modulus, but greater extensibility before failure. Correlation of SEM results with these mechanical data for fibrin suggested that, in general, a decrease in fibril diameter resulted in a more compliant gel of similar tensile strength, but greater extensibility before failure. This result is contrary to previous findings of Rowe et al. [7], who found that a decrease in fibril diameter (formed by decreasing thrombin concentration) effected an increase in UTS and modulus. It should be noted that, however, the microstructural changes caused by altering thrombin concentrations in that study were significantly more drastic; SEM images from [7] showed that as fibril diameter decreased with decreasing

thrombin concentration, the overall network became much more highly interconnected with smaller pores, leading to an increase in mechanical strength and stiffness. In contrast, our SEM images of fibrin networks under different conditions at lower magnifications of 10,000x (see Supplementary Material) showed no visible differences in network architecture. Previous studies on fibrin networks suggest that thicker fibrin fibrils are formed from lateral associations of thinner fibrils, with possible inter-fibril γ chain cross-linking [71]. Conceivably, the smaller failure strain observed in the pure fibrin gels (F in PBS, F in Cs) is due to decreased extensibility of these thicker fibrils as the inter-fibril cross-links hinder stretch of individual fibrils within these fibers. The lower stretch borne by these thicker fibrils necessitates that the thinner fibrils bear a larger proportion of the overall macroscopic stretch, causing catastrophic failure to occur at lower strains. In addition, these inter-fibril cross-links could also stiffen fibrin bundles compared to individual fibrils, resulting in an overall network with slightly higher modulus.

Collagen: Similar trends in microstructure and mechanics were observed for our collagen networks when formed in the presence of fibrin (CG in Pn) compared to formation in its absence (C in Pn, C in PBS): SEM images showing a decrease in average collagen fibril and fiber diameter were accompanied by mechanical data showing similar failure strength, higher strain at failure, and lower tangent modulus. A similar explanation could be made to correlate microstructure with mechanics, that inter-fibrillar bonding between collagen fibrils in bundled fibers [45] (i.e. bonding between laterally associated fibrils within fibers) decreased overall extensibility while

51

increasing stiffness. Further analysis into the collagen network from the reconstructed networks confirmed the result of smaller average collagen fibril/fiber diameters (cf. Figure 3-6A). In addition, while the collagen networks in co-gels showed higher average connectivities, this result was due to the *greater presence of cross-links with very high connectivities* rather than a general increase in connectivity throughout all cross-links. In all cases, connectivities around each cross-link of 3 or 4 were predominant. A connectivity of 3 suggests branching of collagen fibers from a bundled fiber, a phenomenon also observed from cryo-SEM of collagen networks [45]. A cross-link with connectivity 4 can be formed by two fibrils crossing at close proximity to each other and forming an inter-fibrillar chemical bond, or fibrils intertwining to form a mechanical bond. Connectivities above 4 are likely a result of clumping of fibrils, with fibrils radiating out from a central cluster as the FIRE code is unable to resolve fibrils within the cluster. Results from this study suggest that, in general, collagen networks formed in the presence of fibrin retain similar cross-link characteristics compared to collagen networks formed purely by themselves, with similar spacings and tortuosities between cross-links (i.e. segment lengths, cf. Figure 3-6C and 3-6D), and predominantly connectivities of 3 or 4. The very high connectivities observed for the collagen networks in co-gels (Figure 3-8B) suggest more clustering of collagen fibrils when formed with fibrin.

Several groups have previously studied the correlation between collagen network microstructure and overall mechanical behavior of collagen gels. Notable works include the study by Christiansen and co-workers [26], who investigated the effect of

pH and temperature on collagen network formation. In that study, they reported a decrease in collagen fibril diameter with increasing pH from 5.0 to 9.0; comparison with mechanical properties showed that an increase in collagen fibril diameter correlated well with an increase in low strain modulus, but had no effect on UTS or high strain modulus. A similar study by Roeder et al. [70] confirmed the decrease in collagen fibril diameter with increasing pH, as well as an increase in fibril length. However, the group reported an accompanying increase in UTS and linear modulus, results that were contrary to Christiansen et al.. Roeder and co-workers concluded that collagen fibril length had a greater effect on mechanical properties than fibril diameter. In the current study, co-gelation of collagen with fibrin yielded longer but less bundled collagen fibers (i.e. smaller fiber diameter); however, like Christiansen et al., no significant increase in UTS was observed. In contrast to Roeder et al., results from this study suggest a greater effect of collagen fibril diameter than fibril length – thicker fibers reduce macroscopic extensibility and increase overall gel stiffness, presumably due to inter-fibrillar bonding in fiber bundles. It should be noted that all three studies employed similar strain rates for mechanical testing, so that these differences are not due to the viscoelastic nature of these gels. Such discrepancies among reported results highlight the complexity of biological networks: changes in microstructure alone cannot fully account for changes in macroscopic mechanical properties. Different gelation conditions such as variations in pH and presence of contaminants could have affected fibrils on a molecular level, e.g. the degree of cross-linking and bonding between fibrils – factors that cannot be visualized using SEM or confocal microscopy.

Mechanical data for collagen networks revealed additional differences absent in fibrin networks. Firstly, the collagen PBS control (C in PBS) exhibited a higher UTS compared to the gels placed in plasmin (C in Pn, CG in Pn). While positive controls were carried out to verify efficacy of the enzymes used – pure collagen and fibrin gels were fully dissolved when placed in collagenase and plasmin respectively, the plasmin could have caused slight degradation of the collagen network and reduced the strength of the gel even though the collagen network remained largely intact. Secondly, the collagen gels formed by co-gelation with fibrin showed significantly larger transition strains, i.e. these gels have a longer toe region. Previous studies suggest that the toe region corresponds to straightening of undulating fibrils at the fibrillar level [52] and the molecular level [76], as well as fibril reorientation in the direction of stretch [43,77]. Results from this study showed similar fiber and segment tortuosities between collagen networks in co-gels and in pure gels, which indicated that this longer toe region in co-gels could not be explained by more curved fibrils on the fibrillar level. Whether the longer toe region was caused by differences at the molecular level, or due to changes in network characteristics more conducive for fibril rearrangement, remains unclear.

The combination of SEM and confocal imaging techniques allowed observation of collagen networks both at the fibril level and at the network level. However, visual comparisons of images from these techniques showed straighter fibers and larger void spaces in the confocal images compared to SEM. We believe that these discrepancies are due to structural artifacts introduced during sample preparation for SEM; the drying

Table 3-3. pH and ionic strengths of the various gel formulations.

	pH	Ionic Strength (M)
Pure Collagen (C)	7.2	0.12
Pure Fibrin (F)	7.0	0.15
Collagen-Fibrin Co-Gel (CG)	7.2	0.16

process is known to cause slight network collapse resulting in smaller void spaces [44]. Nevertheless, SEM images provide useful qualitative information on our networks at the fibrillar level such as collagen fiber bundling and wispy fibrin fibrils.

Previous studies have shown that gelation conditions of pH and ionic strength influenced fibril formation of both fibrin [60] and collagen [69], resulting in varied microstructures. The formulations used to prepare the gels for these studies varied from each other such that slight differences in pH and ionic concentration were observed between the formulations (Table 3). While the pH of all three formulations were maintained close to neutrality, there was significant difference in the ionic strength of pure collagen (C; 0.12M) compared to that in the co-gel (CG; 0.16M). Wood and Keech [69] reported that an increase in ionic strength from 0.13M to 0.23M effected an increase in collagen fibril diameter; more extensive fibril bundling was also observed. In contrast, an opposite trend for changes in collagen microstructure was observed in our gels: an increase in ionic strength from 0.12M (in pure collagen) to 0.16M (in the collagen-fibrin co-gel) resulted in less fibril bundling and a decrease in average fibril diameter. These different findings highlight the intricate effects of gelation conditions on collagen microstructure and warrants further investigation.

Results from this study indicated that while averaged characteristics are useful in quantifying gross differences in overall network architecture, they do not give the full picture of how the network morphology is changed. Thus, these findings are also relevant towards improving modeling approaches to understand the mechanics of certain native and bioengineered tissues where a collagen-fibrin co-gel is a relevant experimental model. Different groups have used a variety of approaches to model fiber networks, ranging from periodic [78] or homogeneously distributed fiber models [79], to known models for disordered networks, e.g. the Poisson-Voronoi model [80]. To model the mechanical contribution of the ECM in tissues, our group employs a multi-scale framework using a Representative Volume Element (RVE) containing a fiber network around each Gauss point [14,39]. This current method network generation in the RVEs creates a randomly orientated network of elastic fibers connected to one another via rigid pin joints [39]. While our current network models are able to capture the inhomogeneous and anisotropic nature of ECM fiber networks, they suffer the same limitation as the afore-mentioned approaches: these networks do not accurately reflect the microstructure of the ECM networks in the tissues. Here we utilized a method of characterizing ECM networks developed by Stein et al. via 3-D reconstruction of confocal z-stacks and fiber network analysis to obtain actual ECM network characteristics (connectivities, fiber length distributions, fiber tortuosities etc), which can be used to improve our network generation approaches to create fiber networks that mimic more closely the actual microstructure of the ECM in tissues.

4. Fiber Network + Interstitial Matrix Interactions I: Microstructural Interactions in Soft Tissues Using a Coupled Fiber-Matrix Model

The content of this chapter was published in the Journal of Biomechanical Engineering (Jan 2013) as *"A Coupled Fiber-Matrix Model Demonstrates Highly Inhomogeneous Microstructural Interactions in Soft Tissues Under Tensile Load"*, in collaboration with Dr. Mark Shephard's group at Rensselaer Polytechnic Institute.

4.1 Introduction

The mechanical properties of many soft connective tissues are governed by a fiber network (primarily collagen in most tissues) and surrounding non-fibrillar matrix (NFM; e.g., proteoglycans, glycoaminoglycans, cells, etc.). To understand how healthy tissues function, and how properties change in injury and disease, it is necessary to quantify the mechanical response of both the collagen network and the NFM, as well as the nature of the interaction between these tissue constituents. Because the relative contribution of different tissue components is difficult to ascertain experimentally, mathematical modeling is frequently applied to empirical data to characterize and quantify the roles of collagen and NFM in imparting mechanical properties to soft tissues. Phenomenological models (e.g. [81–83]) provided initial insights into the mechanics of fibrillar tissues, and, more recently, structural models (e.g. [84–92]) have emerged that capture more information about the tissue architecture. With the collagen network thus defined, the NFM is often modeled using a simple mathematical representation, such as a neo-Hookean [93–96] or Mooney-Rivlin [97–100] solid, and assumed to contribute to the composite behavior in a summed or "parallel" sense. A limitation of this approach is the inability to evaluate local interactions between fibers and NFM. Some models have

utilized an additional term to account for fiber-matrix interactions [98,101–103], but in general, the appropriate definition for the interaction term is unknown. To overcome this limitation, the current study presents a method wherein the collagen fiber network and surrounding NFM are microscopically coupled, making it possible to evaluate specifically the interaction between fibers and matrix.

Recently, we developed a computational network-based microstructural model to examine how specific NFM properties alter the response of fiber-matrix composites under load [104]. This model, consisting of a representative volume element (RVE) containing a fiber network (collagen) and neo-Hookean solid (NFM), fit experimental data of collagen-agarose co-gels [37] well and provided insight into the role of NFM in tensile mechanics. The NFM was found to preserve volume and restrict collagen fiber reorganization in a concentration-dependent manner. Within a specific range of property values, the NFM pressurized the composite tissue in such a way as to result in a negative (compressive) stress in the loading direction, even though the RVE was loaded in tension. Although this model provided useful results, it was constructed according to the conventional "parallel" approach of superposition of the two constituents (i.e., collagen network and NFM), so it was unable to examine interactions between collagen fibers and the surrounding NFM (as mentioned above) or to identify inhomogeneities in the stress field. For example, in a uniaxial extension experiment, the average transverse and shear stresses would be zero, but local shear would surely occur in the neighborhood of a fiber. Such local stresses could be much larger than average values, which could have important implications in initiating failure of the NFM or in greatly altering the site-

specific cellular environment. Therefore, the objective of this study was to develop a microstructural modeling approach capable of (a) quantifying local stresses throughout the computational domain and (b) exploring interactions between NFM and the embedded collagen network.

4.2 Methods

4.2.1 Modeling Approach

Large-network models (e.g., [14,48,80,105–107]) are composed of an arrangement of interconnected fibers, which are often represented as one-dimensional linear springs or nonlinear rods. The NFM surrounds the fibers and permeates the non-fiber space in a fully three-dimensional manner. In order to couple these components in a unified scheme, a multi-dimensional modeling approach was employed. Such a formulation is advantageous in that the total number of degrees of freedom can be reduced without overall loss of accuracy. For example, collagen fibers can still be modeled as one-dimensional elements, thereby greatly reducing computational demand, while more detailed aspects of collagen fiber morphology (e.g., fiber crimp) can be taken into account mathematically (i.e., in the constitutive equation) instead of geometrically. A finite element mesh, constructed upon the framework of the fiber network, was then used to define the geometry of the NFM and to allow for coupled interactions between the NFM and specific fibers within the network. This study used a multidimensional meshing scheme to construct coupled representations of the collagen fiber network and the surrounding NFM in order to characterize the interactions between constituents in soft

Random Seed Points **Voronoi Tessellation** **Fiber Network** **Nodes at Intersections**
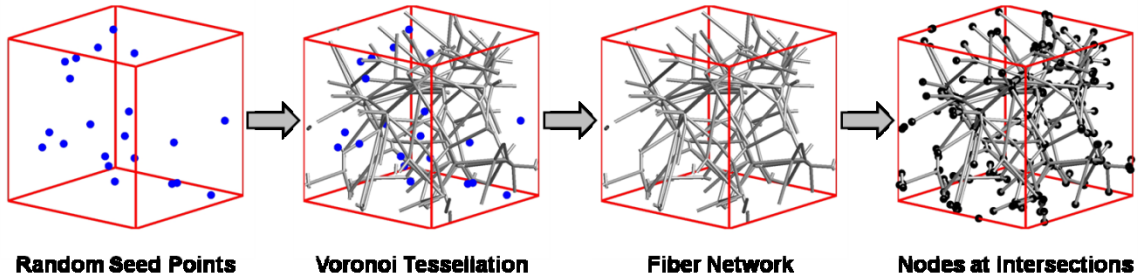
Figure 4-1. Computational representations of collagen fiber networks were constructed by randomly placing a set of seed points in a representative volume element, constructing a Voronoi tessellation about these points, defining fibers as the edges of Voronoi elements, removing seed points, and placing pin-joint nodes at each edge-edge and edge-boundary intersection.

tissues subjected to tensile load. The newly developed *coupled* model was compared to our earlier *parallel* model [104].

4.2.2 Network Generation

Collagen gels were modeled using Voronoi networks [80] as described previously [104]. Seed points placed randomly within representative volume elements (RVEs) were used to construct Voronoi tessellations (Figure 4-1). After construction of the network, seed points were removed, and nodes were placed at the intersections of Voronoi edges with each other or with the RVE boundaries. Nodes were represented as freely rotating pin-joints. Initially isotropic networks were rescaled in the loading (x_1) direction and clipped to produce networks within a cubic domain whose alignment matched polarized light alignment data from collagen-agarose co-gel experiments [37]. Any isolated fibers or fiber clusters were removed to leave a single, fully interconnected network in each RVE. Five similar but distinct RVEs were created (Table 4-1) and analyzed. Collagen fibers were represented as one-dimensional nonlinear springs with constitutive behavior defined as [4,14,93]:

Table 4-1. Initial properties of Voronoi networks evaluated in this study.

Network	Number of Fibers	Number of Nodes		Orientation Tensor		
	Total	Boundary	Internal	Ω_{11}	Ω_{22}	Ω_{33}
1	689	194	296	0.590	0.196	0.214
2	828	240	354	0.625	0.187	0.188
3	668	196	285	0.607	0.196	0.197
4	725	214	309	0.584	0.198	0.218
5	682	216	287	0.597	0.203	0.200
Mean	718.4	212.0	306.2	0.601	0.196	0.203
Std. Dev.	64.8	18.6	28.3	0.016	0.006	0.012

$$f = \frac{E_f A}{B}(e^{B\varepsilon} - 1) \tag{4-1}$$

where f is force in given fiber, E_f is fiber Young's modulus in the zero-strain limit, A is cross-sectional area, B is a nonlinearity constant, and ε is the fiber Green strain along the fiber. Equation 4-1 specified properties for individual fibers, but the mechanical response of each RVE resulted from the collective behavior of the full network of fibers. Fiber parameters (i.e., E_f, A, and B) were defined using values similar to those used previously [14,104]. The NFM was represented as a compressible neo-Hookean solid, with the Cauchy stress defined as [108]:

$$\sigma_{ij}^{nfm} = G\left(\frac{F_{ik}F_{jk}}{J} - J^{-2\beta-1}\delta_{ij}\right) \tag{4-2}$$

where G is shear modulus, F is the deformation gradient tensor, J is the determinant of F, $\beta = v_{nfm}/(1-2v_{nfm})$, and v_{nfm} is Poisson's ratio of the NFM. As done previously [109], v_{nfm} was set to 0.1. The NFM shear modulus was varied over a range of values ($G = 10$, 110, 720 and 4300 Pa) corresponding to 0.05, 0.125, 0.25 and 0.5 % w/v agarose [110] in our experimental collagen-agarose studies [37,111]. To assess the role of compressibility, a

set of simulations with v_{nfm}=0.45 was also evaluated for G=110 Pa. Built upon this common framework, parallel and coupled models were evaluated for each network as described below.

4.2.3 Parallel Model

We previously [104] presented results from simulations using a parallel fiber-matrix model. In the current study, results obtained from simulating a wider range of G values are presented. Some relevant details of the parallel model are repeated here for clarity, and to highlight differences between the parallel approach and the newly-developed coupled model (described below). In the parallel model, the stress due to the collagen network was computed via a volume-averaging approach [38,39] based on the nodal forces on each RVE boundary:

$$< \sigma_{ij}^{col} >= \frac{1}{V} \sum_{\substack{boundary \\ nodes}} x_i f_j \tag{4-3}$$

where V is RVE volume, and f_j are the forces acting on boundary nodes (at positions x_i). Neo-Hookean NFM stresses were dependent only on the macroscopic deformation of the RVE, and the two stress components were combined in a simple summed (parallel) sense:

$$\sigma^{tot} = < \sigma^{col} > +\sigma^{nfm} \tag{4-4}$$

After application of RVE strain, positions of the internal nodes and of the unloaded boundaries were adjusted iteratively until the force balance at each internal node was satisfied and the total stresses on the free surfaces were minimized.
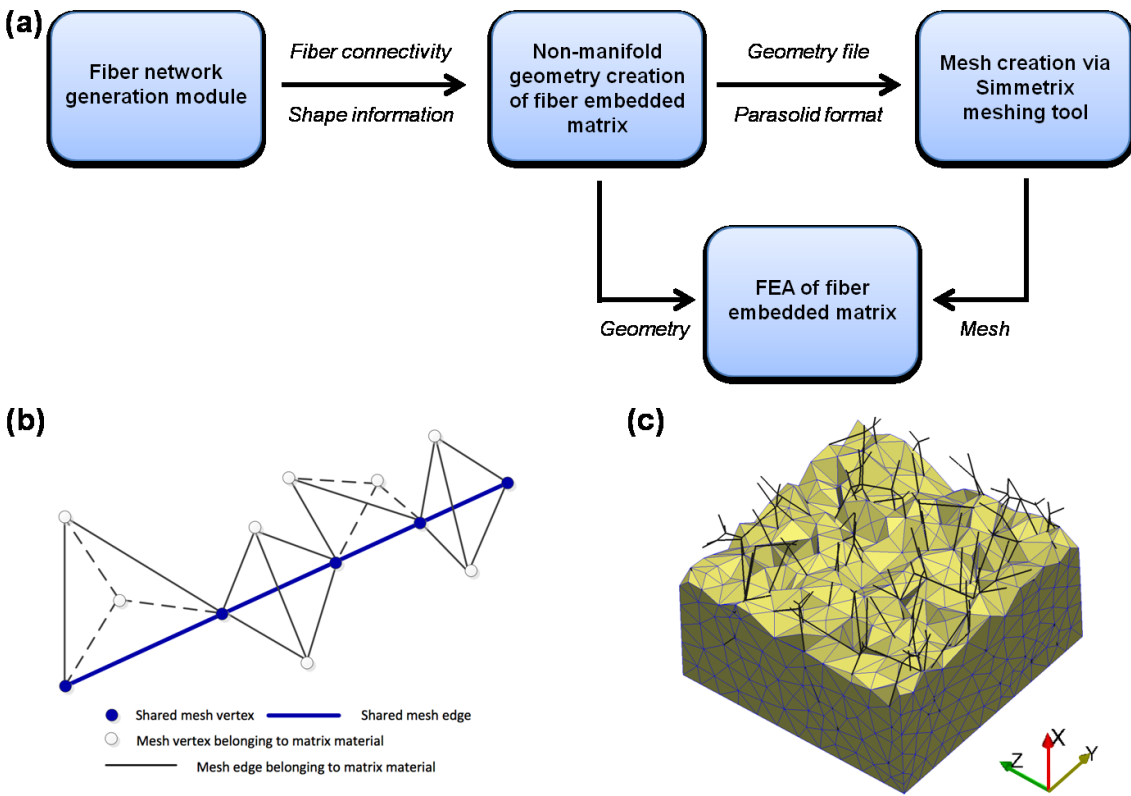
Figure 4-2. Development of the coupled fiber-matrix model: (a) work-flow demonstrating construction protocol for the coupled model; (b) illustration of the conforming multi-dimensional mesh and the mesh classification to the geometric model; (c) schematic showing the interior of the multi-dimensional mesh showing fibers (black lines) and meshed matrix (yellow elements with blue borders).

4.2.4 Coupled Model

A coupled fiber-matrix microstructural model was developed and used to model the interactions between collagen fibers and NFM. A geometric model of the RVE with the two constituents (i.e. collagen fibers and surrounding NFM) was represented as a 3D non-manifold geometric model [112] with the embedded fiber network treated as 1D wire edges. The workflow of applying finite element method in the coupled model is shown in Figure 4-2(a). The complete definition of a Voronoi fiber network including fiber connectivity (network topology) and crosslink coordinates (network shape) was provided by a fiber network generation module and then used as input for creating the multi-

63

dimensional non-manifold geometry via Parasolid API [113]. Simmetrix [114,115] meshing tools were used to create the conforming mesh from the generated RVE geometry.

The generated mesh was multi-dimensional with 3D tetrahedra for the solid matrix and 1D truss elements for the collagen fibers. The solid matrix and embedded fiber network were meshed together such that mesh vertices and mesh edges on the fibers were shared with the adjacent 3D solid elements (Figure 4-2(b)). Figure 4-2(c) shows the interior of the mixed dimensional mesh with shapes of elements intersecting the cutting plane retained. Displacements (u_1, u_2, and u_3) were selected as the nodal variables, and linear shape functions were used to interpolate the displacement field. Since linear tetrahedral and truss elements have the same nodal displacement variable, consistency between the two different dimensional elements was ensured. Newton-Raphson iteration was used to solve the nonlinear finite element equations describing the mechanics of the coupled system.

4.2.5 Model Solution and Analysis

For the coupled model, 0.5% strain steps were applied incrementally in the 1-direction until an RVE strain of 10% was achieved (i.e., $\lambda_1^{max} = 1.1$). The parallel model simulations were evaluated at a single displacement step of 10% for comparison. For both models, simulations were under quasi-static conditions, and stress-free boundaries were maintained in the transverse 2- and 3-directions. The following output measures were evaluated:

- Normal Cauchy stress (σ_{11}) from fibers and NFM

- Apparent Poisson's ratio of the composite RVE (v_{rve}) obtained by averaging the values in 1-2 and 1-3 directions:

$$v_{12} = -\frac{\ln\lambda_2}{\ln\lambda_1}, \qquad v_{13} = -\frac{\ln\lambda_3}{\ln\lambda_1} \tag{4-5}$$

where λ_1, λ_2 and λ_3 are stretch ratios in 1, 2 and 3 direction, respectively

- Average fiber stretch (λ_{fib})

- Fiber orientation measured using the axial component of the projected 2D orientation tensor, Ω_{11}:

$$\Omega = \frac{\sum l_i \begin{bmatrix} \cos^2\theta_i & \cos\theta_i\sin\theta_i \\ \cos\theta_i\sin\theta_i & \sin^2\theta_i \end{bmatrix}}{\sum l_i}, \quad \Omega_{11} = \frac{\sum l_i \cos^2\theta_i}{\sum l_i} \tag{4-6}$$

In addition, the coupled model was used to evaluate stress distributions (for the six unique components of the Cauchy stress tensor) on transverse slices through the RVE mid-section (i.e., in the 2-3 plane), as well as distributions of maximum and minimum principal stress and fiber stretch.

4.3 Results

In the coupled fiber-matrix model, stress due to the fiber network increased with increasing NFM shear modulus, and the non-linearity of fiber stress-strain curves became less pronounced at higher G values (Figure 4-3(a)). As one might expect, the matrix stress increased with increasing NFM shear modulus (Figure 4-3(b)), which accounted for much of the increase in total stress (Figure 4-3(c)). RVE Poisson's ratio decreased with increasing G, but increased with strain for G=10 and 110 Pa (Figure 4-3(d)). In addition to comparing model results computed at the same imposed strain, results were also evaluated at the same imposed total stress (in this case, 200 Pa). Matrix stress values
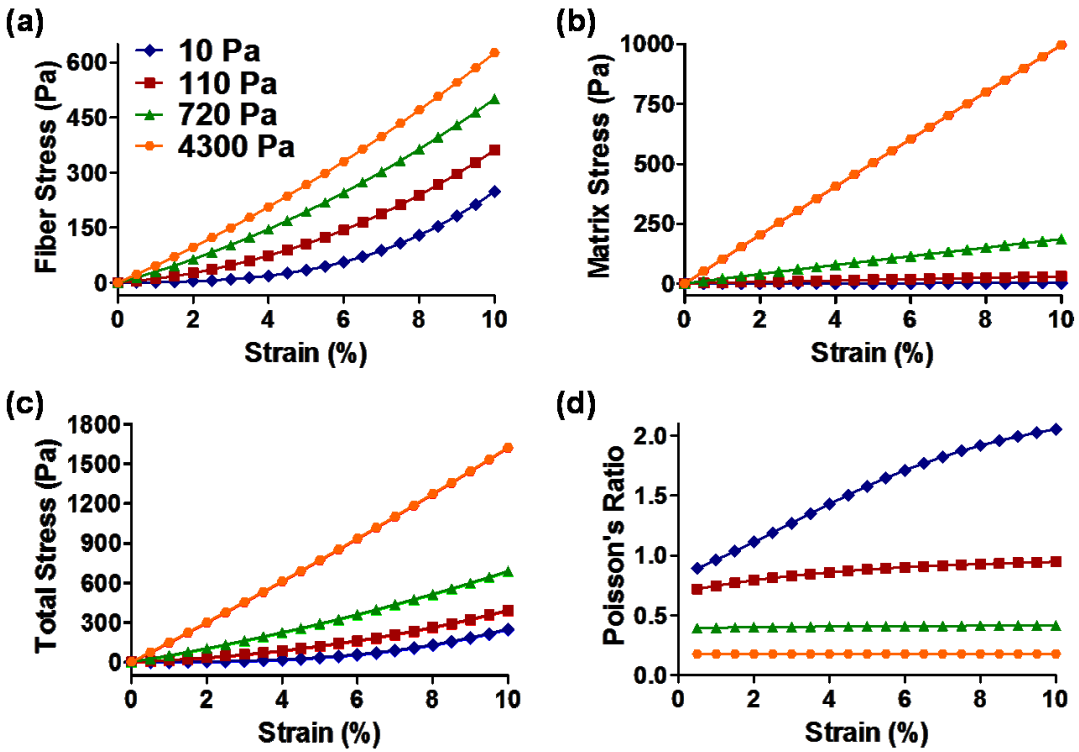
Figure 4-3: (a) Fiber stress, (b) matrix stress, (c) total stress, and (d) RVE Poisson's ratio vs. engineering strain for the coupled fiber-matrix model at varying values of NFM shear modulus; stress values increased with increasing *G*, particularly for the matrix, while Poisson's ratio decreased (data are representative results from a single network)

increased with increasing shear modulus for both cases (Figure 4-4(a)). In contrast, fiber stress values increased for the constant strain case, but decreased for the constant total stress case (Figure 4-4(b)), with the stiffer NFM shielding the collagen network.

Results from the coupled model were similar to those from the parallel model. Specifically, parallel and coupled models produced nearly identical average matrix stress values (Figure 4-5(a)). The coupled model exhibited smaller fiber stress values (Figure 4-5(b)), but both models showed similar fractions of total stress as a function of different *G* (Figure 4-5(c)). In both cases, when v_{nfm} was increased from 0.1 to 0.45, a slight increase

66
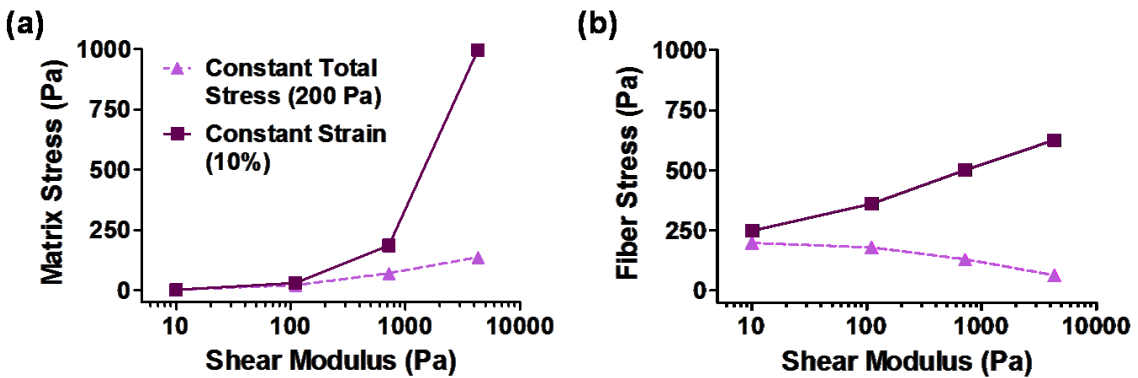
Figure 4-4: Magnitude of stress contributions differed depending on whether simulations were evaluated at constant total strain (solid lines) or constant total stress (dashed lines); (a) while matrix stress values increased in both cases, (b) fiber stresses show opposite trends for the two cases, where decreasing values for the constant-stress case demonstrates stress-shielding (by the matrix) at high shear moduli.
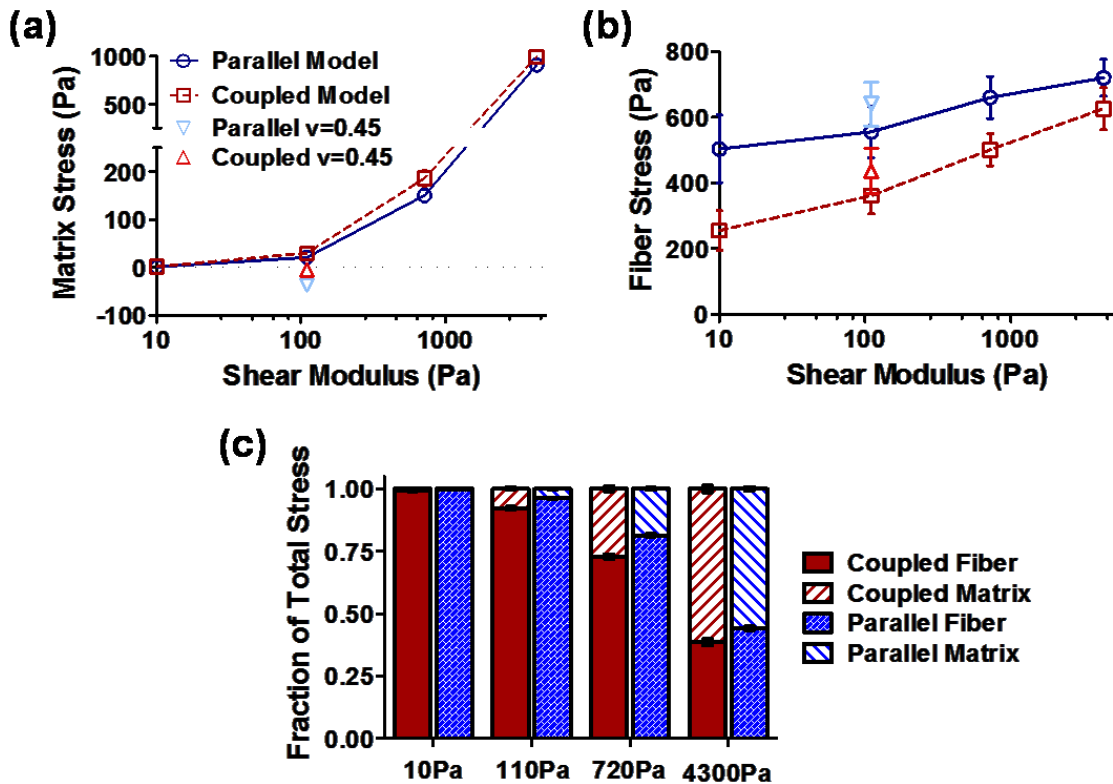
Figure 4-5: Average (a) matrix stress, (b) fiber stress, and (c) fraction of total stress at 10% strain and with v_{nfm}=0.1 show good agreement between the parallel and coupled models; stress values at a larger Poisson's ratio (i.e., v_{nfm}=0.45) at G=110Pa show a small shift of stress from the matrix to fibers (mean±95%CI; n=5)
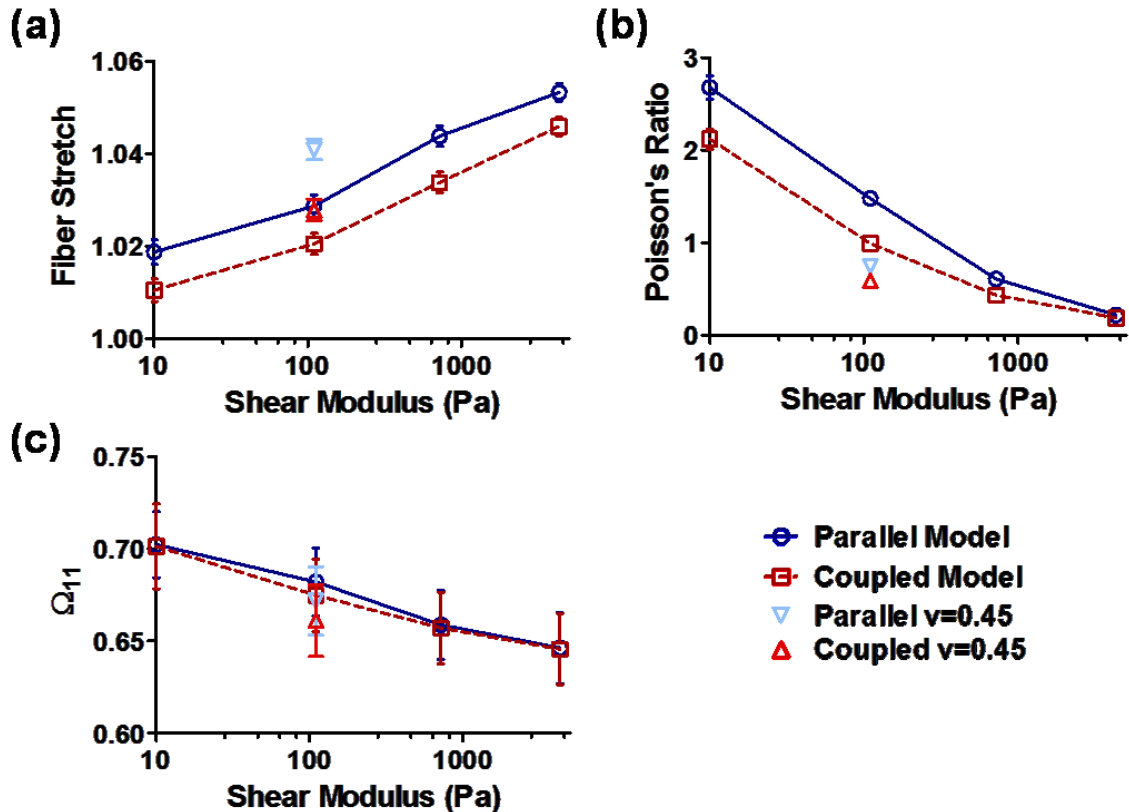
Figure 4-6: Average (a) fiber stretch, (b) RVE Poisson's ratio, and (c) Ω_{11} (representing fiber orientation in the loading direction) at 10% strain and with v_{nfm}=0.1 show decreased values for the coupled model compared to the parallel model, but similar qualitative changes as a function of increasing G; for the case where v_{nfm}=0.1 and G=110Pa, fiber stretch and Poisson's ratio increased and decreased, respectively, with no change in Ω_{11}; (mean±95%CI; n=5)

and decrease were seen in fiber and matrix stress, respectively, with no net change in total stress.

In addition to normal stresses in the loading direction, several other metrics were similar for the coupled and parallel models. Average fiber stretch increased with increasing G (Figure 4-6(a)), while v_{rve} (Figure 4-6(b)) and fiber orientation (represented via Ω_{11}; Figure 4-6(c)) both decreased with increasing G. For each of these output parameters, values were slightly smaller for the coupled model, but showed the same
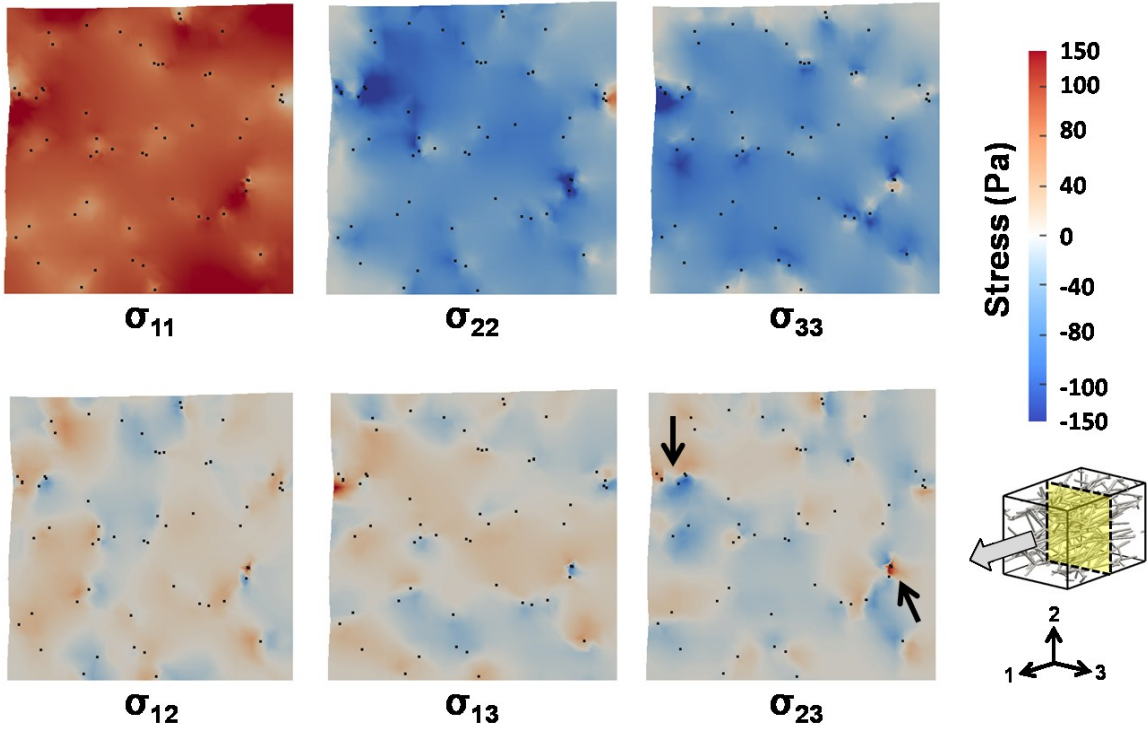
Figure 4-7: Interior normal and shear stress fields at 10% strain on the mid-section slice for a representative network (G=720Pa; v_{nfm}=0.1) demonstrates a highly inhomogeneous distribution for all six independent stress components; slices were cut normal to the loading (1-) direction in the 2-3 plane (represented by the dashed lines in the RVE schematic) and black dots indicate locations were fibers intersect the cutting plane; examples of two regions of high stress concentrations are indicated by arrows in σ_{23} plot.

patterns of change as a function of shear modulus. At high NFM Poisson's ratio (i.e., v_{nfm}=0.45), λ_{fib} and v_{rve} were slightly increased and decreased, respectively, with no change in Ω_{11}.

The use of the coupled model allowed for full-field quantification of the six independent Cauchy stress components of the matrix material, visualized via slice plots through the RVE midsection. Figure 4-7 shows representative plots for G = 720 Pa, where black dots represent intersection points between fibers and the cutting plane. Tensile normal stresses (i.e., positive values) were evident in the loading direction (σ_{11}), whereas compressive stresses were observed in the transverse axes (e.g., σ_{22} and σ_{33}) in
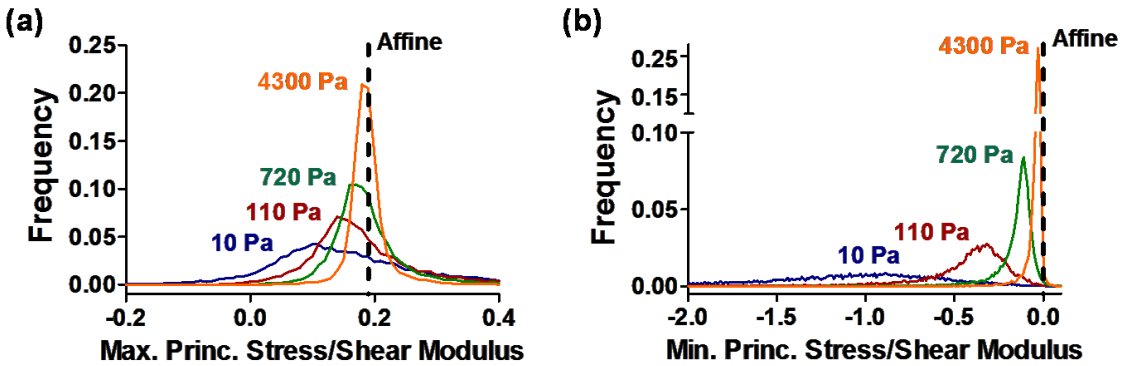
Figure 4-8: **(a) Maximum and (b) minimum principal stress (normalized by shear modulus of matrix material) distributions at 10% strain over all mesh elements of the matrix material; the mean value increased and the standard deviation decreased as *G* increased, with curves moving more towards the affine model (values from five networks lumped and plotted).**

response to the extreme tendency of the collagen network to contract in the unloaded directions. The stress distribution in the matrix material was highly inhomogeneous for all stress components. Normal stress values in the loading direction were smaller in the vicinity of multiple fiber intersection points. Stress concentrations (either positive or negative) occurred in locations where two or more fibers traversed the slice plane in close proximity.

The detailed mechanical response of the NFM in the coupled model was investigated by analyzing the distribution of maximum principal stresses (Figure 4-8(a)) and minimum principal stresses (Figure 4-8(b)) evaluated at the Gauss points of the matrix material mesh. As *G* increased, both the maximum and minimum principal stress distribution curves moved along the positive *x*-axis, indicating that more matrix elements experienced tension under applied stretch. The mean values of the distribution curves approached values corresponding to the affine model at higher G, along with decreasing spread (i.e., standard deviation). In the curve of minimum principal stress distribution

70
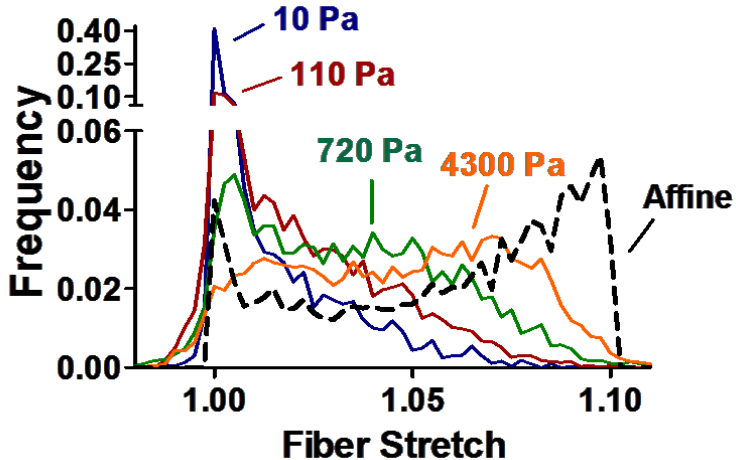
Figure 4-9: Distribution of fiber stretch values at 10% strain and with v_{nfm}=0.1; values concentrated near ~1 when _G_ was low (i.e. _G_=10Pa and 110Pa), but fibers were stretched to a greater extent at higher _G_ values, similar to what was shown in the affine model (values from five networks lumped and plotted).

(Figure 8(b)), nearly all values were negative, indicating that much of the NFM was in compression.

Distributions of fiber stretch values were plotted against varying shear modulus and compared to the affine model (Figure 4-9). For lower _G_ values (i.e. _G_=10Pa and 110Pa), a majority of fibers exhibited values of ~1 (i.e., unstretched). At higher shear modulus, fiber stretch values became more distributed, with a larger portion near the higher limit of the distribution, and demonstrated distributions that were increasingly similar to results from the affine model.

4.4 Discussion

A coupled fiber-matrix microstructural model was developed and utilized to explore the interactions between constituents in soft tissues subjected to tensile load. Specifically, Voronoi tessellations, representing collagen fiber networks, were embedded in a continuous non-fibrillar matrix, represented via tetrahedral finite elements, and coupled using a multi-dimensional mesh framework. In terms of the bulk properties and

71

overall RVE response, the coupled model yielded results consistent with those obtained using a simplified parallel model (Figures 4-5 and 4-6) described previously [104]. Thus, for investigations concerned only with average behavior, microstructural models that assume a superposition or rule-of-mixtures framework (e.g., [48,93,94,102–104]) may be sufficient. In cases where additional detail regarding inhomogeneities in NFM mechanics and/or quantification of fiber-matrix interactions are desired, however, a fully coupled model, such as the one developed in this study, can provide insight that is not attainable using a parallel-type model. One additional consideration important in model selection is relative computational cost. In this study, parallel model simulations ran in a few minutes on a standard desktop computer. In contrast, coupled model simulations of ~140,000 elements were much more expensive computationally, requiring ~20 CPU hours to converge using a high performance computing cluster.

In our previous study [104], a parallel fiber-matrix microstructural model was used to predict the mechanical response of collagen-agarose co-gels, which have been used as a simple experimental test system to quantify the contribution of non-fibrillar matrix to soft tissue properties [37,111]. In the present work, we compared the detailed coupled model to that parallel model. Both models predicted qualitatively the composition-dependent mechanical response of collagen-agarose co-gels in tension. Matrix stress (Figure 4-5(a)), total stress fraction (Figure 4-5(c)), fiber orientation (Figure 4-6(c)), and Poisson's ratio values (Figure 4-6(b)) agreed particularly well between the two models, while the coupled model demonstrated slightly lower mean fiber stretch (Figure 4-6(a)) and fiber stress values (Figure 4-5(b)) than the parallel model. This

72

discrepancy could be due to a mechanism wherein the matrix material has a stronger stress shielding effect on the embedded collagen network in the coupled model than in the parallel model. The stress shielding effect is revealed in Figure 4-4(b), in which fiber stress decreased as matrix material stiffness increased at constant stress.

Results obtained via the coupled model for bulk RVE properties were generally as expected. Stress values increased with strain, and both fiber and matrix stresses at a given strain increased with NFM shear modulus (Figure 4-3). A nonlinear toe-region was observed in the fiber stress-strain curve at small NFM modulus values, but nonlinearity was less pronounced at larger NFM modulus values. The tendency toward linearity is consistent with a stiffer NFM eliminating the non-affine, low-stretch reorientation of the fiber network (Figure 4-9). This difference in reorientation also explains the decreased lateral compaction, and hence Poisson's ratio, with increasing NFM stiffness. In addition, the nonlinear relationship of Poisson's ratio and strain at low G (Figure 4-3(d)) closely matched the relationship observed in experimental tests of collagen-agarose co-gels [37]. The bulk RVE stresses analyzed in this model were obtained from simulations at a constant strain value (e.g., 10% stretch). When results were computed at a constant total stress (200 Pa) for each of the varied simulations, fiber stresses decreased with increasing NFM modulus, demonstrating a stress shielding role of the NFM at large G.

A significant strength of the coupled model is its ability to quantify the internal RVE stress field and interaction between fiber and matrix materials. The embedded fiber network had a significant effect on the stress field of the surrounding matrix material, as demonstrated by the inhomogeneity of internal stress distribution (Figure 4-7). Tensile

73

normal stresses in the loading direction (σ_{11}) were relatively consistent across the RVEs, although smaller values were observed in the vicinity of multiple fiber intersection points. Compressive normal stresses in traverse directions (i.e., σ_{22} and σ_{33}) were caused by fibers squeezing the surrounding matrix material in the lateral direction during reorientation. Due to the Poisson effect, matrix material being compressed in the lateral directions was concurrently stretched in the loading direction, thereby decreasing the local tensile stress and leading to smaller σ_{11} values in areas of concentrated fiber intersection points. Finally, maps of internal shear stresses demonstrated complex patterns (Figure 4-7(bottom)), with areas of particularly high shear stress co-localized with significant fiber clustering. In presenting these stress field plots, we acknowledge that the magnitudes of the stresses contained therein have not been validated. To date, only the boundary (average) stresses of the coupled model have been matched experimentally since we do not yet have experimental data describing internal stresses, but we believe the pronounced inhomogeneity of the stress fields presented here to be real While the <u>magnitude</u> of stress values in areas of stress concentration (e.g., where many fibers intersect the cutting plane) may be subject to numerical error, and could potentially be better converged with additional mesh refinement, the <u>locations</u> of these higher stress values are correct and informative. Our interpretation thus focuses on location and relative stress magnitudes instead of absolute magnitudes, which may not be accurate. Novel experimental techniques (e.g., 3D traction force microscopy [116]) may allow future estimation of internal stress fields in multicomponent tissues and more complete testing of this coupled microstructural model.

A defining characteristic of large-network simulations, in which fibers function in a fully-interacting organizational structure, is non-affine fiber kinematics [105]. After incorporating matrix material with the fiber network in this coupled model, we investigated how the NFM altered the relative affinity of the materials in the composite RVE. Distributions of maximum/minimum principal stress of the matrix material normalized by NFM shear modulus showed a transition from non-affine to affine behavior as the modulus increased (Figure 4-8). With higher matrix stiffness the system became dominated by the NFM, with more matrix stress values approaching the affine case. In other words, as the shear modulus increased, the composite response transitioned from a fiber-dominated to a matrix-dominated response. The matrix material also altered the kinematics of the embedded fiber network (Figure 4-9). At low shear modulus, the NFM had less ability to prevent fibers from reorienting to the load direction, which resulted in minimal stretching of fibers as seen by the high frequency of fibers with low stretch values of ~1. With smaller matrix stiffness, the energy minimization of the matrix-fiber system was achieved mainly through fiber reorientation, which requires less work than fiber stretching. As the matrix stiffened and became more dominant, the fibers tended to stretch with their surrounding matrix material, leading to a higher frequency of large fiber stretch values (i.e., $\lambda_{fib} > 1.05$).

In developing both the parallel and coupled models, several limiting assumptions were made. First, in both models, collagen fibers were treated as one-dimensional springs. Several of our previous studies using this same assumption [14,48,104,117,118] as well as those of others [119–121] have been very successful in matching experimental

75

data, so as a first step in developing the coupled fiber-matrix model presented here, the one-dimensional spring assumption was maintained. Fiber bending (as examined by others [107,122,123] in network-only models) and different types of interactions between fibers and matrix (e.g., sliding, breaking) could be significant under some loading conditions. Second, the simulations in this study were based on a quasi-static tensile test to 10% maximum strain, with no viscoelastic or poroelastic contributions to the mechanical response. Poroelasticity and viscoelasticity of collagen gels have been examined previously by our group [77,101,111,124] and others [29,125–128] and are an important part of the complete picture of collagen gel behavior and, perhaps even more so, soft tissue mechanics. It must be emphasized that the current work focuses only on quasi-static behavior and therefore provides insight into only some aspects of the mechanical response.

In conclusion, by providing detailed descriptions of the inhomogeneities and direction-dependence of internal RVE stress fields, the fully-coupled model has many potential applications, such as quantifying the local environment of cells or examining microscale local failure of tissues by stress concentration. Compared to a parallel model framework, however, the coupled model is much more computationally expensive. Since both of these models provide good predictions in terms of gross average parameters (e.g., fiber orientation parameter, averaged stresses, etc.), parallel-type models are suitable, and even preferable, if specific details on fiber-matrix interactions are not needed.

5. Fiber Network + Interstitial Matrix Interactions II: Experimental Characterization of Collagen Pre-Stress Using Collagen-Hyaluronic Acid Co-gels

5.1 Introduction

Collagen gel tissue-equivalents (TEs), which are simple model tissues with tunable properties, have been used to explore many properties of soft tissues, such as how structural and compositional properties affect mechanical function [37,111,129,130]. One aspect not captured in previous TE formulations is residual stress due to interactions among components with different mechanical rest states, which has an important functional role in many tissues (e.g., blood vessels [131], ligaments [132], annulus fibrosus [133]). Since the *in vivo* stress state of native tissues is not easily replicated in TE fabrication, a different method for "pre-stressing" collagen networks of TEs was necessary.

To this end, co-gel TEs were fabricated by adding hyaluronic acid (HA) to reconstituted Type-I collagen (Col) gels. HA is a glycosaminoglycan found in various connective, epithelial and neural tissues; it serves different functions, such as a lubrication in articular cartilage [134] and participation in the inflammatory response during wound healing [135]. HA is a linear polysaccharide comprised of alternating N-acetyl-β-D-glucosamine and β-D-glucuronic acid residues (see [136] for its chemical structure). Its inherent advantages of biocompatibility and the ability to elicit desirable

cellular responses such as cell proliferation [137,138] and migration [139] have made HA a biomaterial of interest for various biomedical applications such as tissue engineering [139–141] and drug delivery [142,143]. Use of soluble HA on its own, however, is limited by its low mechanical strength and rapid degradation. As such, to improve its mechanical properties, HA is often chemically modified or cross-linked [144], or co-gelated with other extra-cellular matrix molecules such as collagen [139,141,145,146]. Because of the high fixed-charge density (one charged carboxyl group per disaccharide monomer unit), HA gels swell in hypertonic solutions due to the buildup of osmotic pressure arising from the Donnan effect [147]. In this work, we utilize the swelling properties of HA gels to induce a pre-stress in a collagen network: when placed in solutions of varying osmolarity, HA-Col TEs swell by HA hydration, which in turn stretches (and stresses) the collagen network. In this way, TEs with residual stress (i.e., pre-stressed collagen fibers) can be fabricated and evaluated in order to elucidate relationships between residual stress and functional properties. In the pres-stressed HA-Col gel, the HA is pressurized by the osmotic effect and constrained by the collagen network, and the collagen is stretched by the HA until the tension in the collagen network is balanced by the HA swelling stress. Therefore, the goals of the present study were to fabricate HA-Col TEs, to make initial measurements of their swelling properties, and to quantify the amount of pre-stress introduced in the collagen network.
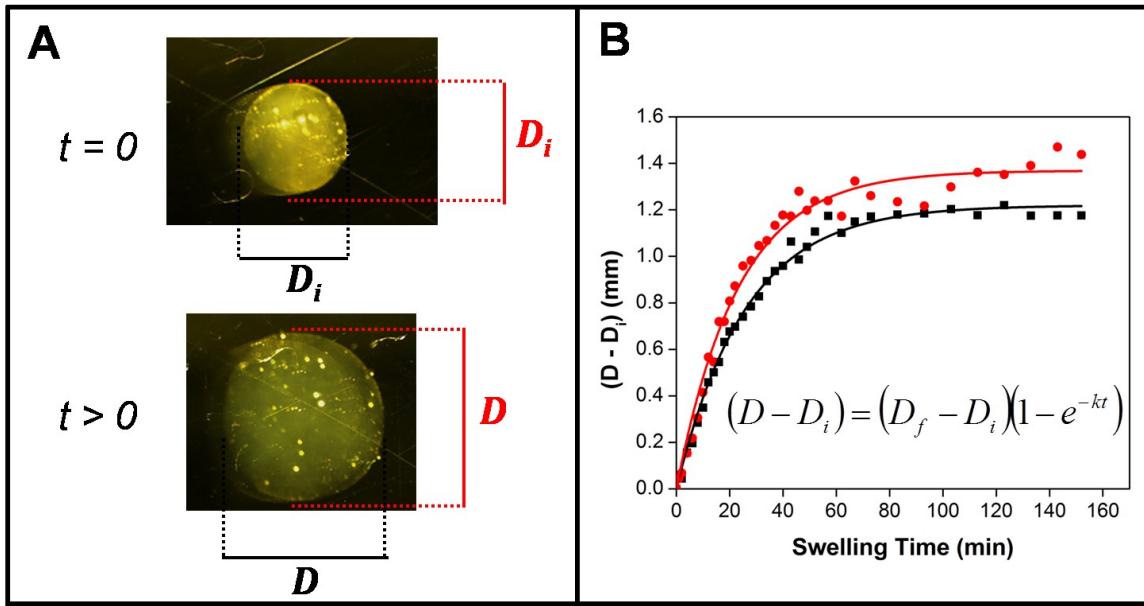
Figure 5-1. (A) Spherical gel before and after swelling; sphere diameters were computed in 2 orthogonal directions (shown in red and black). **(B)** Example of the exponential curve fits for each gel to experimental data to obtain the swelled sphere diameter, *D_f*, and characteristic swelling time, *1/k*.

5.2 Materials and Methods

5.2.1 Sample Fabrication

Three groups of TE gels were fabricated: Pure collagen (Col), pure HA, and HA-Col co-gels. For collagen, reconstituted Type-I rat tail collagen (Invitrogen, Carlsbad, CA) was mixed as described previously [59] with 1M HEPES, 1M NaOH, 10X MEM, FBS, Penicillin/Streptomycin, Fungizone, and L-Glutamine, and diluted with DI water to a final concentration of 1 mg/mL. HA samples were prepared by mixing thiol-modified HA (Biotime, Inc., Alameda, CA) with a polyethylene glycol based thio-reactive cross-linker to form a 0.67% (w/v) HA gel. HA-col TEs were prepared by mixing equal volumes of Col and HA (with cross-linker) solutions, such that final concentrations for each component were consistent with the single-component gels. After the solutions were

79

made, 10-µL droplets of each gel type were cast in silicone oil and incubated at 37°C for 24 hours to create spheres of ~2.5mm diameter, similar to the procedure in [148].

5.2.2 Swelling Experiments

After incubation, spheres were placed in solutions of 0, 25, 50, 75 or 100% 1x phosphate buffered saline (PBS, Mediatech, Manassas VA, mixed with deionized, distilled water, n≥3 per solution) and allowed to swell for 150 minutes with images captured every 2 minutes. Sphere diameters were computed as the average of 2 orthogonal directions (Fig. 5-1A) and an exponential curve was fit to the data (Fig. 5-1B) to compute the equilibrium swelling ratio (D_f/D_i) and the characteristic swelling time ($1/k$) for each sample.

5.2.3 Tensile Testing

Ring-shaped samples were formed by injecting 700 µL of gel solution into two-piece circular molds and incubating at 37°C for 24 hours. Samples were mounted on T-shaped grips of an Instron mechanical testing machine for uniaxial tensile testing while submerged in 100% PBS. After application of a 14.5 mm step-displacement to remove slack, samples were stretched at 0.2 mm/second until failure. Using initial gel dimensions (measured optically) and actuator displacement, the 1st Piola-Kirchoff stress and Green strain were computed for each sample.

5.2.4 Data Analysis

The fixed charge density of HA before swelling, c_F^0, is estimated by

$$c_F{}^0 = \frac{|z_{HA}|C_{HA}}{MW_{HA}} \qquad\qquad (5\text{-}1)$$

where z_{HA} is the charge per HA monomer, C_{HA} is the mass concentration of HA, and MW_{HA} is the molecular weight of a HA disaccharide monomer. For a HA concentration of 6.67mg/mL, with $|z_{HA}| = 1$ and $MW_{HA} = 379$g/mol, $c_F^0 = 0.0176$M. The superscript '0' indicates the fixed charged density of an unswelled HA gel. Since the HA gels are dilute (0.667% w/v), the fixed charge density after swelling, c_F, is calculated by

$$c_F = c_F{}^0 \frac{V_0}{V} \tag{5-2}$$

where V_0 and V are the volumes of the HA gel before and after swelling, respectively.

For a HA solution immersed in a external bath solution containing monovalent ions, e.g., NaCl, the Donnan osmotic pressure, π_{Donnan}, can be computed as [147,149]

$$\pi_{Donnan} = RT\Delta c = RT\left(\sqrt{c_F{}^2 + 4c^{*2}} - 2c^*\right) \tag{5-3}$$

where R is the universal gas constant, T is the temperature of the solution, c* is the concentration of Na^+ in the external solution. For a swollen HA gel at equilibrium, the Donnan osmotic pressure is balanced by the hydrostatic stress in the HA gel, σ_{HA}:

$$\sigma_{HA} - \pi_{Donnan} = 0 \tag{5-4}$$

Similarly, a swollen HA-Col gel at equilibrium, under the assumption that the co-gel obeys constrained mixture theory, satisfies the following stress balance:

$$\sigma_{HA} + \sigma_{Col} - \pi_{Donnan} = 0 \tag{5-5}$$

where σ_{Col} is the stress in the collagen network, and π_{Donnan} calculated using equation 5-1.

The method for calculating the stress in the collagen network, σ_{Col}, is as follows. From the swelling data for the pure HA gels in solutions of varying osmolarity, σ_{HA} was computed using the equilibrium condition in equation 5-4, and the osmotic pressure from equations 5-1 to 5-3. The σ_{HA} vs. V/V_0 curve was subsequently used to estimate the stress
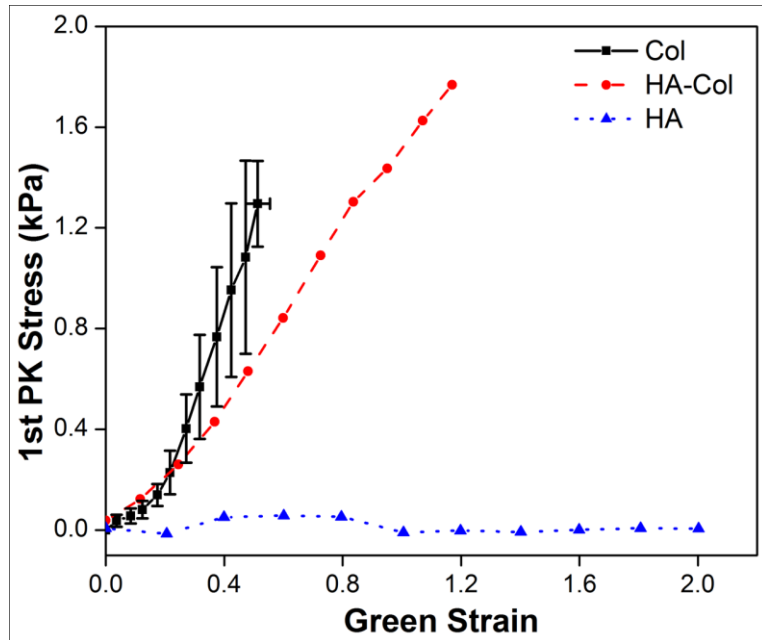
Figure 5-2. Average stress-strain curves for Col, HA, and HA-Col gels. HA gels exhibited negligible mechanical strength. HA-Col response showed a smaller toe region, and higher stress and strain and failure compared to Col. Error bars for Col = 95%CI, n = 6.

contribution by the HA (σ_{HA}) in the HA-Col gels from the equilibrium swollen size of the HA-Col gels. With π_{Donnan} calculated from equations 5-1 to 5-3, the collagen stress could be found using equation 5-5.

5.3 Results

As measured via ring tensile tests, Figure 5-2 shows that the average stress-strain curve of the Col gels (n=5) was highly nonlinear, while HA (n=1) demonstrated very low mechanical strength yet high extensibility (The HA gel did not fail even at a Green Strain of 3; only data up to a Green Strain of 2 was plotted). Key observations from Figure 5-2:

- HA-Col gels are more extensible

- HA-Col gels have higher stress at failure

82
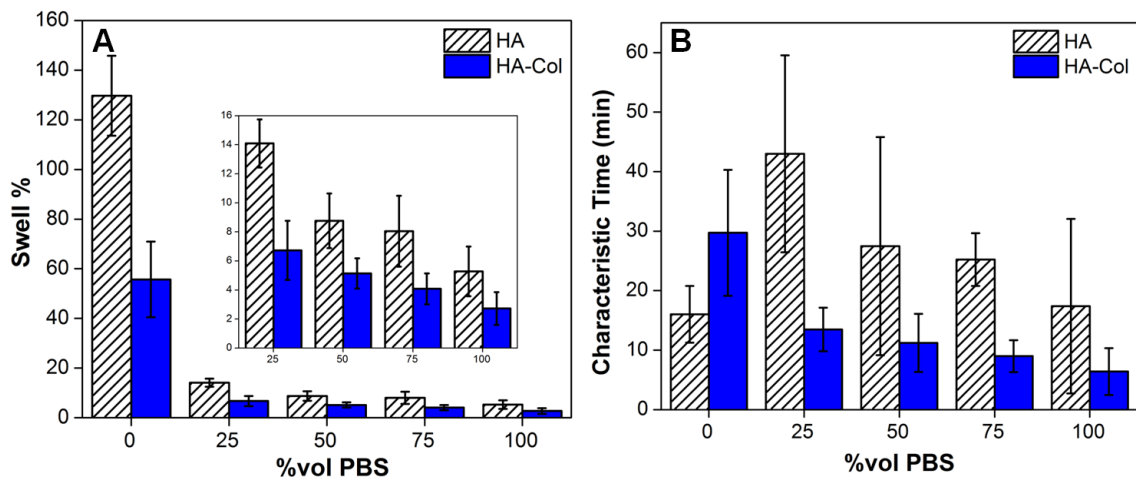
Figure 5-3. (A) Swelling percentages of HA and HA-Col gels showed a decreasing trend with increasing %vol PBS. In all solutions, the HA gels swelled to a larger extent (~40 – 60%) compared to the HA-Col gels. (B) Average characteristic times showed that HA-Col gels exhibited a decreasing trend with increasing PBS concentration. For the HA gels, however, the gels swelled in 0vol% PBS showed the shortest characteristic time. Error bars = 95%CI, n ≥ 6 in each case.

That the HA-Col stress-strain response was not identical to that of the Col gels, since the pure HA gel exhibited negligible mechanical strength, strongly suggest microstructural differences in the collagen network in the HA-Col co-gels.

Figure 5-3A shows the swelling ratio for HA and HA-Col gels in the 5 different concentrations of PBS; pure collagen gels did not swell in any of the solutions (data not shown). In all solutions, the HA gels swelled to a larger extent (~40 – 60%) than the HA-Col gels. In addition, the swelling ratio decreased with increasing PBS concentration for both HA and HA-Col gels, with the largest decrease occurring from 0%vol PBS to 25%vol PBS (>8x in both cases). Comparison of characteristic swelling times (Figure 5-3B) showed that the HA-Col gels exhibited a decreasing trend in characteristic swell time with increasing PBS concentration. For the HA gels, however, the gels swelled in 0vol% PBS showed the shortest characteristic time; this unexpected result, coupled with the
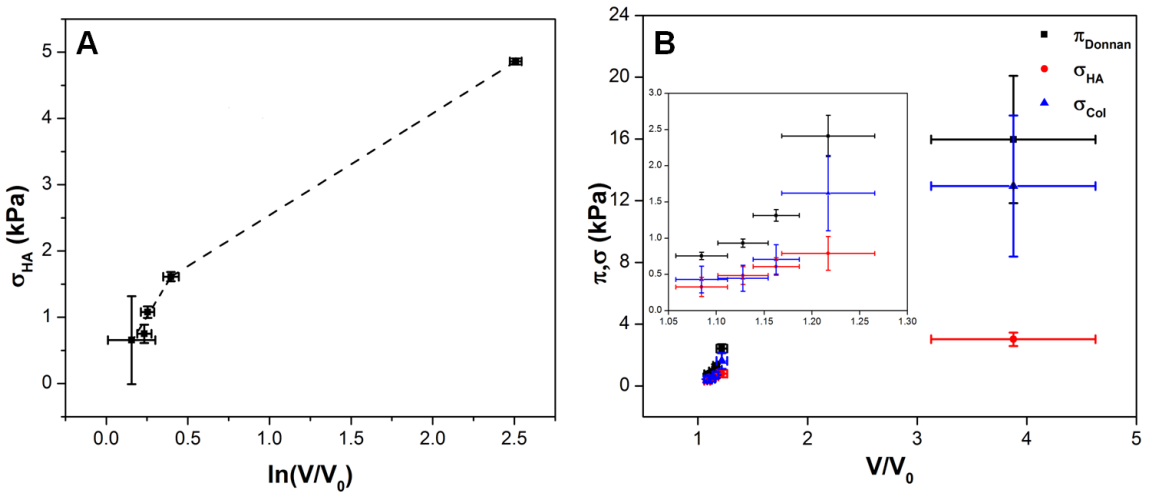
Figure 5-4. (A) Average σ_{HA} from swelling of pure HA gels showed increasing values with swelling percentage; the largest difference in swelling percentage occurred between gels swelled in 0vol% PBS and 25vol% PBS. **(B)** Relative magnitudes of σ_{HA}, π_{Donnan}, and σ_{Col} from swelling of HA-Col gels; the linear stretch exerted on the collagen network (approximated by $(V/V_0)^{1/3} = 1.6$) exceeded the average stretch at failure for pure collagen gels of the same concentration from Figure 5-2. Error bars = 95% CI, $n \geq 6$ in all cases.

largest swelling percentage for these HA gels, meant a very fast swelling rate for pure HA gels in 0vol% PBS.

Figure 5-4A shows the hydrostatic stress in the HA with change in volume of the HA gel. At volume changes of ≤50% (i.e., $\ln(V/V_0) \leq 0.4$), σ_{HA} increases linearly with $\ln(V/V_0)$. Data obtained for the HA gels swelled in 0vol% PBS deviated from this linear trend; work is in progress to obtain intermediate data points using external solutions between 0vol% and 25vol% PBS. By extrapolating the data from Figure 5-4A, σ_{HA} was estimated for the HA-Col co-gels, and the collagen pre-stress, σ_{Col}, calculated using equation 5-5. The relative magnitude of each stress contribution is shown in Figure 5-4B. As expected, the stress induced in the collagen network increased with swelling percentage. For the HA-Col gels which exhibited the largest swelling percentage (i.e., those immersed in 0vol% PBS), the linear stretch exerted on the collagen network (approximated by $(V/V_0)^{1/3} = 1.6$) exceeded the average stretch at failure of ~1.5 for pure

84

collagen gels of the same concentration under uniaxial stretch [150]. This surprising result was similar to the tensile test results in Figure 5-2 which showed higher strain at failure for the HA-Col gel. Whether the enhanced extensibility of the collagen network in the HA-Col gels were due to alterations in collagen network architecture (e.g., fibril tortuosity, cross-link density), or because of interactions between the HA polymer chains with the collagen network, remains unclear and warrants further investigation.

5.4 Discussion and Future Work

The primary purpose of this study was to fabricate tissue-equivalents composed of a collagen fiber network and hyaluronic acid and to evaluate their potential use as an experimental model system to study residual stress in soft tissues. We successfully created three gel types (Col, HA, and HA-Col). Initial evaluation has shown that HA-Col TEs constitute a useful experimental model system to examine residual stresses in soft tissues for the reasons outlined below.

First, each component of the HA-Col samples appears to be responsible for a specific behavior of the composite gels. Specifically, Col gels do not swell (regardless of osmolarity), but the addition of HA results in a concentration-dependent swelling response. In addition, HA samples exhibited negligible mechanical resistance subjected to uniaxial tensile tests, but Col samples demonstrated strong mechanical properties. Thus, the collagen network imparts mechanical strength and the HA component modulates the swelling response.

Second, HA-Col gels have a very simple formulation, which is ideal for a model system. While our ultimate goal is to understand the mechanism and consequences of

residual stress in native tissues, the compositional and organizational properties of native tissues are often very complex, making the characterization and separation of contributions difficult to ascertain. With a simple model system (in this case, acellular gels with only two constituents and water), properties and relationships are more easily discerned and described.

Third, the chosen method of achieving residual stress within the collagen network (i.e., osmotic swelling) is physiologically based and an important contributing factor in native tissues. In a mathematical investigation on the origins of residual stress in soft tissues, Lanir [151] reported that published data and experimental observations demonstrate that "osmotic-driven tissue swelling is a predominant residual stress producing mechanism." So, although the composition and organization of the HA-Col TE system does not directly mimic a particular tissue of interest, the method of inducing residual stress is based on a biologically relevant mechanism.

With the establishment of this TE model system, future work will replicate the uniaxial tensile tests of the ring samples performed in this study, but in baths of varying osmolarity after allowing samples to reach swelling equilibrium. These experiments will elucidate differences in mechanical response as a function of swelling (and hence, residual collagen network stress). In addition, other imaging modalities (e.g., confocal and scanning electron microscopy) will be utilized to visualize and quantify the degree to which the collagen fibers within the TE samples are stretched for a given amount of gel swelling. Ultimately, such investigations will provide insight into the role of residual stress in functional properties of biological soft tissues.

6. Fiber Network + Cells: A Multiscale Approach to Modeling the Passive Mechanical Contributions of Cells in Tissues

The content of this chapter was published in the Journal of Biomechanical Engineering (July 2013) as *"A Multiscale Approach to Modeling the Passive Mechanical Contributions of Cells in Tissues"*.

6.1. Introduction

Understanding the mechanics of biological and bioengineered tissues is difficult; unlike synthetic composite materials (e.g. laminates), tissues are comprised of different components (cells, fibrous protein networks, proteoglycans) that are distributed inhomogeneously, exhibit non-linear mechanical behavior [81,152] , and can be highly anisotropic. In particular, cells play a complex role in the mechanics of native and bioengineered tissues. In addition to a *passive* component of cells as inclusions within an extracellular matrix (ECM), *active* mechanical contributions also exist from the interactions between cells with the surrounding ECM (e.g., compaction, remodeling).

Early phenomenological and continuum modeling approaches to understand tissue biomechanics (e.g., [81,153]) considered both the cell and the matrix as continuous materials. Evolution of such models has generally involved incorporation of microstructural detail and/or cellular phenomenon to develop improved constitutive laws, e.g., models that incorporate fiber orientation distributions to capture anisotropic behavior of the ECM surrounding the cells [88,154,155], incorporation of "anisotropy tensors" to account for cell orientation within a tissue [12,13,156,157], or a mathematical model motivated by localized variations in the pericellular region [158,159]. In addition, multi-level finite element approaches have been used to account for tissue inhomogeneity

by discretizing cells from the surrounding ECM to consider cells as separate entities [160]. While such models have had some success in predicting tissue mechanics, the lack of microstructural detail in their formulation limits their ability to explore the respective contributions and interactions between different components within a tissue. In contrast, structural approaches attempt to understand tissue biomechanics by incorporating microstructural details directly into the model to elucidate composition-structure-function relationships in biological tissues. One such model is the tensegrity approach by Ingber and co-workers, who proposed that cytoskeletal filaments and the ECM form a tensegrity structure in combination with one another [161–164]. The cellular solid model considered the cytoskeletal filaments as struts forming the edges of a cubic cell that can bend and stretch under deformation [165–167]. Biopolymer models [168,169] utilize flexible polymer theories by treating the single segments of the network as worm-like chains; Boyce and co-workers extended the concept to create an eight-chain volume-averaged network model [170]. The above-mentioned models, while beginning to incorporate network microstructure detail into the model formulation, contain simplified network representations that assume ordered periodicity within the network.

Research in our group focuses on developing a comprehensive model to predict the mechanical behavior of biological and bioengineered tissues via a multiscale approach, with the fibrillar components of the ECM represented as large random interconnected networks. Multiscale modeling allows integration of the microstructural details of different components into the modeling framework, hence capturing better the structural and mechanical complexities that exist in a tissue, and relating structure and

mechanics on the microstructural level to overall tissue mechanics at the macroscopic level. Recent efforts in extending this model have focused on the ECM, with the fibrous material (e.g. collagen) represented by a fiber network, and other non-fibrous components (e.g. proteoglycans) represented as a solid Neo-Hookean material. This framework has been successfully used to model tissues and tissue equivalents, e.g., arteries [48], collagen-agarose co-gels [104,171], as well as model tissue damage [117]. A significant gap in this model, however, is the absence of cells, which are integral components in most tissues. The current work represents an improvement of the multiscale model via the addition of cells, and investigates the *passive* mechanical contribution of cells to overall tissue mechanics. As such, it constitutes an extension of our early study on passive cellular contribution based on Hashin's solution [15] for a composite of rigid inclusions in a homogeneous, linear, and isotropic elastic matrix.

6.2. Materials and Methods

6.2.1 Multiscale Model Formulation

Cells were modeled as dilute, non-interacting spherical inclusions embedded within a fibrous ECM network. Cells were assumed to be dilute and non-interacting, such that they could be considered as organized in a periodic lattice (Figure 6-1A). As such, a simplified mesh geometry containing a sphere in a box was sufficient to describe the cell-matrix system. Finite element mesh generation was performed in ABAQUS (Dassault Systèmes Americas Corp., Waltham, MA); the cell was represented by an eighth of a sphere contained within a cube, with three symmetry planes as shown in Figure 6-1B. Three mesh geometries, corresponding to 5, 10, and 15% cell by volume, were created.
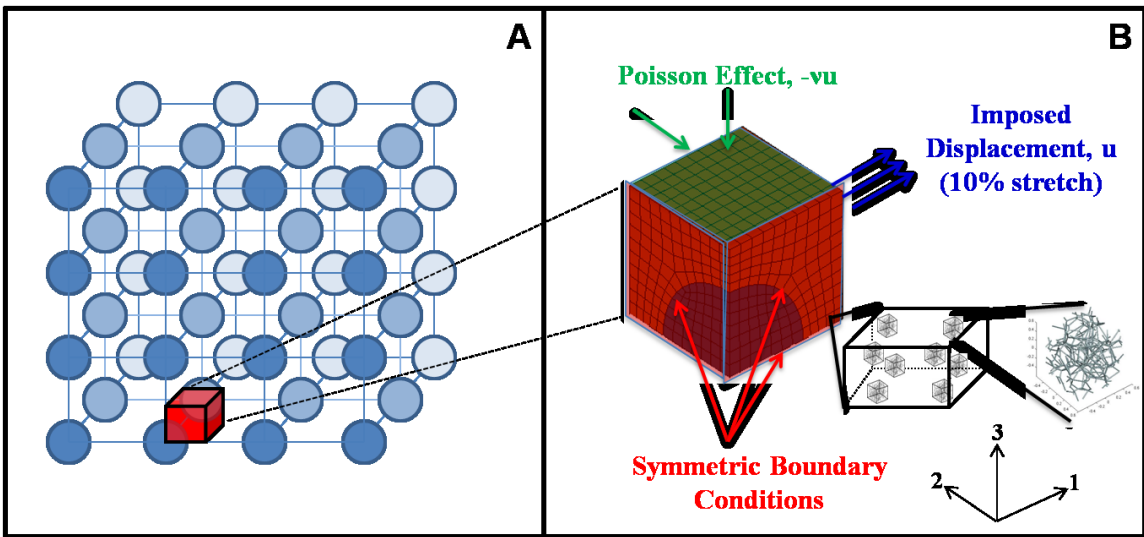
Figure 6-1. (A) Schematic representation of cells within a tissue organized in a periodic lattice, based on the assumption that cells are dilute, non-interacting, and spherical in shape. (B) Finite-element mesh showing boundary conditions and three symmetry planes. In the multiscale formulation, each Gauss point in every element is associated with a unique representative volume element (RVE) comprised of a random, interconnected network.

For each case, tensile tests of up to 10% stretch in the *1*-direction were simulated by imposing displacement of 0.5% stretch per step on the positive *1*-face over 20 steps; stress-free boundary conditions were prescribed on the positive 2- and 3- faces by allowing compaction on these faces (Figure 6-1B).

Our multiscale model couples the macroscopic scale (i.e. finite element mesh representing the tissue level) with the microscopic scale (representing the fibrous ECM network) via volume-averaging; a summary of the methodology is described here, with more detailed description found in [38,39]. Briefly, each of the eight Gauss points in every element is associated with a unique representative volume element (RVE) comprised of a network of randomly oriented fibrils (Figure 6-1B), with the fibrils interconnected at cross-links represented by freely-rotating pin-joints. Initial guesses for the displacements of each RVE boundary are determined by linear interpolation of the

nodal displacements to every Gauss point within the element; in turn, these nodal displacements are determined by the imposed macroscopic boundary conditions as described in Figure 6-1B. Force balances within each RVE are solved instead of a constitutive equation at each Gauss point. At static equilibrium, the vector sum of forces exerted by fibrils connected at each cross-link is zero, and the macroscopic (averaged) RVE Cauchy stress tensor, σ_{ij}^{macro}, can be computed by the forces exerted by the fibrils on the RVE boundaries:

$$\sigma_{ij}^{macro} = \frac{1}{V}\int_V \sigma_{ij}^{micro}dV = \frac{1}{V}\sum_{\substack{boundary \\ crosslinks}} x_i F_j \tag{6-1}$$

where V is the RVE volume, x_i is the i-th component of the coordinate where the fibril intersects the boundary, and F_j is the j-th component of the force acting on the boundary by the fibril. σ_{ij}^{micro} is the microscopic stress tensor of individual fibrils in the network; for a single fiber intersecting with a boundary,

$$\oint_{dV} \sigma_{ij}^{micro}n_i dS = F_j \tag{6-2}$$

where F_j is as defined above, and n_i is the unit normal of the boundary intersected by the fibril in question. The force exerted by each fibril, F, is governed by the exponential constitutive equation [4,40]:

$$F = \frac{A}{B}\left(exp(BE_f) - 1\right) \tag{6-3}$$

In the above equation, A and B are material constants for each individual fibril. The constant A is a measure of fibril stiffness, and B captures the degree of non-linearity in

mechanical behavior of individual fibrils. E_f is the fibril Green strain computed from the fibril stretch ratio, λ_f:

$$E_f = \frac{1}{2}(\lambda_f^2 - 1) \tag{6-4}$$

At small strains (i.e., as $\lambda_f \to 1$), a Taylor series expansion around $E_f = 0$ reduces equation 3 to a linear elastic fibril. The components of this force in each direction (F_j in equation 1) are computed by multiplying the force F (in equation 3) with the respective directional cosines for each fibril. Solving the macroscopic force balance yields the following expression for the divergence of the macroscopic Cauchy Stress tensor:

$$\sigma_{ij,i}^{macro} = \frac{1}{V} \oint_{dV} \left(\sigma_{ij}^{micro} - \sigma_{ij}^{macro}\right) u_{k,i} n_k \, dS \tag{6-5}$$

where u_k is the RVE boundary displacement and n_k is the unit normal vector, and σ_{ij}^{macro} defined in equation 1; equation 2 allows calculation of the integral of σ_{ij}^{micro} in terms of the boundary forces. The final deformation of each RVE at each Gauss point is dependent on the solution of equation 5 upon convergence.

2.2 Model Specification

2.2.1 Rigid Cell

Cells were first modeled as rigid inclusions by fixing all the nodes in the spherical region of the mesh. These simulations were motivated by our previous work on fibroblast-populated collagen gels, which compared experimental data to an analytical solution of an inclusion-based model [15]. While we acknowledge that cells are generally deformable, this set of simulations allowed for direct comparison between our multiscale model predictions and this analytical solution. Developed by Hashin, this theory of linear

elastic spherical inclusions embedded in an elastic, homoegeneous, isotropic matrix gave analytical expressions for approximating the composite bulk modulus (K^*) and shear modulus (G^*) from material constants of the inclusion (K_p, G_p), matrix (K_m, G_m, Poisson's ratio v_m), and volume fraction of inclusions (c). In the limit of rigid inclusions (i.e. K_p, $G_p \rightarrow \infty$), these expressions reduce to [172]

$$\frac{K^*}{K_m} = 1 + \frac{3(1 - v_m)c}{(1 + v_m)(1 - c)} \tag{6-6}$$

$$\frac{G^*}{G_m} = 1 + \frac{15(1 - v_m)c}{2(4 - 5v_m)(1 - c)} \tag{6-7}$$

Three different cases were considered for the surrounding ECM: (1) linear elastic material (Hookean), (2) hyperelastic material (Neo-Hookean), and (3) a network of fibers, using our multiscale model as described above. Simulations for these three ECM cases were performed with rigid cell volume fractions of 0%, 5%, 10% and 15%. In the no-cell case (i.e., 0% cell volume fraction), results for the linear elastic and Neo-Hookean matrix cases were obtained directly from their respective constitutive equations (equations 8 and 9 below); for the case of the ECM containing a network of fibers, the mesh for 5% cell volume fraction was used, with all elements (including the cell elements) assigned as ECM elements. The linear elastic matrix was governed by Hooke's law:

$$\sigma_{ij}^{matrix} = 2G_m \varepsilon_{ij} + \frac{2G_m v_m}{(1 - 2v_m)} \varepsilon_{kk} \delta_{ij} \tag{6-8}$$

where ε_{ij} is the small strain tensor. These simulations were run in Matlab (The Mathworks, Inc., Natick, MA) using a custom code. The form of the Neo-Hookean equation used is [48,173]

93

$$\sigma_{ij}^{matrix} = \frac{G_m}{J}\left(B_{ij} - \delta_{ij}\right) + \frac{2G_m v_m}{J(1 - 2v_m)}(\ln J)\delta_{ij} \qquad (6\text{-}9)$$

where J is the determinant of the deformation tensor $F_{ij} \equiv \partial x_i/\partial X_j$, and B_{ij} is the left Cauchy-Green deformation tensor given by $B_{ij} = F_{ik}F_{jk}$. For these elastic models, the matrix shear modulus was set at G_m= 4.2kPa, similar in magnitude to the value used to model the non-fibrillar matrix of the arterial wall [48,174]. While soft tissues typically exhibit high Poisson's ratios in tension, often values greater than 1 [175–177], equations (6) to (9) are governed by elasticity theory and are only valid for Poisson's ratios ranging between -1 and 0.5; as such, the matrix Poisson's ratio was set at v_m = 0.3 for these models.

For an ECM comprising of a fibrous network, a Voronoi network of fibrils was used, generated from Voronoi tessellation about random seed points. Voronoi networks have a connectivity of four at each cross-link, similar to experimental observations of average connectivity in acellular collagen gels from confocal microscopy [150]. In addition, Voronoi networks have been used successfully to predict network mechanics in collagen gels [80]. All Voronoi networks generated contained approximately 350 fibrils; each element was assigned a unique Voronoi network (with this same network for all 8 Gauss points within that element) randomly chosen from a set of 100 different networks. Hence, all 8 RVEs in each element have the same microstructure. Three simulations were made for the case of a network of fibers, which a different pool of 100 Voronoi networks used for each run. Values for materials constants A and B were 340nN and 2.5 respectively, obtained from previous experimental result for pure collagen gels [59]. For

the Neo-Hookean and network cases, simulations were run using a 128 processor cluster at the Minnesota Computing Institute, with wall times on the order of 12 hours.

6.2.2 Cell containing network of filaments

To include cell deformability, the filamentous structures on the cell were modeled using the same Voronoi networks as described above, with the same governing equation 3 for individual filaments. In addition, cells were assumed to be incompressible in the short term (e.g., during the duration of a tensile test). To impose incompressibility, a hydrostatic pressure term, *p*, was added to equation 1 to compute the Cauchy stress in the cell elements:

$$\langle \sigma_{ij}^{cell} \rangle = \frac{1}{V} \sum_{\substack{boundary \\ crosslinks}} x_i F_j - p\delta_{ij} \tag{6-10}$$

where *p* is the (uniform) pressure in the cell. This pressure, acting similarly to a Lagrange multiplier, represents the effect of the cytosol (i.e., intracellular fluid) on the cell, and was varied to allow the cell to maintain constant *total* volume. Individual elements within the cell were not required to maintain volume, representing the ability of water to move within the cell but not across the cell membrane at the time scale of interest. The relative stiffness between the cell and matrix regions was changed by altering the value of the material constant *A* in equation 3:

(a) A_{cell} = 340nN, A_{matrix} = 3400nN – matrix 10 times stiffer than the cell

(b) A_{cell} = 3400nN, A_{matrix} = 340nN – cell 10 times stiffer than the matrix

(c) A_{cell} = 340nN, A_{matrix} = 340nN – same stiffness for cell and matrix

Case (c) did not reduce to a simple box with fibrils of similar properties throughout because of the incompressibility of the cell region. Because of the computational cost of running these multiscale simulations, a coarser 10 vol% finite element mesh containing 608 elements was used; mesh refinement was checked against a finer mesh containing 1812 elements, which resulted in a mean difference of less than 3% in the stress-strain response for case (c). Similar to the rigid cell case with the ECM represented by a network of fibers, each element contained a unique Voronoi network randomly selected from a pool of 100 different networks; for each case, three simulations were run using a different pool for each run. To quantify the orientation of the networks, the network orientation tensor was calculated as

$$\Omega = \frac{1}{l_{total}} \sum l_i \begin{bmatrix} \cos^2 \alpha_i & \cos \alpha_i \cos \beta_i & \cos \alpha_i \cos \gamma_i \\ \cos \alpha_i \cos \beta_i & \cos^2 \beta_i & \cos \beta_i \cos \gamma_i \\ \cos \alpha_i \cos \gamma_i & \cos \beta_i \cos \gamma_i & \cos^2 \gamma_i \end{bmatrix} \qquad (6\text{-}11)$$

where l_{total} is the total length of all fibers in the network, l_i is the length of fiber i, and $\cos \alpha_i$, $\cos \beta_i$, and $\cos \gamma_i$ are the directional cosines of fiber i with respect to the 1, 2, and 3 axis directions respectively. For an isotropic network, $\Omega_{11} = \Omega_{22} = \Omega_{33} = 1/3$, and all off-diagonal components are 0.

6.2.3 Statistical Analysis

Statistical analyses were done using the commercial statistical package in Origin (OriginLab Corporation, Northampton, MA). Comparisons of material properties between two groups were performed using a two-tailed unpaired t-test. For multiple groups, a 1-way ANOVA F-test, coupled with multiple comparisons using the Bonferroni procedure, was used.
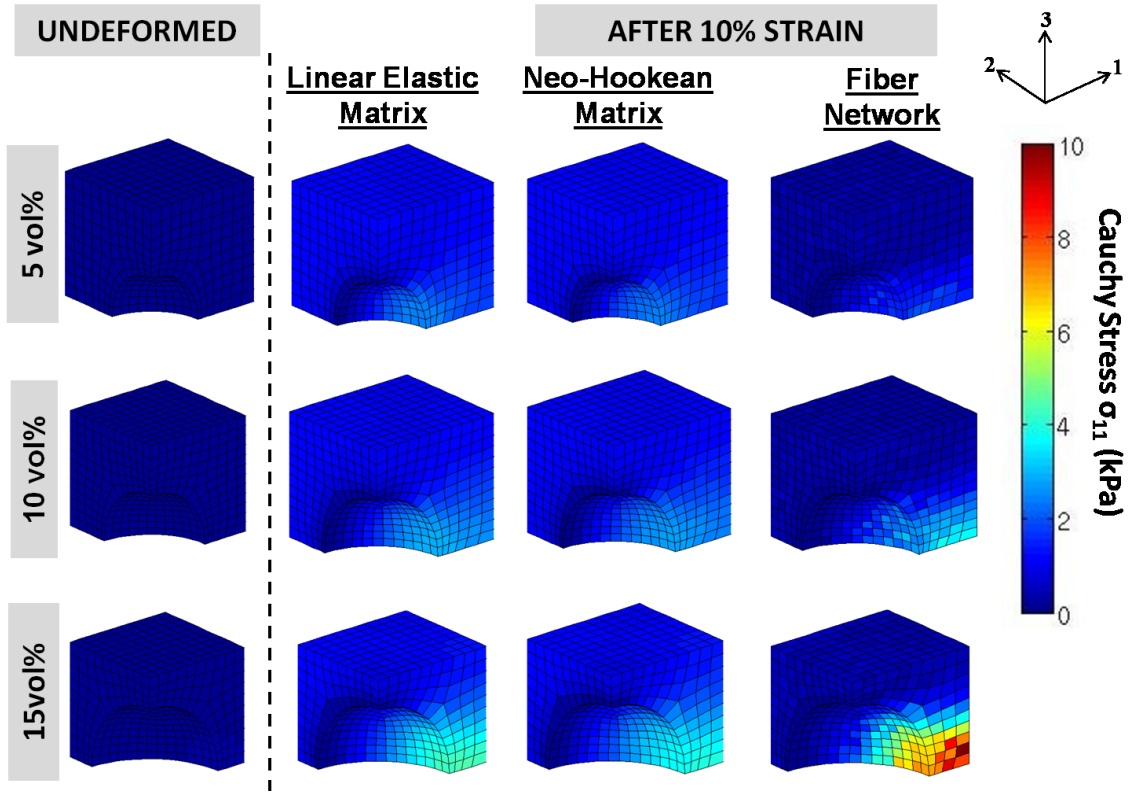
Figure 6-2. Undeformed meshes, as well as Cauchy stress (σ_{11}) distributions after 10% strain (averaged over 3 runs for each), for the cases of a linear elastic matrix, Neo-Hookean matrix, and a fiber network at rigid cell volume fractions of 5%, 10%, and 15%. The rigid cells were removed for clarity. In general, larger stresses were observed with increasing cell volume fraction. Variations in cell stresses in the fiber network cases were due to the uniqueness of Voronoi networks used for each element.

6.3. Results

6.3.1 Rigid Cell

Plots of the undeformed meshes, as well as Cauchy σ_{11} stress distributions after 10% stretch, are shown in Figure 6-2, with the rigid cell removed for clarity. As expected, higher stresses were observed with increasing cell volume in all matrix cases, as the proportion of the infinitely stiff cell component increased. Stress concentrated in the matrix at the leading edge of tension in front of the cell, where the effect of the rigid cell was most felt. The largest stresses around this leading edge were observed for the

network material cases; in the matrix-only regions above the cell, in contrast, the network material exhibited lower stresses than the linear elastic and Neo-Hookean matrix cases. These results demonstrate the highly non-linear mechanical behavior of the Voronoi networks compared to the Hookean and Neo-Hookean models: larger stresses in the matrix elements near the cell were contrasted with smaller stresses in the matrix-only region above the cell. It should be emphasized that this effect of large stress gradients within the composite arises from the degree of non-linearity in the network model, and not from the relative stiffness of the fiber network compared to the constitutive models. Since the Hookean and Neo-Hookean models have a linear dependence on G_m, changing G_m will alter the *magnitude* of the stresses developed in the composite; the stress *distributions,* however, within the composite will be unchanged. In comparison, the high degree of non-linearity in the network model will still produce larger differences in stresses within the composite (compared to the Hookean and Neo-Hookean models), with much higher stresses in the leading front of the cell contrasted with smaller stresses in the cell-free region above the cell. Similar stress gradients to our network model may be observed if constitutive models with higher degrees of non-linearity are used, e.g., the Ogden model. Similarly, it is expected that increasing the fiber stiffness parameter *A* (in equation 3) will increase the magnitude of the stresses developed, while increasing the degree of non-linearity (parameter *B*) will alter the stress gradients developed within the composite.

This non-linear stress-strain behavior of the network material, similar to the mechanical behavior of soft tissues [81,152], is also shown in Figure 6-3. In contrast, the
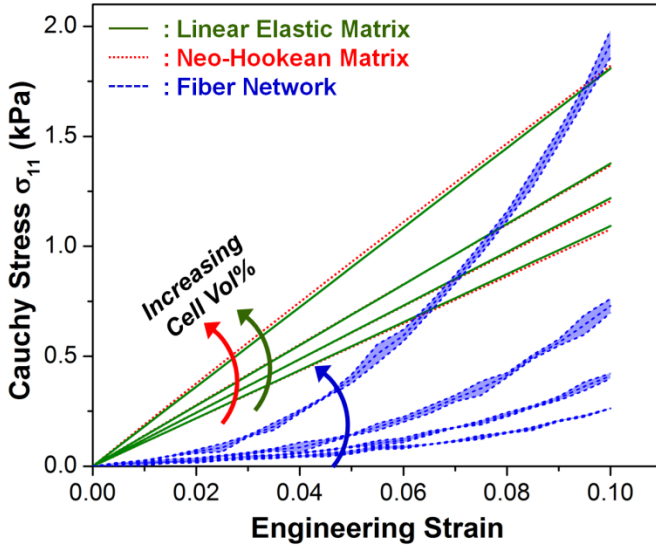
Figure 6-3. Cauchy stress σ_{11} vs engineering strain for the linear elastic matrix, Neo-Hookean matrix, and fiber network cases at rigid cell volume fractions of 0%, 5%, 10%, and 15%. Stress-strain curves for the linear elastic and Neo-Hookean matrix cases appeared linear and largely coincided with each other. The fiber network case exhibited non-linear stress-strain behavior, similar to that of soft tissues. Error bands in the fiber network cases are 95% confidence intervals, n = 3 for each case.

linear elastic and Neo-Hookean matrix cases showed relatively linear stress-strain characteristics that largely coincided with each other at all cell proportions. While lower stresses were observed in the network material composites for 0, 5 and 10% cell volume cases, rapidly increasing stress in the network material for the 15 vol% cell case resulted in the overall composite stress overtaking the linear elastic and Neo-Hookean matrix cases at 10% strain. Unlike the smooth stress distributions in the linear elastic and Neo-Hookean matrix cases, greater variations were observed in the network matrix cases, attributed to the different Voronoi networks used for each element: slight differences in network mechanical behavior exist within the set of unique networks even though all networks had approximately the same number of fibers.

Quantitative comparisons of composite elastic modulus (E*) and Poisson's ratio between the different models are shown in Figure 6-4. Comparison of these material

99
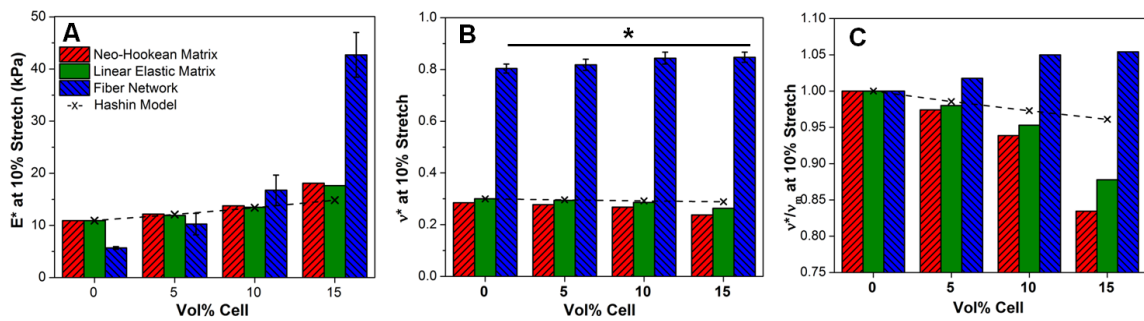
Figure 6-4. Plots at 10% stretch of (A) composite elastic modulus E*, (B) composite Poisson's ratio v*, and (C) composite Poisson's ratio normalized with Poisson's ratio of the matrix, v*/v$_m$, compared with the Hashin model. * represents statistical significance at the 95% level. Model results showed close agreement with the Hashin solution at lower volume fractions. Unlike the linear elastic and Neo-Hookean matrix cases, the Poisson's ratio for the fiber network case did not decrease with increasing cell volume fraction. Error bars for the fiber network cases are 95% confidence intervals, n = 3 for each case.

properties for the linear elastic matrix case with the Hashin model showed close agreement at low cell proportions, with larger deviations from the Hashin solution with increasing cell volume. Consistent with the qualitative observations of the stress-strain behavior in Figure 6-3, the network material exhibited a non-linear increase in composite stiffness with cell volume (Figure 6-4A), compared to more gradual increases for the linear elastic and Neo-Hookean matrix cases. These results were consistent with experimental data from our previous study which showed increasing stiffness in our cell-seeded collagen gel tissue equivalents with cell volume fraction [172]. Results for the composite Poisson's ratio, *v**, showed values for the network models that were larger than the elastic theory limit of 0.5 for incompressible materials (Figure 6-4B). This observation is consistent with our previous studies using these networks [104], and is a consequence of the looseness of the Voronoi network structure which allows the ECM to collapse significantly. That the composite Poisson's ratio, *v**, decreased with increasing cell proportion for the linear elastic and Neo-Hookean matrix cases (Figure 6-4C) was

100
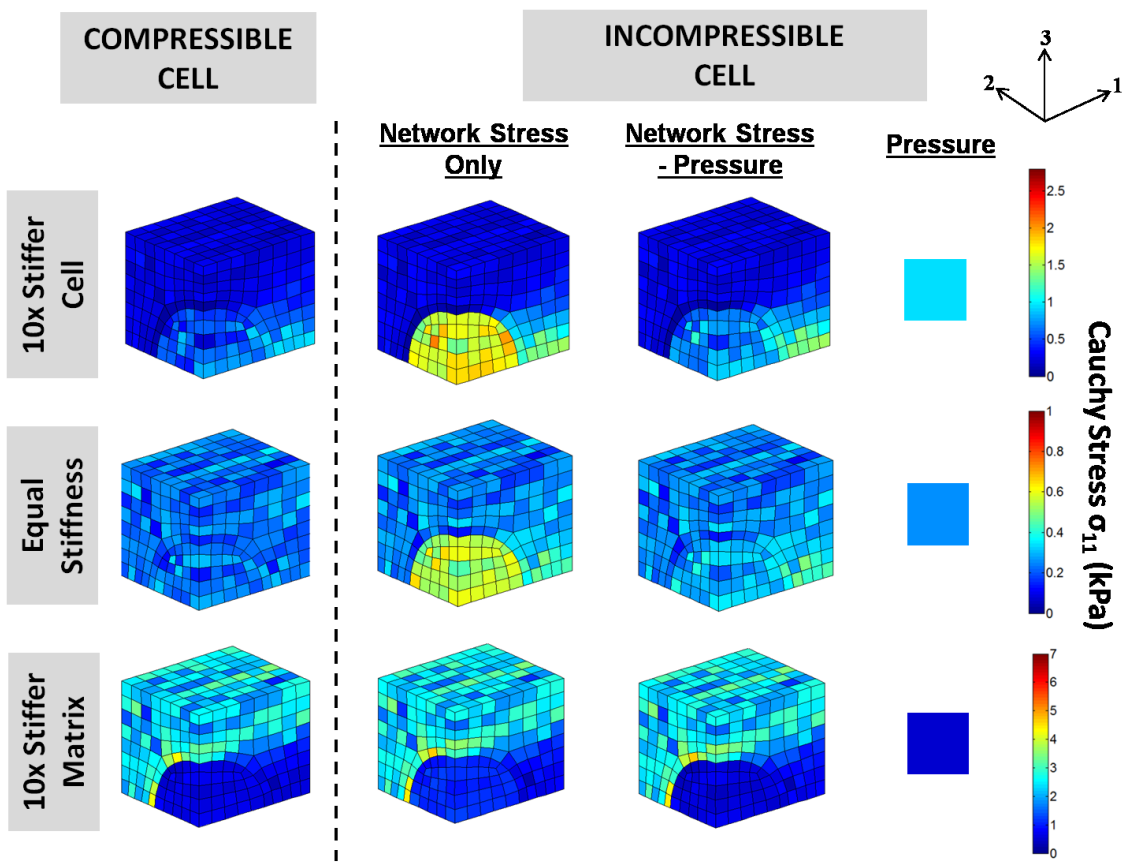
Figure 6-5. Cauchy stress (σ_{11}) distributions at 10% stretch of the 10x stiffer cell (1st row), equal cell and matrix stiffness (2nd row), and the 10x stiffer matrix (3rd row) cases, for both the compressible and incompressible cells (averaged over 3 runs for each case). Stress distributions around the cell differed depending on the relative stiffness of cell and matrix. In all cases, introduction of a cytoplasmic pressure to enforce incompressibility increased the stresses borne by the cell filament networks.

expected since the rigid cell resisted compaction. The network material case, however, did not exhibit the same decreasing trend in v^*; in fact, Figure 6-4C indicated higher Poisson's ratios for all cell proportions compared to the matrix-only (i.e. 0 vol%) case, although the difference was only statistically significant for the 15 vol% cell (p = 0.047).

6.3.2. Cell containing network of filaments

Figure 6-5 shows plots of the Cauchy stress distributions after 10% stretch for the compressible and incompressible cell cases, averaged over the three simulations for each

case, with varying relative stiffness for the cell and matrix components as described in Section 6.3.2. Here, a compressible cell is defined as the case without an intracellular pressure. The mottled appearance of stresses in these models can be attributed to variation among the 100 networks randomly sampled for each element. This phenomenon is especially noticeable in the compressible cell case with equal stiffness values for both the cell and matrix: even though the composite is effectively comprised of Voronoi networks prescribed with the same material properties, the mottled appearance is a consequence of slight differences in mechanical behavior between the networks used in each element. Altering the relative stiffness of the cell and matrix resulted in different stress distributions in the matrix around the cell. In the case of a stiffer cell (top row), higher resistance to the macroscopic stretch from the cellular filament network caused the matrix ahead of the cell in the stretch direction to bear a larger proportion of the overall deformation, hence producing higher matrix stresses around this region compared to the cell-free region above it. Conversely, in the stiffer matrix case (bottom row), the compliant cell bore a disproportionately larger amount of deformation compared to the matrix ahead of the cell, thereby relieving stress in the matrix compared to the cell-free region above.

In all cases, incorporation of hydrostatic pressure to enforce incompressibility increased the stresses borne by the filament networks in the cell, countered by similar qualitative increases in matrix stresses directly ahead of the cell in the stretch direction, as the matrix bore a larger proportion of the overall stretch. These higher stresses in the cell networks were the result of restricted rotation of the filaments about their cross-links
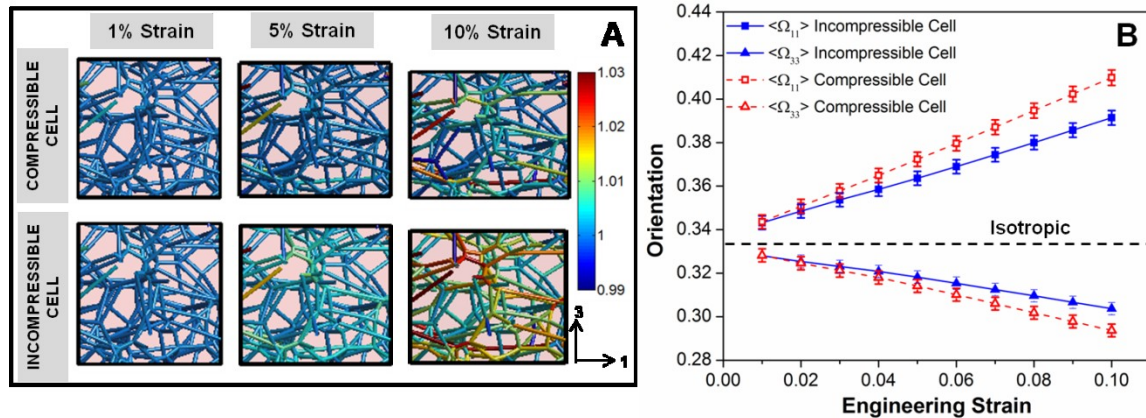
Figure 6-6. (A) Representative cell filament network at 1%, 5% and 10% strain for the compressible and incompressible cell cases, showing the distribution of filament stretches in the networks. Larger filament stretches were observed for the incompressible cell case. (B) Average filament orientation in the 1 (Ω_{11}) and 3 (Ω_{33}) directions vs. strain for the compressible and incompressible cell cases. Introduction of a cytoplasmic pressure inhibited filament rotation into the direction of stretch, such that the filaments were less oriented in the incompressible cell. Error bars are 95% confidence intervals, n = 112 (total number of cell elements).
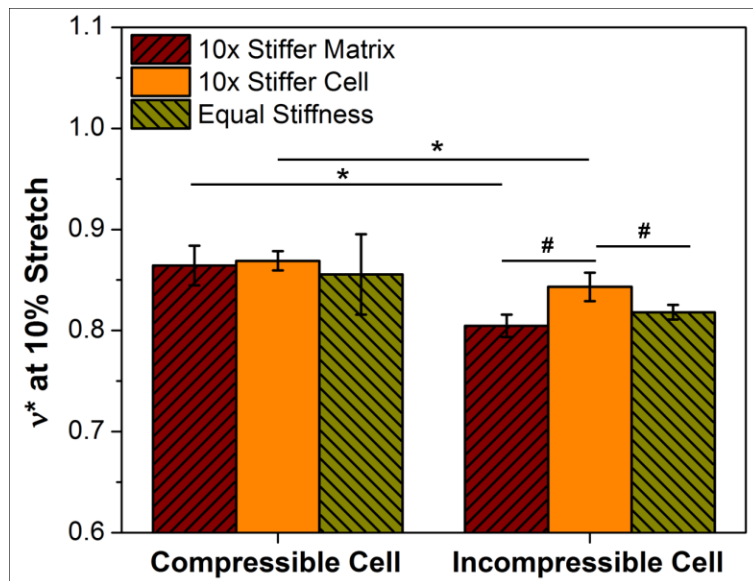
Figure 6-7. Composite Poisson's ratio, v*, at 10% stretch for the compressible and incompressible cell cases, with different relative stiffness of cell and matrix. * and # represent statistical significance at the 95% level. No significant differences were observed between the different relative stiffness cases for the compressible cell. The 10x stiffer cell case had significantly higher v* than the 10x stiffer matrix (p = 0.0036) and equal stiffness (p = 0.0285) cases for the incompressible cell. Error bars represent 95% confidence intervals, with n = 3 for each case.
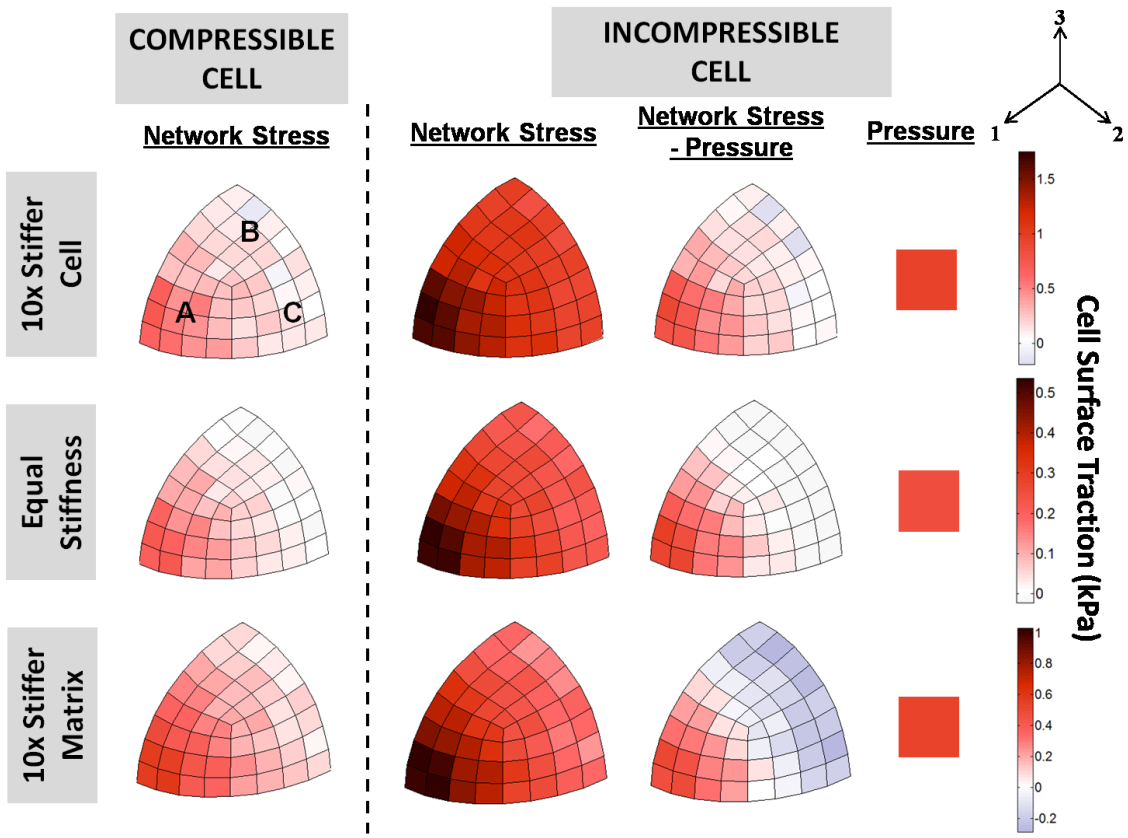
Figure 6-8. Cell surface traction at 10% stretch of the 10x stiffer cell (1st row), equal cell and matrix stiffness (2nd row), and the 10x stiffer matrix (3rd row) cases, for both the compressible and incompressible cells (averaged over 3 runs for each case). In the compressible cell cases, large tensile stresses were observed in the direction of tension (region A). The cell surface region under the Poisson effect (regions B and C) did not exhibit large compressive stresses. Addition of pressure increased the surface traction from the cell filament network, and slightly increased the overall compressive stress in regions B and C.

into the direction of stretch due to the outward pressure exerted against the cell membrane, shown qualitatively by the selected RVE plots of fiber stretches in Figure 6-6A, and quantified by the lower $<\Omega_{11}>$ values for the incompressible cell case in Figure 6-6B. The added resistance to cell deformation by the pressure consequently decreased the overall Poisson's ratio of the composite in all cases (Figure 6-7), but this difference was not significant at the 95% level for the equal stiffness case. Similar to the rigid cell cases, no significant differences in v^* were observed across all cases of the compressible

cell; for the incompressible cell, the Poisson's ratio for the 10x stiffer cell was significantly higher than that of the 10x stiffer matrix (p = 0.0036), and equal cell and matrix stiffness cases (p = 0.0285).

The traction on the cell surface (averaged over 3 runs) was plotted for both the compressible and incompressible cell in Figure 6-8. The magnitude of the traction stress from the cell filament network was computed by $n_i n_j \sigma_{ij}$, where n_i and n_j both are the unit normal to each cell surface element, and σ_{ij} is the averaged Cauchy stress tensor of the cell element. Similar traction stress distributions were observed for all compressible cell cases: the cell networks developed large tensile stresses in region facing the 1-direction (i.e., direction of macroscopic stretch – exemplified by region A in the 10x stiffer compressible cell), contrasted with smaller stresses in the regions facing the transverse directions (i.e. regions under the Poisson effect – regions B and C). Since the transverse surfaces were stress-free, the cell regions B and C were expected to be stress-free regardless of the relative stiffness between the cell and the matrix, as confirmed by model simulations using a Neo-Hookean formulation for both cell and matrix (data not shown). In the 10x stiffer cell and 10x stiffer matrix cases, however, these regions exhibited non-zero tensile stresses. This result is likely a consequence of the asymmetric mechanical behavior of these networks, which are strong in tension but very weak in compression, hence producing a net positive traction even in these transverse regions. Introduction of the cytoplasmic pressure to render the cell incompressible had the effect of increasing the tensile stresses in the networks throughout the cell. While the overall stress state of the cell ("Network Stress - Pressure" plots in Figure 6-8) showed similar stress distributions
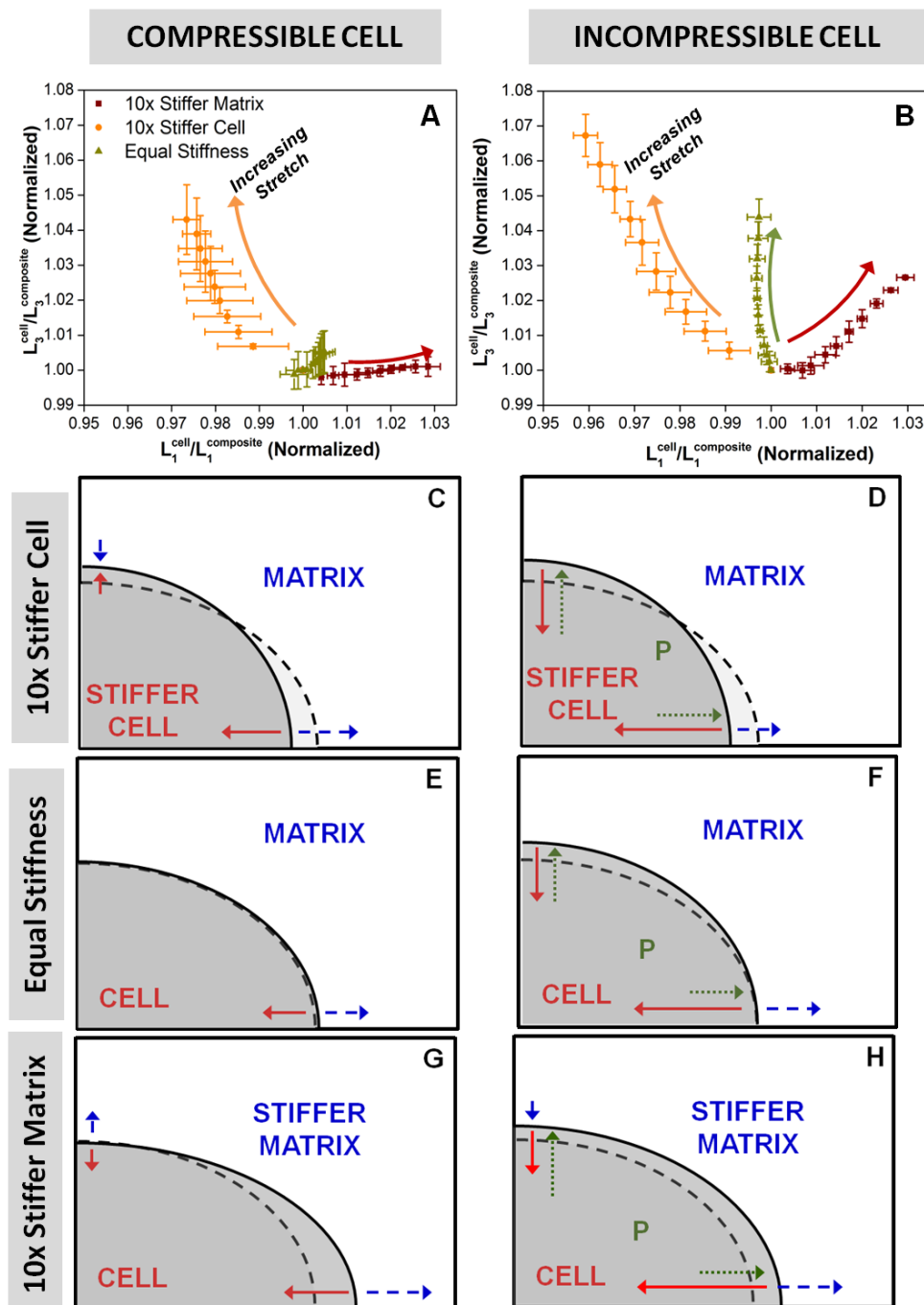
Figure 6-9. (A-B): Normalized ratio of cell dimension to composite dimension in the 3-direction vs. the 1-direction. Addition of pressure increased the cell proportion in the 3-direction for all cases. (C-H): Schematic drawings showing differences in cell shape, and the stresses exerted on the cell surface at equilibrium; dotted lines represent the equal cell and matrix stiffness case without pressure. In the compressible cell cases (C, E, G), matrix tension in the 1-direction was always balanced by cell tension. In the incompressible cell cases, (D, F, H), the outward-exerting pressure pushed out against the cell to increase cell proportion in the 3-direction.

106

to those in the compressible cell cases, addition of pressure had the effect of increasing the magnitudes of both the tensile and compressive stresses on the cell, with regions B and C now more evidently under compression, especially in the 10x stiffer matrix case.

Figures 6-9A and 6-9B show dimensional changes for the cell in the 1 and 3 directions for the compressible and incompressible cell cases, respectively, with schematic drawings underneath (Figures 6-9C – 6-9H) illustrating the differences in cell shape after deformation, as well as the stresses exerted on the cell surface at static equilibrium. The normalized ratio of cell dimension to overall composite (cell + fiber matrix) dimension on either axis is a measure of the relative deformation of the cell compared to that of the overall composite. On the abscissa, a value greater than 1 means the cell stretch is greater than that of the composite in the 1-direction. Conversely, on the ordinate axis, a value greater than 1 indicates that the cell contracts less in the 3-direction than the matrix. For the compressible cell cases, the equal stiffness case exhibited little change in cell proportion in both directions under stretch, a result that was as expected. The 10x stiffer matrix case showed an increase in cell proportion in the 1-direction, but it did not predict a similar increase in cell deformation in the compressive 3-direction, a result that reinforced the idea that these networks, while strong in tension, had little compressive strength. While the 10x stiffer cell showed expected higher resistance to deformation in both directions, the above result strongly suggested that the increased resistance to compression was not due to a direct increase in cell compressive stiffness, but a consequence of lesser rotation into the direction of stretch due to increased *tensile* stiffness, which prevented compaction of the cell by inhibiting the collapse of the cell's

filament network. In the compressible cell cases (Figures 6-9C, E, G), matrix tension in the 1-direction was always balanced by cell tension. For the stiff cell (Figure 6-9C), the matrix pushed in on the cell, whereas for the stiff matrix, σ_{22} was positive for the cell, indicating that the cell was being pulled out by the matrix. Enforcing cell incompressibility (Figures 6-9D, F, H) had the effect of increasing the stresses of the filamentous networks in all cases; this increase in filamentous stress was countered by the cytoplasmic pressure pushing outward against the cell surface, such that the net effect was an increase in cell dimension in the 3-direction in all cases. In the 1-direction, this pressure exerted stress on the cell surface in the same direction as the matrix in tension, but did not cause the cell to elongate in this direction in all cases; in fact, cell dimension decreased for both the 10x stiffer cell and 10x stiffer matrix cases (albeit only a slight decrease in the latter). This observation could be explained by the fact that the intracellular pressure preserves volume by resisting changes to the overall cell shape. Hence, the net effect of this pressure is that the cell bears a smaller proportion of the overall deformation in both the tensile and compressive directions (compared to the case without pressure), as shown from comparison of Figures 6-9A and 6-9B. As a result, the filamentous network develops larger tensile stresses (due to restricted rotation into the direction of stretch, shown in Figure 6-6) that counters the effect of intracellular pressure working in tandem with the ECM tension.

6.4 Discussion

This study represented a major improvement to our multiscale model to understand soft tissue biomechanics by incorporating a major component of such tissues:

cells. We acknowledge, however, that several critical assumptions were used in the model development. First, the cell-matrix interface was modeled as continuous even though cells are known to attach to the matrix via discrete focal adhesions [178,179]; Guilak and Mow [159] asserted that such an assumption was not unreasonable based on experimental evidence of numerous focal adhesion points for chondrocyte attachment to its pericellular matrix from confocal and electron microscopy [180,181]. In addition, the microstructural representations of both the ECM and cell were simplified to contain only a network. In reality, the ECM is generally comprised of other biomacromolecules (e.g. proteoglycans) which exist within the network interstitium, and which alter the overall mechanics of the tissue. For the cell, this reduced representation comprised entirely of a network of cytoskeletal filaments was chosen based on studies showing that the cytoskeleton was predominantly responsible for structural integrity and stiffness in a cell [182], and hence is a reasonable first approximation for modeling the passive mechanical contribution of cells. The current model also accounts for equilibrium mechanical properties only, ignoring the viscoelastic behavior of both the cell and ECM. Nevertheless, development of this model helped gain significant insight into the cellular mechanical microenvironment, and laid the groundwork for future work incorporating further microstructural and mechanical details for the cell and ECM.

Comparison of the inclusion-based model of Hashin with our finite element model results showed close agreement at low cell volume fractions; deviation at higher cell concentrations were expected since the Hashin model is only relevant at low inclusion densities. While our previous work on cell-seeded collagen gels showed close

agreement of Young's modulus predicted by the Hashin model with experimental data at low cell volume fractions [172], such models are unable to generate the highly non-linear stress-strain behavior of soft tissues. In addition, elastic theories preclude Poisson's ratios larger than 0.5, while many tissues have been shown to exhibit Poisson's ratios with values much higher than this elastic limit in tension. The ability of our multiscale network simulations to generate non-linear stress-strain behavior (as shown in Figure 6-3) and Poisson's ratios beyond the elastic limit demonstrates a more viable and accurate model for application towards soft tissue biomechanics.

The multiscale model predicted similar composite Poisson's ratios regardless of the volume fraction of rigid cell. This unexpected result suggests that the composite Poisson's ratio is dependent only on the collapse of the network in the matrix above the cell, caused by fiber rotation about their cross-links. Across all volume fractions of rigid cell, the matrix-only region (above the cell) experiences the same amount stretch, hence the same degree of network collapse, to produce similar Poisson's ratios.

The model assumption that cells are incompressible is reasonable, validated by experimental data on single chondrocytes where an apparent Poisson's ratio of 0.49 was reported, although this value was shown to decrease with increasing axial strain [183]. Modeling the cell as compressible and incompressible, however, generally represents two extreme cases of the effect of the intracellular fluid; in reality, a cell is likely to be "moderately" compressible and dependent on the time scale of observation. In such cases, we hypothesize that our results would lie between our extreme cases of the compressible and incompressible cells. The resistance to filament rotation into the direction of stretch

due to the pressure (Figure 6-6) would cause the network to stretch to an intermediate extent, thereby producing stresses bounded by the current results. Similarly, the intracellular pressure would resist cell compression, though to a smaller extent than the incompressible cell case shown in Figure 6-9B.

In a tissue under tension, the tensile stress on the cell by the fibrillar matrix has the effect of elongating the cell into the direction of stretch; such changes in cell shape and alignment are similar to experimental observations of contact guidance of cells, where cells preferentially elongate with the underlying matrix fibrils aligned under stretch [184,185].

Model results from this study show complex effects of relative cell and matrix stiffness, as well as cytoplasmic pressure, on the overall cellular mechanical microenvironment, which has implications on understanding cellular mechanosensation. That cells respond differently to varying substrate stiffness has been extensively studied, in terms of various cell properties and processes such as cell attachment [186] and morphology [187], proliferation [188], stem cell differentiation [189], and migration [190]. The justification for modeling the three different scenarios for the relative stiffness between the cell and the matrix was based on experimental results on different cell types showing a wide range of cell stiffness, e.g., from ~0.2kPa in fibroblasts, to 42kPa in cardiac myocytes [182]. From our previous studies, the elastic (tangent) modulus of 2mg/mL acellular collagen gels was found to be on the order of 10kPa [59]; compacted gels would exhibit significantly higher modulus. Hence, our three scenarios were designed to qualitatively cover a wide combination of cell types entrapped in different

ECM. The current work shows that the stiffness of the matrix relative to that of the cell can also affect the qualitative and quantitative nature of strain transfer from the tissue to the cell. Even in the compressible cell case, the net transverse stress acting on a cell can be tensile or compressive depending on the relative stiffness of the cell and matrix. When the cell is incompressible, the existence of the cytoplasmic pressure can cause significant filamentous tension even in the transverse directions, which might be expected to be in compression or nearly stress-free. To the best of our knowledge, there are no published experimental data on detailed stress and/or strain fields of cells entrapped in a matrix under tension, for comparison with our model predictions. Recently developed techniques, however, have the potential of quantifying cell/matrix stresses and strains in tissues under tension, e.g., measurement of three-dimensional traction forces exerted by cells entrapped in a hydrogel [191], and generation of three-dimensional strain maps of cells with their surrounding matrix [192]. The combination of these experimental techniques with computational modeling can provide a clearer picture of the cellular mechanical microenvironment in tissues. Such findings can have implications on improving tissue engineering design, in terms of providing the optimal level of mechanical signaling to promote desired growth and remodeling by the cells.

7. Conclusions and Future Work

This thesis work presented various improvements to an existing computational model of a single network (representing the fibrillar extra-cellular matrix) to predict the mechanical behavior of bioengineered soft tissues. Incorporation of other components that comprise a soft tissue – a secondary network (Chapters 2 and 3), an interstitial matrix (Chapters 3 and 4), and cells (Chapter 5), enhanced our understanding of the microstructural origins of the overall mechanics in soft tissues. Through this work, we have shown that composite theories such as the simple rule of mixtures and the Hashin model are inadequate in describing the overall mechanics of tissues, hence necessitating the use of more complex modeling approaches. The use of a microstructural approach in our modeling efforts has the advantage of incorporating details from microstructure into our simulations, e.g., fiber network anisotropy, cellular stress fiber networks, interaction between components – features that could not be represented to the same level of detail using phenomenological or continuum approaches.

One of the key goals for a bioengineered tissue is to develop mechanical properties that are comparable to that of its native counterparts. To this end, cells play a critical role in imparting mechanical strength via means such as tissue compaction and matrix production. While the overall mechanical behavior of a bioengineered tissue can be measured easily, interactions on a microstructural level between the different

components in soft tissues, which have a profound effect on the mechanical microenvironment, are difficult to quantify and observe experimentally. In this thesis work, we have shown that our model provides a method to investigate computationally such interactions, and the stress inhomogeneities within the cells' mechanical microenvironment that arise as a result. Hence, such simulations have the potential to provide a better fundamental understanding of the relationship between tissue microstructure and overall mechanics, to develop more rational designs and approaches used in tissue engineering.

The future on this project will involve further improvements to the computational model to address current shortcomings:

(A) Incorporation of viscoelastic behavior. Soft tissues are known to exhibit viscoelastic behavior [121,125,193–195]; the current model considers only the long-time, quasi-static equilibrium mechanical behavior of tissues. Incorporation of viscoelasticity will be a major improvement to our model, and allows us to investigate the time-dependence in the mechanical response of soft tissues. We will modify the constitutive equations governing the different microstructural components to account for the viscoelastic effects from each component.

(B) Modeling the effects of pre-stress on a collagen network within a tissue. This proposed work will be a continuation of the study using Col-HA TEs in Chapter 5. The experimental data obtained from the HA-Col experiments will be used to guide the development of our model to introduce a pre-stress in our networks. In addition, we will study the effects of different extents of pre-stress on the collagen network on overall

mechanical behavior of the TEs, and compare experimental results with our model predictions.

(C) Inclusion of microstructural detail within a cell. The first attempt at modeling the mechanical contribution of cells only involves simulation of an isotropic actin network which is homoegeneously distributed throughout the cell, as well as a cytosolic pressure (Chapter 6). Improvements to the cell representation include will incorporation of a cell nucleus, and alignment and distribution of the actin network to represent the actin cortex. We will also explore ways to alter the cell shape in our model to that which is more representative of real cells, e.g., using confocal microscopy to obtain a three-dimensional cell geometry.

(D) Modeling the active mechanical contributions from cells. Our current model formulation assumes cells as passive, dilute and non-interacting. We will explore ways to simulate higher cell densities to include cell-cell interactions, as well as cell remodeling behavior such as fiber network alignment from tissue compaction.

Bibliography

[1]   Viola J., Lal B., and Grad O., 2003, "The Emergence of Tissue Engineering as a Research Field."

[2]   Butler D. L., Goldstein S. A., and Guilak F., 2000, "Functional Tissue Engineering: The Role of Biomechanics," J. Biomech. Eng., **122**(6), pp. 570–575.

[3]   Vesely I., and Boughner D., 1989, "Analysis of the Bending Behaviour of Porcine Xenograft Leaflets and of Natural Aortic Valve Material: Bending Stiffness, Neutral Axis and Shear Measurements," J. Biomech., **22**(6-7), pp. 655–671.

[4]   Billiar K. L., and Sacks M. S., 2000, "Biaxial Mechanical Properties of the Native and Glutaraldehyde-Treated Aortic Valve Cusp: Part II---A Structural Constitutive Model," J. Biomech. Eng., **122**(4), pp. 327–335.

[5]   Ma Z., Gao C., Gong Y., and Shen J., 2005, "Cartilage Tissue Engineering PLLA Scaffold with Surface Immobilized Collagen and Basic Fibroblast Growth Factor," Biomaterials, **26**(11), pp. 1253–1259.

[6]   Grassl E. D., Oegema T. R., and Tranquillo R. T., 2003, "A Fibrin-Based Arterial Media Equivalent," J. Biomed. Mater. Res. A, **66A**(3), pp. 550–561.

[7]   Rowe S. L., Lee S. Y., and Stegemann J. P., 2007, "Influence of Thrombin Concentration on the Mechanical and Morphological Properties of Cell-Seeded Fibrin Hydrogels," Acta Biomater., **3**(1), pp. 59–67.

[8]   Cummings C. L., Gawlitta D., Nerem R. M., and Stegemann J. P., 2004, "Properties of Engineered Vascular Constructs Made From Collagen, Fibrin, and Collagen–Fibrin Mixtures," Biomaterials, **25**(17), pp. 3699–3706.

[9]   Hoerstrup S. P., Zünd G., Sodian R., Schnell A. M., Grünenfelder J., and Turina M. I., 2001, "Tissue engineering of Small Caliber Vascular Grafts," Eur. J. Cardio-Thorac., **20**(1), pp. 164–169.

[10]   Mauck R. L., Nicoll S. B., Seyhan S. L., Ateshian G. A., and Hung C. T., 2003, "Synergistic Action of Growth Factors and Dynamic Loading for Articular Cartilage Tissue Engineering," Tissue Eng., **9**(4), pp. 597–611.

[11]   Lanir Y., 1983, "Constitutive Equations for Fibrous Connective Tissues," J. Biomech., **16**(1), pp. 1–12.

[12]   Zahalak G. I., Wagenseil J. E., Wakatsuki T., and Elson E. L., 2000, "A Cell-Based Constitutive Relation for Bio-Artificial Tissues," Biophys. J., **79**(5), pp. 2369–2381.

[13]   Marquez J. P., Genin G. M., Zahalak G. I., and Elson E. L., 2005, "Thin Bio-Artificial Tissues in Plane Stress: The Relationship between Cell and Tissue Strain, and an Improved Constitutive Model," Biophys. J., **88**(2), pp. 765–777.

[14]   Sander E. A., Stylianopoulos T., Tranquillo R. T., and Barocas V. H., 2009, "Image-Based Multiscale Modeling Predicts Tissue-Level and Network-Level Fiber Reorganization in Stretched Cell-Compacted Collagen Gels," Proc. Natl. Acad. Sci., **106**(42), pp. 17675–17680.

[15]   Hashin Z., 1962, "The Elastic Moduli of Heterogeneous Material," J. Appl. Mech., pp. 143–150.

[16] Lee C. H., Singla A., and Lee Y., 2001, "Biomedical Applications of Collagen," Int. J. Pharm., **221**(1-2), pp. 1–22.

[17] Buttafoco L., Kolkman N. G., Engbers-Buijtenhuijs P., Poot A. A., Dijkstra P. J., Vermes I., and Feijen J., 2006, "Electrospinning of Collagen and Elastin for Tissue Engineering Applications," Biomaterials, **27**(5), pp. 724–734.

[18] Couet F., Rajan N., and Mantovani D., 2007, "Macromolecular Biomaterials for Scaffold-Based Vascular Tissue Engineering," Macromol. Biosci., **7**(5), pp. 701–718.

[19] Mol A., van Lieshout M. I., Dam-de Veen C. G., Neuenschwander S., Hoerstrup S. P., Baaijens F. P. T., and Bouten C. V. C., 2005, "Fibrin as a Cell Carrier in Cardiovascular Tissue Engineering Applications," Biomaterials, **26**(16), pp. 3113–3121.

[20] Grassl E. D., Oegema T. R., and Tranquillo R. T., 2002, "Fibrin as an Alternative Biopolymer to Type-I Collagen for the Fabrication of a Media Equivalent," J. Biomed. Mater. Res., **60**(4), pp. 607–612.

[21] Mosesson M. W., 2004, "John Ferry and the Mechanical Properties of Cross-Linked Fibrin," Biophys. Chem., **112**(2-3), pp. 215–218.

[22] Roska F. J., and Ferry J. D., 1982, "Studies of Fibrin Film. I. Stress Relaxation and Birefringence," Biopolymers, **21**(9), pp. 1811–1832.

[23] Roska F. J., Ferry J. D., Lin J. S., and Anderegg J. W., 1982, "Studies of Fibrin Film. II. Small- Angle X- ray Scattering," Biopolymers, **21**(9), pp. 1833–1845.

[24] Whittaker P., and Przyklenk K., 2009, "Fibrin Architecture in Clots: A Quantitative Polarized Light Microscopy Analysis," Blood Cells Mol. Dis, **42**(1), pp. 51–56.

[25] Miller E. J., 1984, "Chemistry of the Collagens and Their Distribution," Extracellular matrix biochemistry, pp. 41–81.

[26] Christiansen D. L., Huang E. K., and Silver F. H., 2000, "Assembly of Type I Collagen: Fusion of Fibril Subunits and the Influence of Fibril Diameter on Mechanical Properties," Matrix Biol., **19**(5), pp. 409–420.

[27] Eyre D. R., Paz M. A., and Gallop P. M., 1984, "Cross-Linking in Collagen and Elastin," Annu. Rev. Biochem., **53**(1), pp. 717–748.

[28] Eppell S. ., Smith B. ., Kahn H., and Ballarini R., 2006, "Nano Measurements with Micro-Devices: Mechanical Properties of Hydrated Collagen Fibrils," J. R. Soc. Interface, **3**(6), pp. 117–121.

[29] Wagenseil J. E., Wakatsuki T., Okamoto R. J., Zahalak G. I., and Elson E. L., 2003, "One-Dimensional Viscoelastic Behavior of Fibroblast Populated Collagen Matrices," J. Biomech. Eng., **125**(5), pp. 719–725.

[30] Rowe S. L., and Stegemann J. P., 2006, "Interpenetrating Collagen-Fibrin Composite Matrices with Varying Protein Contents and Ratios," Biomacromolecules, **7**(11), pp. 2942–2948.

[31] Rowe S. L., and Stegemann J. P., 2009, "Microstructure and Mechanics of Collagen-Fibrin Matrices Polymerized Using Ancrod Snake Venom Enzyme," J. Biomech. Eng., **131**(6), p. 061012.

[32] Duckert F., and Nyman D., 1978, "Factor XIII, Fibrin and Collagen," Suppl. Thromb. Haemost., **63**, pp. 391–396.

[33] Mosher D. F., and Schad P. E., 1979, "Cross-Linking of Fibronectin to Collagen by Blood Coagulation Factor XIIIa," J. Clin. Invest., **64**(3), pp. 781–787.

[34] Stemberger A., Jilek F., Hormann H., and Blumel G., 1977, "Fibrinogen-Collagen Interactions," Thromb. Haemost., **38**, p. 305.

[35] Stegemann H., and Stalder K., 1967, "Determination of Hydroxyproline," Clin. Chim. Acta, **18**(2), pp. 267–273.

[36] Ahmann K. A., Weinbaum J. S., Johnson S. L., and Tranquillo R. T., 2010, "Fibrin Degradation Enhances Vascular Smooth Muscle Cell Proliferation and Matrix Deposition in Fibrin-Based Tissue Constructs Fabricated *in Vitro*," Tissue Engineering Part A, **16**(10), pp. 3261–3270.

[37] Lake S. P., and Barocas V. H., 2011, "Mechanical and Structural Contribution of Non-Fibrillar Matrix in Uniaxial Tension: A Collagen-Agarose Co-Gel Model," Ann. Biomed. Eng., **39**(7), pp. 1891–1903.

[38] Chandran P. L., and Barocas V. H., 2007, "Deterministic Material-Based Averaging Theory Model of Collagen Gel Micromechanics," J. Biomech. Eng., **129**(2), pp. 137–147.

[39] Stylianopoulos T., and Barocas V. H., 2007, "Volume-Averaging Theory for the Study of the Mechanics of Collagen Networks," Comput. Meth. Appl. Mech. Eng., **196**(31-32), pp. 2981–2990.

[40] Fung Y., 1993, Biomechanics: Mechanical Properties of Living Tissues, Springer.

[41] Guthold M., Liu W., Sparks E. A., Jawerth L. M., Peng L., Falvo M., Superfine R., Hantgan R. R., and Lord S. T., 2007, "A Comparison of the Mechanical and Structural Properties of Fibrin Fibers with Other Protein Fibers," Cell Biochem. Biophys., **49**(3), pp. 165–181.

[42] Liu W., Jawerth L. M., Sparks E. A., Falvo M. R., Hantgan R. R., Superfine R., Lord S. T., and Guthold M., 2006, "Fibrin Fibers Have Extraordinary Extensibility and Elasticity," Science, **313**(5787), p. 634.

[43] Tower T. T., Neidert M. R., and Tranquillo R. T., 2002, "Fiber Alignment Imaging During Mechanical Testing of Soft Tissues," Ann. Biomed. Eng., **30**(10), pp. 1221–1233.

[44] Stuart K., and Panitch A., 2008, "Influence of Chondroitin Sulfate on Collagen gel Structure and Mechanical Properties at Physiologically Relevant Levels," Biopolymers, **89**(10), pp. 841–851.

[45] Lewis J. L., Johnson S. L., and Oegema T. R., 2002, "Interfibrillar Collagen Bonding Exists in Matrix Produced by Chondrocytes in Culture: Evidence by Electron Microscopy," Tissue Eng., **8**, pp. 989–995.

[46] Syedain Z. H., Weinberg J. S., and Tranquillo R. T., 2008, "Cyclic Distension of Fibrin-Based Tissue Constructs: Evidence of Adaptation During Growth of Engineered Connective Tissue," Proc. Natl. Acad. Sci., **105**(18), pp. 6537–6542.

[47] Alford P. W., Humphrey J. D., and Taber L. A., 2007, "Growth and Remodeling in a Thick-Walled Artery Model: Effects of Spatial Variations in Wall Constituents," Biomech. Model. Mechan., **7**, pp. 245–262.

[48]   Stylianopoulos T., and Barocas V. H., 2007, "Multiscale, Structure-Based Modeling for the Elastic Mechanical Behavior of Arterial Walls," J. Biomech. Eng., **129**(4), pp. 611–618.

[49]   Prockop J. D., 1995, "Collagens: Molecular Biology, Diseases, and Potentials for Therapy," Annu. Rev. Biochem., **64**(1), pp. 403–434.

[50]   Ross J. ., and Tranquillo R. ., 2003, "ECM Gene Expression Correlates With in Vitro Tissue Growth and Development in Fibrin gel Remodeled by Neonatal Smooth Muscle Cells," Matrix Biol., **22**(6), pp. 477–490.

[51]   Robinson P. S., Johnson S. L., Evans M. C., Barocas V. H., and Tranquillo R. T., 2008, "Functional Tissue-Engineered Valves from Cell-Remodeled Fibrin with Commissural Alignment of Cell-Produced Collagen," Tissue Eng. Pt. A, **14**(1), pp. 83–95.

[52]   Diamant J., Keller A., Baer E., Litt M., and Arridge R. G. C., 1972, "Collagen; Ultrastructure and its Relation to Mechanical Properties as a Function of Ageing," Proc. R. Soc. Lond. [Biol], **180**(1060), pp. 293 –315.

[53]   Mosesson M. W., 2005, "Fibrinogen and Fibrin Structure and Functions," J. Thromb. Haemost., **3**(8), pp. 1894–1904.

[54]   Pezzin G., Scandola M., and Gotte L., 1976, "The low Temperature Mechanical Relaxation of Elastin. I. The dry Protein," Biopolymers, **15**(2), pp. 283–292.

[55]   Scandola M., and Pezzin G., 1978, "The low Temperature Mechanical Relaxation of Elastin. II. The Solvated Protein," Biopolymers, **17**(1), pp. 213–223.

[56]   Yonese M., Baba K., and Kishimoto H., 1992, "Viscoelastic Properties of Poly(Vinyl Alcohol)/Alginate Snake-Cage Hydrogels and Interpenetrating Hydrogels," Polym. J., **24**(4), pp. 395–404.

[57]   Mathew A. P., Packirisamy S., and Thomas S., 2000, "Morphology, Mechanical Properties, and Failure Topography of Semi-Interpenetrating Polymer Networks Based on Natural Rubber and Polystyrene," J. Appl. Polym. Sci., **78**(13), pp. 2327–2344.

[58]   Santin M., Huang S. J., Iannace S., Ambrosio L., Nicolais L., and Peluso G., 1996, "Synthesis and Characterization of a new Interpenetrated Poly(2-Hydroxyethylmethacrylate)-Gelatin Composite Polymer," Biomaterials, **17**(15), pp. 1459–1467.

[59]   Lai V. K., Lake S. P., Frey C. R., Tranquillo R. T., and Barocas V. H., 2012, "Mechanical Behavior of Collagen-Fibrin Co-Gels Reflects Transition From Series to Parallel Interactions With Increasing Collagen Content," J. Biomech. Eng., **134**(1), p. 011004.

[60]   Ferry J. D., and Morrison P. R., 1947, "Preparation and Properties of Serum and Plasma Proteins. VIII. The Conversion of Human Fibrinogen to Fibrin under Various Conditions," J. Am. Chem. Soc., **69**(2), pp. 388–400.

[61]   Blombäck B., Carlsson K., Fatah K., Hessel B., and Procyk R., 1994, "Fibrin in Human Plasma: Gel Architectures Governed by Rate and Nature of Fibrinogen Activation," Thromb. Res., **75**(5), pp. 521–538.

[62]   Blombäck B., Carlsson K., Hessel B., Liljeborg A., Procyk R., and Åslund N., 1989, "Native Fibrin gel Networks Observed by 3D Microscopy, Permeation and

Turbidity," Biochim. Biophys. Acta, Protein Struct. Mol. Enzymol., **997**(1-2), pp. 96–110.

[63]   Akpalo E., and Larreta-Garde V., 2010, "Increase of Fibrin gel Elasticity by Enzymes: A Kinetic Approach," Acta Biomater., **6**(2), pp. 396–402.

[64]   Shen L. L., McDonagh R. P., McDonagh J., and Hermans Jr. J., 1974, "Fibrin gel Structure: Influence of Calcium and Covalent Cross-Linking on the Elasticity," Biochem. Biophys. Res. Commun., **56**(3), pp. 793–798.

[65]   Kaibara M., and Fukada E., 1977, "Effect of Temperature on Dynamic Viscoelasticity During the Clotting Reaction of Fibrin," Biochim. Biophys. Acta, Gen. Subj., **499**(3), pp. 352–361.

[66]   Dubey N., Letourneau P. C., and Tranquillo R. T., 2001, "Neuronal Contact Guidance in Magnetically Aligned Fibrin Gels: Effect of Variation in gel Mechano-Structural Properties," Biomaterials, **22**(10), pp. 1065–1075.

[67]   Naito M., Nomura H., Iguchi A., Thompson W. D., and Smith E. B., 1998, "Effect of Crosslinking by Factor XIIIa on the Migration of Vascular Smooth Muscle Cells into Fibrin Gels," Thromb. Res., **90**(3), pp. 111–116.

[68]   Ho W., Tawil B., Dunn J. C. Y., and Wu B. M., 2006, "The Behavior of Human Mesenchymal Stem Cells in 3D Fibrin Clots: Dependence on Fibrinogen Concentration and Clot Structure," Tissue Eng., **12**(6), pp. 1587–1595.

[69]   Wood G. C., and Keech M. K., 1960, "The Formation of Fibrils From Collagen Solutions 1. The Effect of Experimental Conditions: Kinetic and Electron-Microscope Studies," Biochem. J., **75**(3), pp. 588–598.

[70]   Roeder B. A., Kokini K., Sturgis J. E., Robinson J. P., and Voytik-Harbin S. L., 2002, "Tensile Mechanical Properties of Three-Dimensional Type I Collagen Extracellular Matrices With Varied Microstructure," J. Biomech. Eng., **124**(2), pp. 214–222.

[71]   Mosesson M. W., Siebenlist K. R., and Meh D. A., 2001, "The Structure and Biological Features of Fibrinogen and Fibrin," Ann. NY Acad. Sci., **936**, pp. 11–30.

[72]   Kadler K. E., Holmes D. F., Trotter J. A., and Chapman J. A., 1996, "Collagen Fibril Formation," Biochem. J., **316**(Pt 1), pp. 1–11.

[73]   Eb S., 1986, "Fibrinogen, Fibrin and Fibrin Degradation Products in Relation to Atherosclerosis," Clin. Haematol., **15**(2), p. 355.

[74]   Martin P., 1997, "Wound Healing--Aiming for Perfect Skin Regeneration," Science, **276**(5309), pp. 75–81.

[75]   Stein A. M., Vader D. A., Jawerth L. M., Weitz D. A., and Sander L. M., 2008, "An Algorithm for Extracting the Network Geometry of Three-Dimensional Collagen Gels," J. Microsc., **232**(3), pp. 463–475.

[76]   Fratzl P., Misof K., Zizak I., Rapp G., Amenitsch H., and Bernstorff S., 1998, "Fibrillar Structure and Mechanical Properties of Collagen," J. Struct. Biol., **122**(1–2), pp. 119–122.

[77]   Chandran P. L., and Barocas V. H., 2004, "Microstructural Mechanics of Collagen Gels in Confined Compression: Poroelasticity, Viscoelasticity, and Collapse," J. Biomech. Eng., **126**(2), pp. 152–166.

[78]   Purohit P. K., Litvinov R. I., Brown A. E. X., Discher D. E., and Weisel J. W., 2011, "Protein Unfolding Accounts for the Unusual Mechanical Behavior of Fibrin Networks," Acta Biomater., **7**(6), pp. 2374–2383.

[79]   Soulhat J., Buschmann M. D., and Shirazi-Adl A., 1999, "A Fibril-Network-Reinforced Biphasic Model of Cartilage in Unconfined Compression," J. Biomech. Eng., **121**(3), pp. 340–347.

[80]   Nachtrab S., Kapfer S. C., Arns C. H., Madadi M., Mecke K., and Schröder-Turk G. E., 2011, "Morphology and Linear-Elastic Moduli of Random Network Solids," Adv. Mater., **23**(22-23), pp. 2633–2637.

[81]   Fung Y. C., 1967, "Elasticity of Soft Tissues in Simple Elongation," Am. J. Physiol., **213**(6), pp. 1532–1544.

[82]   Humphrey J. D., 1994, "Mechanics of the Arterial Wall: Review and Directions," Crit. Rev. Biomed. Eng., **23**(1-2), pp. 1–162.

[83]   Horgan C. O., and Saccomandi G., 2003, "A Description of Arterial Wall Mechanics Using Limiting Chain Extensibility Constitutive Models," Biomech. Model. Mechanobiol., **1**(4), pp. 251–266.

[84]   Lanir Y., 1979, "A Structural Theory for the Homogeneous Biaxial Stress-Strain Relationships in Flat Collagenous Tissues," J. Biomech., **12**(6), pp. 423–436.

[85]   Decraemer W. F., Maes M. A., and Vanhuyse V. J., 1980, "An Elastic Stress-Strain Relation for Soft Biological Tissues Based on a Structural Model," J. Biomech., **13**(6), pp. 463–468.

[86]   Kwan M. K., and Woo S. L.-Y., "A Structural Model to Describe the Nonlinear Stress-Strain Behavior for Parallel-Fibered Collagenous Tissues," J. Biomech. Eng., **111**(4), pp. 361–363.

[87]   Cortes D. H., Lake S. P., Kadlowec J. A., Soslowsky L. J., and Elliott D. M., 2010, "Characterizing the Mechanical Contribution of Fiber Angular Distribution in Connective Tissue: Comparison of two Modeling Approaches," Biomech. Model. Mechanobiol., **9**(5), pp. 651–658.

[88]   Wagner H. P., and Humphrey J. D., "Differential Passive and Active Biaxial Mechanical Behaviors of Muscular and Elastic Arteries: Basilar Versus Common Carotid," J. Biomech. Eng., **133**(5).

[89]   Hollander Y., Durban D., Lu X., Kassab G. S., and Lanir Y., 2011, "Experimentally Validated Microstructural 3D Constitutive Model of Coronary Arterial Media," J. Biomech. Eng., **133**(3), p. 031007.

[90]   Kao P. H., Lammers S., Tian L., Hunter K., Stenmark K. R., Shandas R., and Qi H. J., 2011, "A Microstructurally-Driven Model for Pulmonary Artery Tissue," J. Biomech. Eng., **133**(5), p. 051002.

[91]   Soares A. L. F., Stekelenburg M., and Baaiiens F. P. T., "Remodeling of the Collagen Fiber Architecture Due to Compaction in Small Vessels Under Tissue Engineered Conditions," J. Biomech. Eng., **133**(7).

[92]   Szczesny S. E., Peloquin J. M., Cortes D. H., Kadlowec J. A., Soslowsky L. J., and Elliott D. M., 2012, "Biaxial Tensile Testing and Constitutive Modeling of Human Supraspinatus Tendon," J. Biomech. Eng., **134**(2), pp. 021004–1.

[93]   Holzapfel G. A., Gasser T. C., and Ogden R. W., 2000, "A New Constitutive Framework for Arterial Wall Mechanics and a Comparative Study of Material Models," J. Elasticity, **61**(1-3), pp. 1–48.

[94]   Driessen N. J. B., Bouten C. V. C., and Baaijens F. P. T., 2005, "A Structural Constitutive Model For Collagenous Cardiovascular Tissues Incorporating the Angular Fiber Distribution," J. Biomech. Eng., **127**(3), p. 494.

[95]   Tang H., Buehler M. J., and Moran B., 2009, "A Constitutive Model of Soft Tissue: From Nanoscale Collagen to Tissue Continuum," Ann. Biomed. Eng., **37**(6), pp. 1117–1130.

[96]   Nagel T., and Kelly D. J., 2012, "Remodelling of Collagen Fibre Transition Stretch and Angular Distribution in Soft Biological Tissues and Cell-Seeded Hydrogels," Biomech. Model. Mechanobiol., **11**(3-4), pp. 325–339.

[97]   Quapp K. M., and Weiss J. A., 1998, "Material Characterization of Human Medial Collateral Ligament," J. Biomech. Eng., **120**(6), p. 757.

[98]   Guerin H. L., and Elliott D. M., 2007, "Quantifying the Contributions of Structure to Annulus Fibrosus Mechanical Function Using a Nonlinear, Anisotropic, Hyperelastic Model," J. Orthop. Res., **25**(4), pp. 508–516.

[99]   Abraham A. C., Moyer J. T., Villegas D. F., Odegard G. M., and Haut Donahue T. L., 2011, "Hyperelastic Properties of Human Meniscal Attachments," J. Biomech., **44**(3), pp. 413–418.

[100] Cortes D. H., and Elliott D. M., 2012, "Extra-Fibrillar Matrix Mechanics of Annulus Fibrosus in Tension and Compression," Biomech. Model. Mechanobiol., **11**(6), pp. 781–790.

[101] Wagner D. R., and Lotz J. C., 2004, "Theoretical Model and Experimental Results for the Nonlinear Elastic Behavior of Human Annulus Fibrosus," J. Orthop. Res., **22**(4), pp. 901–909.

[102] Peng X. Q., Guo Z. Y., and Moran B., "An Anisotropic Hyperelastic Constitutive Model With Fiber-Matrix Shear Interaction for the Human Annulus Fibrosus," J. Appl. Mech., **73**(5), pp. 815–824.

[103] O'Connell G. D., Guerin H. L., and Elliott D. M., 2009, "Theoretical and Uniaxial Experimental Evaluation of Human Annulus Fibrosus Degeneration," J. Biomech. Eng., **131**(11), p. 111007.

[104] Lake S. P., Hadi M. F., Lai V. K., and Barocas V. H., 2012, "Mechanics of a Fiber Network Within a Non-Fibrillar Matrix: Model and Comparison With Collagen-Agarose Co-Gels," Ann. Biomed. Eng., **40**(10), pp. 2111–2121.

[105] Chandran P. L., and Barocas V. H., 2006, "Affine Versus Non-Affine Fibril Kinematics in Collagen Networks: Theoretical Studies of Network Behavior," J. Biomech. Eng., **128**(2), pp. 259–270.

[106] Kang J., Steward R. L., Kim Y., Schwartz R. S., LeDuc P. R., and Puskar K. M., 2011, "Response of an Actin Filament Network Model Under Cyclic Stretching Through a Coarse Grained Monte Carlo Approach," J. Theor. Biol., **274**(1), pp. 109–119.

[107] Stein A. M., Vader D. A., Weitz D. A., and Sander L. M., 2011, "The Micromechanics of Three-Dimensional Collagen-I Gels," Complexity, **16**(4), pp. 22–28.

[108] Holzapfel G., 2000, Nonlinear Solid Mechanics: A Continuum Approach for Engineering, John Wiley & Sons Ltd.

[109] Nagel T., and Kelly D. J., 2010, "The Influence of Fiber Orientation on the Equilibrium Properties of Neutral and Charged Biphasic Tissues," J. Biomech. Eng., **132**(11), p. 114506.

[110] Benkherourou M., Rochas C., Tracqui P., Tranqui L., and Guméry P. Y., 1999, "Standardization of a Method for Characterizing Low-Concentration Biogels: Elastic Properties of Low-Concentration Agarose Gels," J. Biomech. Eng., **121**(2), p. 184.

[111] Lake S. P., Hald E. S., and Barocas V. H., 2011, "Collagen-Agarose Co-Gels as a Model for Collagen–Matrix Interaction in Soft Tissues Subjected to Indentation," J. Biomed. Mater. Res. A, **99A**(4), pp. 507–515.

[112] Weiler K., 1988, "The Radial Edge Structure: A Topological Representation for Non-Manifold Geometric Boundary Modeling," Geometric modeling for CAD applications, pp. 3–36.

[113] "Parasolid: Siemens PLM Software."

[114] "Simmetrix Inc. - Mesh Generation, Geometry Access."

[115] Shephard M. S., 2000, "Meshing Environment for Geometry-Based Analysis," Int. J. Numer. Meth. Eng, **47**(1-3), pp. 169–190.

[116] Franck C., Maskarinec S. A., Tirrell D. A., and Ravichandran G., 2011, "Three-Dimensional Traction Force Microscopy: A New Tool for Quantifying Cell-Matrix Interactions," PLoS ONE, **6**(3), p. e17833.

[117] Hadi M. F., Sander E. A., and Barocas V. H., 2012, "Multiscale Model Predicts Tissue-Level Failure From Collagen Fiber-Level Damage," J. Biomech. Eng., **134**(9), p. 091005.

[118] Hadi M. F., Sander E. A., Ruberti J. W., and Barocas V. H., 2012, "Simulated Remodeling of Loaded Collagen Networks via Strain-Dependent Enzymatic Degradation and Constant-Rate Fiber Growth," Mech. Mater., **44**, pp. 72–82.

[119] Pence T. J., Monroe R. J., and Wright N. T., 2008, "On the Computation of Stress in Affine Versus Nonaffine Fibril Kinematics Within Planar Collagen Network Models," J. Biomech. Eng., **130**(4), p. 041009.

[120] Sopakayang R., De Vita R., Kwansa A., and Freeman J. W., 2012, "Elastic and Viscoelastic Properties of a Type I Collagen Fiber," J. Theor. Biol., **293**, pp. 197–205.

[121] Silver F. H., Ebrahimi A., and Snowhill P. B., 2002, "Viscoelastic Properties of Self-Assembled Type I Collagen Fibers: Molecular Basis of Elastic and Viscous Behaviors," Connect. Tissue Res., **43**(4), pp. 569–580.

[122] Broedersz C. P., Sheinman M., and MacKintosh F. C., 2012, "Filament-Length-Controlled Elasticity in 3D Fiber Networks," Phys. Rev. Lett., **108**(7), p. 078102.

[123] Head D. A., Levine A. J., and MacKintosh F. C., 2003, "Distinct Regimes of Elastic Response and Deformation Modes of Cross-Linked Cytoskeletal and Semiflexible Polymer Networks," Phys. Rev. E, **68**(6), p. 061907.

[124] Knapp D. M., Barocas V. H., Moon A. G., Yoo K., Petzold L. R., and Tranquillo R. T., 1997, "Rheology of Reconstituted Type I Collagen gel in Confined Compression," J. Rheol., **41**(5), pp. 971–993.

[125] Hsu S., Jamieson A. M., and Blackwell J., 1993, "Viscoelastic Studies of Extracellular Matrix Interactions in a Model Native Collagen gel System," Biorheology, **31**(1), pp. 21–36.

[126] Meghezi S., Couet F., Chevallier P., and Mantovani D., 2012, "Effects of a Pseudophysiological Environment on the Elastic and Viscoelastic Properties of Collagen Gels," Int. J. Biomater., **2012**, pp. 1–9.

[127] Krishnan L., Weiss J. A., Wessman M. D., and Hoying J. B., 2004, "Design and Application of a Test System for Viscoelastic Characterization of Collagen Gels," Tissue Eng., **10**(1-2), pp. 241–252.

[128] Pryse K. M., Nekouzadeh A., Genin G. M., Elson E. L., and Zahalak G. I., 2003, "Incremental Mechanics of Collagen Gels: New Experiments and a New Viscoelastic Model," Ann. Biomed. Eng., **31**(10), pp. 1287–1296.

[129] Jhun C.-S., Evans M. C., Barocas V. H., and Tranquillo R. T., 2009, "Planar Biaxial Mechanical Behavior of Bioartificial Tissues Possessing Prescribed Fiber Alignment," J. Biomech. Eng., **131**(8), p. 081006.

[130] Lake S. P., Cortes D. H., Kadlowec J. A., Soslowsky L. J., and Elliott D. M., 2012, "Evaluation of Affine Fiber Kinematics in Human Supraspinatus Tendon Using Quantitative Projection Plot Analysis," Biomech. Model. Mechanobiol., **11**(1-2), pp. 197–205.

[131] Lanir Y., 2012, "Osmotic Swelling and Residual Stress in Cardiovascular Tissues," J. Biomech., **45**(5), pp. 780–789.

[132] Weiss J. A., and Gardiner J. C., 2001, "Computational Modeling of Ligament Mechanics," Crit. Rev. Biomed. Eng., **29**(3), pp. 303–371.

[133] Michalek A. J., Gardner-Morse M. G., and Iatridis J. C., 2012, "Large Residual Strains are Present in the Intervertebral Disc Annulus Fibrosus in the Unloaded State," J. Biomech., **45**(7), pp. 1227–1231.

[134] Laurent T. C., 1998, The Chemistry, Biology and Medical Applications of Hyaluronan and Its Derivatives, Portland Press, Limited.

[135] Alexander S. A., and Donoff R. B., 1980, "The Glycosaminoglycans of Open Wounds," J. Surg. Res., **29**(5), pp. 422–429.

[136] Crouzier T., and Picart C., 2009, "Ion Pairing and Hydration in Polyelectrolyte Multilayer Films Containing Polysaccharides," Biomacromolecules, **10**(2), pp. 433–442.

[137] Greco R. M., Iocono J. A., and Ehrlich H. P., 1998, "Hyaluronic Acid Stimulates Human Fibroblast Proliferation Within a Collagen Matrix," J. Cell. Physio., **177**(3), pp. 465–473.

[138] Kawasaki K., Ochi M., Uchio Y., Adachi N., and Matsusaki M., 1999, "Hyaluronic Acid Enhances Proliferation and Chondroitin Sulfate Synthesis in

Cultured Chondrocytes Embedded in Collagen Gels," J. Cell. Physio., **179**(2), pp. 142–148.

[139] Matsiko A., Levingstone T. J., O'Brien F. J., and Gleeson J. P., 2012, "Addition of Hyaluronic Acid Improves Cellular Infiltration and Promotes Early-Stage Chondrogenesis in a Collagen-Based Scaffold for Cartilage Tissue Engineering," J. Mech. Behav. Biomed. Mater., **11**, pp. 41–52.

[140] Park S.-N., Lee H. J., Lee K. H., and Suh H., 2003, "Biological characterization of EDC-crosslinked collagen–hyaluronic acid matrix in dermal tissue restoration," Biomaterials, **24**(9), pp. 1631–1641.

[141] Davidenko N., Campbell J. J., Thian E. S., Watson C. J., and Cameron R. E., 2010, "Collagen–Hyaluronic Acid Scaffolds for Adipose Tissue Engineering," Acta Biomater., **6**(10), pp. 3957–3968.

[142] Choh S.-Y., Cross D., and Wang C., 2011, "Facile Synthesis and Characterization of Disulfide-Cross-Linked Hyaluronic Acid Hydrogels for Protein Delivery and Cell Encapsulation," Biomacromolecules, **12**(4), pp. 1126–1136.

[143] Luo Y., Kirker K. R., and Prestwich G. D., 2000, "Cross-Linked Hyaluronic Acid Hydrogel Films: New Biomaterials for Drug Delivery," J. Controlled Release, **69**(1), pp. 169–184.

[144] Segura T., Anderson B. C., Chung P. H., Webber R. E., Shull K. R., and Shea L. D., 2005, "Crosslinked hyaluronic Acid Hydrogels: A Strategy to Functionalize and Pattern," Biomaterials, **26**(4), pp. 359–371.

[145] Anandagoda N., Ezra D. G., Cheema U., Bailly M., and Brown R. A., 2012, "Hyaluronan hydration generates three-dimensional meso-scale structure in engineered collagen tissues," J. R. Soc. Interface, **9**(75), pp. 2680–2687.

[146] Suri S., and Schmidt C. E., 2009, "Photopatterned Collagen–Hyaluronic Acid Interpenetrating Polymer Network Hydrogels," Acta Biomater., **5**(7), pp. 2385–2397.

[147] Donnan F. G., 1924, "The Theory of Membrane Equilibria.," Chem. Rev., **1**(1), pp. 73–90.

[148] Moon A. G., and Tranquillo R. T., 1993, "Fibroblast-Populated Collagen Microsphere Assay of Cell Traction Force: Part 1. Continuum Model," AIChE J., **39**(1), pp. 163–177.

[149] Lai W. M., Hou J. S., and Mow V. C., 1991, "A Triphasic Theory for the Swelling and Deformation Behaviors of Articular Cartilage," J. Biomech. Eng., **113**(3), p. 245.

[150] Lai V. K., Frey C. R., Kerandi A. M., Lake S. P., Tranquillo R. T., and Barocas V. H., 2012, "Microstructural and Mechanical Differences Between Digested Collagen–Fibrin Co-Gels and Pure Collagen and Fibrin Gels," Acta Biomater., **8**(11), pp. 4031–4042.

[151] Lanir Y., 2009, "Mechanisms of Residual Stress in Soft Tissues," J. Biomech. Eng., **131**(4), p. 044506.

[152] Humphrey J. D., 2003, "Review Paper: Continuum Biomechanics of Soft Biological Tissues," Proc. R. Soc. Lond. A, **459**(2029), pp. 3–46.

[153] Humphrey J. D., and Yin F. C., 1989, "Constitutive Relations and Finite Deformations of Passive Cardiac Tissue II: Stress Analysis in the Left Ventricle.," Circ. Res., **65**(3), pp. 805–817.

[154] Gasser T. C., Ogden R. W., and Holzapfel G. A., 2006, "Hyperelastic Modelling of Arterial Layers With Distributed Collagen Fibre Orientations," J. R. Soc. Interface, **3**(6), pp. 15–35.

[155] Hu J.-J., Baek S., and Humphrey J. D., 2007, "Stress–Strain Behavior of the Passive Basilar Artery in Normotension and Hypertension," J. Biomech., **40**(11), pp. 2559–2563.

[156] Marquez J. P., Genin G. M., Zahalak G. I., and Elson E. L., 2005, "The Relationship between Cell and Tissue Strain in Three-Dimensional Bio-Artificial Tissues," Biophys. J., **88**(2), pp. 778–789.

[157] Barocas V. H., and Tranquillo R. T., 1997, "An Anisotropic Biphasic Theory of Tissue-Equivalent Mechanics: The Interplay Among Cell Traction, Fibrillar Network Deformation, Fibril Alignment, and Cell Contact Guidance," J. Biomech. Eng., **119**(2), p. 137.

[158] Stevenson M. D., Sieminski A. L., McLeod C. M., Byfield F. J., Barocas V. H., and Gooch K. J., 2010, "Pericellular Conditions Regulate Extent of Cell-Mediated Compaction of Collagen Gels," Biophys. J., **99**(1), pp. 19–28.

[159] Guilak F., and Mow V. C., 2000, "The Mechanical Environment of the Chondrocyte: A Biphasic Finite Element Model ff Cell–Matrix Interactions in Articular Cartilage," J. Biomech., **33**(12), pp. 1663–1673.

[160] Breuls R. G. M., Sengers B. G., Oomens C. W. J., Bouten C. V. C., and Baaijens F. P. T., 2002, "Predicting Local Cell Deformations in Engineered Tissue Constructs: A Multilevel Finite Element Approach," J. Biomech. Eng., **124**(2), p. 198.

[161] Stamenović D., Fredberg J. J., Wang N., Butler J. P., and Ingber D. E., 1996, "A Microstructural Approach to Cytoskeletal Mechanics Based on Tensegrity," J. Theor. Biol., **181**(2), pp. 125–136.

[162] Wang N., Naruse K., Stamenović D., Fredberg J. J., Mijailovich S. M., Tolić-Nørrelykke I. M., Polte T., Mannix R., and Ingber D. E., 2001, "Mechanical Behavior in Living Cells Consistent With the Tensegrity Model," Proc. Natl. Acad. Sci., **98**(14), pp. 7765–7770.

[163] Coughlin M. F., and Stamenović D., 1998, "A Tensegrity Model of the Cytoskeleton in Spread and Round Cells," J. Biomech. Eng., **120**(6), p. 770.

[164] Stamenovic D., and Coughlin M. F., 2000, "A Quantitative Model of Cellular Elasticity Based on Tensegrity," J. Biomech. Eng., **122**(1), pp. 39–43.

[165] Gibson L. J., and Ashby M. F., 1999, Cellular Solids: Structure and Properties, Cambridge University Press.

[166] Satcher Jr R. L., and Dewey Jr C. F., 1996, "Theoretical Estimates of Mechanical Properties of the Endothelial Cell Cytoskeleton," Biophys. J., **71**(1), pp. 109–118.

[167] Susilo M. E., Roeder B. A., Voytik-Harbin S. L., Kokini K., and Nauman E. A., 2010, "Development of a Three-Dimensional Unit Cell to Model the

Micromechanical Response of a Collagen-Based Extracellular Matrix," Acta Biomater., **6**(4), pp. 1471–1486.

[168] Isambert H., and Maggs A. C., 1996, "Dynamics and Rheology of Actin Solutions," Macromolecules, **29**(3), pp. 1036–1040.

[169] Storm C., Pastore J. J., MacKintosh F. C., Lubensky T. C., and Janmey P. A., 2005, "Nonlinear Elasticity in Biological Gels," Nature, **435**(7039), pp. 191–194.

[170] Palmer J. S., and Boyce M. C., 2008, "Constitutive Modeling of the Stress–Strain Behavior of F-Actin Filament Networks," Acta Biomater., **4**(3), pp. 597–612.

[171] Zhang L., Lake S. P., Lai V. K., Picu C. R., Barocas V. H., and Shephard M. S., 2013, "A Coupled Fiber-Matrix Model Demonstrates Highly Inhomogeneous Microstructural Interactions in Soft Tissues Under Tensile Load," J. Biomech. Eng., **135**(1), p. 011008.

[172] Evans M. C., and Barocas V. H., 2009, "The Modulus of Fibroblast-Populated Collagen Gels is not Determined by Final Collagen and Cell Concentration: Experiments and an Inclusion-Based Model," J. Biomech. Eng., **131**(10), pp. 101014–1 – 101014–7.

[173] Bonet J., and Wood R. D., 1997, Nonlinear Continuum Mechanics for Finite Element Analysis, Cambridge University Press.

[174] Roy S., Silacci P., and Stergiopulos N., 2005, "Biomechanical Properties of Decellularized Porcine Common Carotid Arteries," Am. J. Physiol. Heart Circ. Physiol., **289**(4), pp. H1567–H1576.

[175] Lynch H. A., Johannessen W., Wu J. P., Jawa A., and Elliott D. M., 2003, "Effect of Fiber Orientation and Strain Rate on the Nonlinear Uniaxial Tensile Material Properties of Tendon," J. Biomech. Eng., **125**(5), p. 726.

[176] Lake S. P., Miller K. S., Elliott D. M., and Soslowsky L. J., 2010, "Tensile Properties and Fiber Alignment of Human Supraspinatus Tendon in the Transverse Direction Demonstrate Inhomogeneity, Nonlinearity, and Regional Isotropy," J. Biomech., **43**(4), pp. 727–732.

[177] Cheng V. W. T., and Screen H. R. C., 2007, "The Micro-Structural Strain Response of Tendon," J. Mater. Sci., **42**(21), pp. 8957–8965.

[178] Burridge K., Fath K., Kelly T., Nuckolls G., and Turner C., 1988, "Focal Adhesions: Transmembrane Junctions Between the Extracellular Matrix and the Cytoskeleton," Annu. Rev. Cell Biol., **4**(1), pp. 487–525.

[179] Goffin J. M., Pittet P., Csucs G., Lussi J. W., Meister J.-J., and Hinz B., 2006, "Focal Adhesion Size Controls Tension-Dependent Recruitment of α-Smooth Muscle Actin to Stress Fibers," J. Cell. Biol., **172**(2), pp. 259–268.

[180] Durrant L. A., Archer C. W., Benjamin M., and Ralphs J. R., 1999, "Organisation of the Chondrocyte Cytoskeleton and its Response to Changing Mechanical Conditions in Organ Culture," J. Anat., **194**(3), pp. 343–353.

[181] Eggli P. S., Hunzinker E. B., and Schenk R. K., 1988, "Quantitation of Structural Features Characterizing Weight- and Less-Weight-Bearing Regions in Articular Cartilage: A Stereological Analysis of Medical Femoral Condyles in Young Adult Rabbits," Anat. Rec., **222**(3), pp. 217–227.

[182] Janmey P. A., and McCulloch C. A., 2007, "Cell Mechanics: Integrating Cell Responses to Mechanical Stimuli," Annu. Rev. Biomed. Eng., **9**(1), pp. 1–34.

[183] Ofek G., Wiltz D. C., and Athanasiou K. A., 2009, "Contribution of the Cytoskeleton to the Compressive Properties and Recovery Behavior of Single Cells," Biophys. J., **97**(7), pp. 1873–1882.

[184] Eastwood M., Mudera V. c., Mcgrouther D. a., and Brown R. a., 1998, "Effect of Precise Mechanical Loading on Fibroblast Populated Collagen Lattices: Morphological Changes," Cell Motil. Cytoskel., **40**(1), pp. 13–21.

[185] Huang D., Chang T. R., Aggarwal A., Lee R. C., and Ehrlich H. P., 1993, "Mechanisms and Dynamics of Mechanical Strengthening in Ligament-Equivalent Fibroblast-Populated Collagen Matrices," Ann. Biomed. Eng., **21**(3), pp. 289–305.

[186] Chan C. E., and Odde D. J., 2008, "Traction Dynamics of Filopodia on Compliant Substrates," Science, **322**(5908), pp. 1687–1691.

[187] Yeung T., Georges P. C., Flanagan L. A., Marg B., Ortiz M., Funaki M., Zahir N., Ming W., Weaver V., and Janmey P. A., 2005, "Effects of Substrate Stiffness on Cell Morphology, Cytoskeletal Structure, and Adhesion," Cell Motil. Cytoskel., **60**(1), pp. 24–34.

[188] Subramanian A., and Lin H.-Y., 2005, "Crosslinked Chitosan: Its Physical Properties and the Effects of Matrix Stiffness on Chondrocyte Cell Morphology and Proliferation," J. Biomed. Mater. Res. A, **75A**(3), pp. 742–753.

[189] Engler A. J., Sen S., Sweeney H. L., and Discher D. E., 2006, "Matrix Elasticity Directs Stem Cell Lineage Specification," Cell, **126**(4), pp. 677–689.

[190] Hadjipanayi E., Mudera V., and Brown R. A., 2009, "Guiding Cell Migration in 3D: A Collagen Matrix with Graded Directional Stiffness," Cell Motil. Cytoskel., **66**(3), pp. 121–128.

[191] Legant W. R., Miller J. S., Blakely B. L., Cohen D. M., Genin G. M., and Chen C. S., 2010, "Measurement of Mechanical Tractions Exerted by Cells in Three-Dimensional Matrices," Nature Methods, **7**(12), pp. 969–971.

[192] Pizzo A. M., Kokini K., Vaughn L. C., Waisner B. Z., and Voytik-Harbin S. L., 2005, "Extracellular Matrix (ECM) Microstructural Composition Regulates Local Cell-ECM Biomechanics and Fundamental Fibroblast Behavior: A Multidimensional Perspective," J Appl Physiol, **98**(5), pp. 1909–1921.

[193] Holzapfel G. A., Gasser T. C., and Stadler M., 2002, "A structural model for the viscoelastic behavior of arterial walls: Continuum formulation and finite element analysis," European Journal of Mechanics - A/Solids, **21**(3), pp. 441–463.

[194] Doehring T. C., Carew E. O., and Vesely I., 2004, "The Effect of Strain Rate on the Viscoelastic Response of Aortic Valve Tissue: A Direct-Fit Approach," Annals of Biomedical Engineering, **32**(2), pp. 223–232.

[195] Trickey W. R., Vail T. P., and Guilak F., 2004, "The Role of the Cytoskeleton in the Viscoelastic Properties of Human Articular Chondrocytes," J. Orthop. Res., **22**(1), pp. 131–139.

[196] Ulrich T. A., Jain A., Tanner K., MacKay J. L., and Kumar S., 2010, "Probing Cellular Mechanobiology in Three-Dimensional Culture with Collagen–Agarose Matrices," Biomaterials, **31**(7), pp. 1875–1884.

[197] Ault H. K., and Hoffman A. H., 1992, "A Composite Micromechanical Model for Connective Tissues: Part I--Theory," J. Biomech. Eng., **114**(1), pp. 137–141.

[198] Horowitz A., Lanir Y., Yin F. C.-P., Perl M., Sheinman I., and Strumpf R., 1988, "Structural Three-Dimensional Constitutive law for the Passive Myocardium," J. Biomech. Eng., **110**(3), pp. 200–207.

[199] Horowitz A., Sheinman I., and Lanir Y., 1988, "Nonlinear Incompressible Finite Element for Simulating Loading of Cardiac Tissue--Part II: Three Dimensional Formulation for Thick Ventricular Wall Segments," J. Biomech. Eng., **110**(1), pp. 62–68.

[200] Kiviranta P., Rieppo J., Korhonen R. K., Julkunen P., Töyräs J., and Jurvelin J. S., 2006, "Collagen Network Primarily Controls Poisson's Ratio of Bovine Articular Cartilage in Compression," J. Orthop. Res., **24**(4), pp. 690–699.

[201] Martufi G., and Gasser T. C., 2011, "A Constitutive Model for Vascular Tissue that Integrates Fibril, Fiber and Continuum Levels with Application to the Isotropic and Passive Properties of the Infrarenal Aorta," J. Biomech., **44**(14), pp. 2544–2550.

[202] Raghupathy R., and Barocas V. H., 2009, "A Closed-Form Structural Model of Planar Fibrous Tissue Mechanics," J. Biomech., **42**(10), pp. 1424–1428.

[203] Arruda E. M., and Boyce M. C., 1993, "A Three-Dimensional Constitutive Model for the Large Stretch Behavior of Rubber Elastic Materials," J. Mech. Phys. Solids, **41**(2), pp. 389–412.

[204] Bischoff J. E., Arruda E. A., and Grosh K., "A Microstructurally Based Orthotropic Hyperelastic Constitutive law," J. Appl. Mech., **69**(5), pp. 570–579.

[205] Kabla A., and Mahadevan L., 2007, "Nonlinear Mechanics of Soft Fibrous Networks," J. R. Soc. Interface, **4**(12), pp. 99–106.

[206] Kuhl E., Garikipati K., Arruda E. M., and Grosh K., 2005, "Remodeling of biological Tissue: Mechanically Induced Reorientation of a Transversely Isotropic Chain Network," J. Mech. Phys. Solids, **53**(7), pp. 1552–1573.

[207] Sander E. A., Downs J. C., Hart R. T., Burgoyne C. F., and Nauman E. A., "A Cellular Solid Model of the Lamina Cribrosa : Mechanical Dependence on Morphology," J. Biomech. Eng., **128**(6), pp. 879–889.

[208] Ritter M. C., Jesudason R., Majumdar A., Stamenović D., Buczek-Thomas J. A., Stone P. J., Nugent M. A., and Suki B., 2009, "A Zipper Network Model of the Failure Mechanics of Extracellular Matrices," Proc. Natl. Acad. Sci., **106**(4), pp. 1081–1086.

[209] Sander E. A., and Barocas V. H., 2009, "Comparison of 2D Fiber Network Orientation Measurement Methods," J. Biomed. Mater. Res. A, **88A**(2), pp. 322–331.

[210] Billiar K. L., and Sacks M. S., 1997, "A Method to Quantify the Fiber Kinematics of Planar Tissues Under Biaxial Stretch," J. Biomech., **30**(7), pp. 753–756.

[211] Gilbert T. W., Sacks M. S., Grashow J. S., Woo S. L.-Y., Badylak S. F., and Chancellor M. B., 2006, "Fiber Kinematics of Small Intestinal Submucosa Under Biaxial and Uniaxial Stretch," J. Biomech. Eng., **128**(6), pp. 890–898.

[212] Guerin H. A. L., and Elliott D. M., 2006, "Degeneration Affects the Fiber Reorientation of Human Annulus Fibrosus Under Tensile Load," J. Biomech., **39**(8), pp. 1410–1418.

[213] Hepworth D. G., Steven-fountain A., Bruce D. M., and Vincent J. F. V., 2001, "Affine Versus Non-Affine Deformation in Soft Biological Tissues, Measured by the Reorientation and Stretching of Collagen Fibres Through the Thickness of Compressed Porcine Skin," J. Biomech., **34**(3), pp. 341–346.

[214] Ault H. K., and Hoffman A. H., 1992, "A Composite Micromechanical Model for Connective Tissues: Part II--Application to rat Tail Tendon and Joint Capsule," J. Biomech. Eng., **114**(1), pp. 142–146.

[215] Driessen N. J. B., Boerboom R. A., Huyghe J. M., Bouten C. V. C., and Baaijens F. P. T., 2003, "Computational Analyses of Mechanically Induced Collagen Fiber Remodeling in the Aortic Heart Valve," J. Biomech. Eng., **125**(4), p. 549.

[216] Driessen N. J. B., Cox M. A. J., Bouten C. V. C., and Baaijens F. P. T., 2008, "Remodelling of the Angular Collagen Fiber Distribution in Cardiovascular Tissues," Biomech. Model. Mechanobiol., **7**(2), pp. 93–103.

[217] Driessen N. J. B., Wilson W., Bouten C. V. C., and Baaijens F. P. T., 2004, "A Computational Model for Collagen Fibre Remodelling in the Arterial Wall," J. Theor. Biol., **226**(1), pp. 53–64.

[218] Horowitz A., Sheinman I., Lanir Y., Perl M., and Sideman S., 1988, "Nonlinear Incompressible Finite Element for Simulating Loading of Cardiac Tissue--Part I: Two Dimensional Formulation for Thin Myocardial Strips," J. Biomech. Eng., **110**(1), pp. 57–61.

[219] Julkunen P., Harjula T., Marjanen J., Helminen H. J., and Jurvelin J. S., 2009, "Comparison of Single-Phase Isotropic Elastic and Fibril-Reinforced Poroelastic Models for Indentation of Rabbit Articular Cartilage," J. Biomech., **42**(5), pp. 652–656.

[220] Maceri F., Marino M., and Vairo G., 2010, "A Unified Multiscale Mechanical Model for Soft Collagenous Tissues with Regular Fiber Arrangement," J. Biomech., **43**(2), pp. 355–363.

[221] Driessen N. J. B., Mol A., Bouten C. V. C., and Baaijens F. P. T., 2007, "Modeling the Mechanics of Tissue-Engineered Human Heart Valve Leaflets," J. Biomech., **40**(2), pp. 325–334.

[222] Amoroso N. J., D'Amore A., Hong Y., Wagner W. R., and Sacks M. S., 2011, "Elastomeric Electrospun Polyurethane Scaffolds: The Interrelationship Between Fabrication Conditions, Fiber Topology, and Mechanical Properties," Adv. Mater., **23**(1), pp. 106–111.

[223] D'Amore A., Stella J. A., Wagner W. R., and Sacks M. S., 2010, "Characterization of the complete fiber network topology of planar fibrous tissues and scaffolds," Biomaterials.

[224] Hewitt J., Guilak F., Glisson R., and Vail T. P., 2001, "Regional Material Properties of the Human hip Joint Capsule Ligaments," J. Orthop. Res., **19**(3), pp. 359–364.

[225] Lake S. P., 2009, "Anisotropic, Inhomogeneous and Nonlinear Structure-Function of Human Supraspinatus Tendon," PhD. Thesis, University of Pennsylvania: Philadelphia, PA, pp. 1–243.

[226] Lake S. P., Miller K. S., Elliott D. M., and Soslowsky L. J., 2009, "Effect of Fiber Distribution and Realignment on the Nonlinear and Inhomogeneous Mechanical Properties of Human Supraspinatus Tendon Under Longitudinal Tensile Loading," J. Orthop. Res., **27**(12), pp. 1596–1602.

[227] Adeeb S., Ali A., Shrive N., Frank C., and Smith D., 2004, "Modelling the Behaviour of Ligaments: A Technical Note," Comput. Methods Biomech. Biomed. Eng., **7**(1), pp. 33–42.

[228] Wellen J., Helmer K. G., Grigg P., and Sotak C. H., 2004, "Application of Porous-Media Theory to the Investigation of Water ADC Changes in Rabbit Achilles Tendon Caused by Tensile Loading," J. Magn. Reson., **170**(1), pp. 49–55.

[229] Reese S. P., Maas S. A., and Weiss J. A., 2010, "Micromechanical Models of Helical Superstructures in Ligament and Tendon Fibers Predict Large Poisson's Ratios," J. Biomech., **43**(7), pp. 1394–1400.

Appendix A: Published Paper – Mechanics of a Fiber Network Within a Non-Fibrillar Matrix: Model and Comparison With Collagen-Agarose Co-Gels

The content of this Appendix was published in the Annals of Biomedical Engineering (May 2012). My contributions to this paper include active participation in discussions with the co-authors on the modeling results, and providing suggestions and feedback during the writing of the manuscript.

A.1 Introduction

In order to understand fully the functional mechanics of soft tissues, it is necessary to characterize the mechanical properties of each tissue constituent and elucidate how they interact and function together. While the mechanical role of collagen (the primary structural component of connective tissues) is often evaluated, less is known about the role of non-fibrillar matrix (NFM, e.g., proteoglycans, glycosaminoglycans, cells, etc.), which varies compositionally across tissue types. Our recent work [37,111] evaluated collagen-agarose tissue analogs (with agarose as a representative NFM) in uniaxial tension and indentation to characterize the contribution of the NFM under different loading scenarios. In these studies, agarose was selected to represent non-fibrillar matrix because of several advantageous characteristics, namely its biocompatibility, uncharged nature, and ability to intersperse between fibers of a collagen gel without disrupting the collagen network [196]. Results demonstrated that the NFM contributes significantly to the elastic and viscoelastic mechanical response and structural reorganization of soft tissues in a concentration-dependent manner, even in tensile testing in which collagen is normally assumed to be the predominant contributor. While these

studies have provided useful information, the mechanism by which NFM interacts with the collagen network on the microscale to alter the macroscale composite tissue properties remains unknown. Thus, the objective for the current work was to use a two-component microstructural model of the collagen-agarose system under quasi-static loading to elucidate the interaction between the collagen and the agarose during uniaxial extension of the co-gel.

Various approaches have been used to incorporate structural information into mechanical models of soft tissues. Three broad categories of model can be identified: isolated fiber [84,88,93,94,96–98,100,101,103,109,197–202], regular-fiber-cell [78,167,203–207], and large-network [48,80,106,107,169,208,209]. *Isolated-fiber* models, often expressed in terms of a continuum strain-energy function, are characterized by each fiber in the tissue behaving independently of the others and moving affinely with the macroscopic deformation. *Regular-fiber-cell* models involve a small unit cell (4-20 fibers) that is assumed to repeat within the tissue. These models capture some of the complex mechanical behavior of a tissue but can still be converted to a closed-form stress-strain (or strain energy) expression. Fibers within regular-fiber-cell models may be able to move non-affinely, but the cells themselves deform with the macroscopic boundary. Finally, *large-network* models involve a network of hundreds to thousands of fibers, often arranged randomly, that interact fully with each other. In this case, the network must be large enough that different networks with the same overall structural properties (alignment, crosslink density, etc.) produce the same stress-strain results even if the detailed structures are quite different. Highly non-affine kinematics exhibited by

133

interacting fibers are consistent with reports that collagen fiber kinematics in native tissues do not follow the affine assumption [130,210–213].

Each of these three modeling approaches exhibit specific advantages, and models constructed at each domain size (isolated fiber, regular-fiber-cell, large-network) have provided insight into the mechanical behavior of a variety of materials, including native soft tissues [48,94,100,109,198,200,201,214–220], biological tissue analogs [80,96,107,167,169,208,221], and biomimetic synthetic materials [205,222]. In addition to representing the collagen component, several previous models have also considered the contribution of the NFM. Within models based on non-interacting fibers, NFM has been represented, often via a neo-Hookean or Mooney-Rivlin formulation, as a summed contribution to the collagen stress [93–98,100,101,103,109,201]. Since each fiber in these models functions independently (of other fibers and the NFM) at the local level, interactions between tissue constituents cannot be evaluated. To capture such interactions, some models have included an additional term to incorporate the stress contribution due to interactions between the collagen network and NFM [98,101–103]. When the fiber architecture is precise and well known, the form of the interaction contribution can be suggested by the structure of the tissue (as in [98]). Unfortunately, for an unstructured fiber network the appropriate definition for the interaction term is unknown. For regular-fiber-cell models, the general tendency is to evaluate the collagen network alone, but a few studies have incorporated a "bulk" term to describe the contribution from non-collagenous material [204,206]. To date, however, these models have focused on the fiber component and have not been used to specifically evaluate the

role of NFM or how it interacts with fibrillar material to alter the composite tissue response. Similarly, large-network models have not generally included a representation of NFM. One exception is a previous study performed by our group [48], in which a neo-Hookean NFM term was incorporated in parallel with collagen networks in a multiscale model to simulate the mechanical behavior of decellularized arteries. The current study employs a modified version of our previous approach, but constructed more closely with experimental data and with a more specific focus on microstructural properties and relationships. Therefore, the purpose of this study was to apply a large-network-based modeling approach to experimental co-gel data to evaluate the role of non-fibrillar matrix and the nature of microstructural collagen-matrix interactions in soft connective tissues.

A.2 Methods

A.2.1 Material of Interest

A microscale model was developed for collagen-agarose co-gels, of which experimental data was presented previously [37]. Although the fabrication and testing of the gels are described elsewhere, a brief description is provided here as part of the development of the model. Collagen-agarose co-gels composed of 1.0 mg/mL collagen and 0% (NoAg), 0.125% (LoAg) or 0.25% (HiAg) w/v agarose were cast in dog-bone shaped Teflon molds (Figure A-1A) and allowed to gel. Agarose, which constituted the NFM of this tissue analog system, formed an interspersed, web-like matrix within the collagen network [37,196]. Co-gels were subjected to a four-step incremental stress-relaxation tensile test, wherein the load, tissue strain, and cross-sectional area were recorded
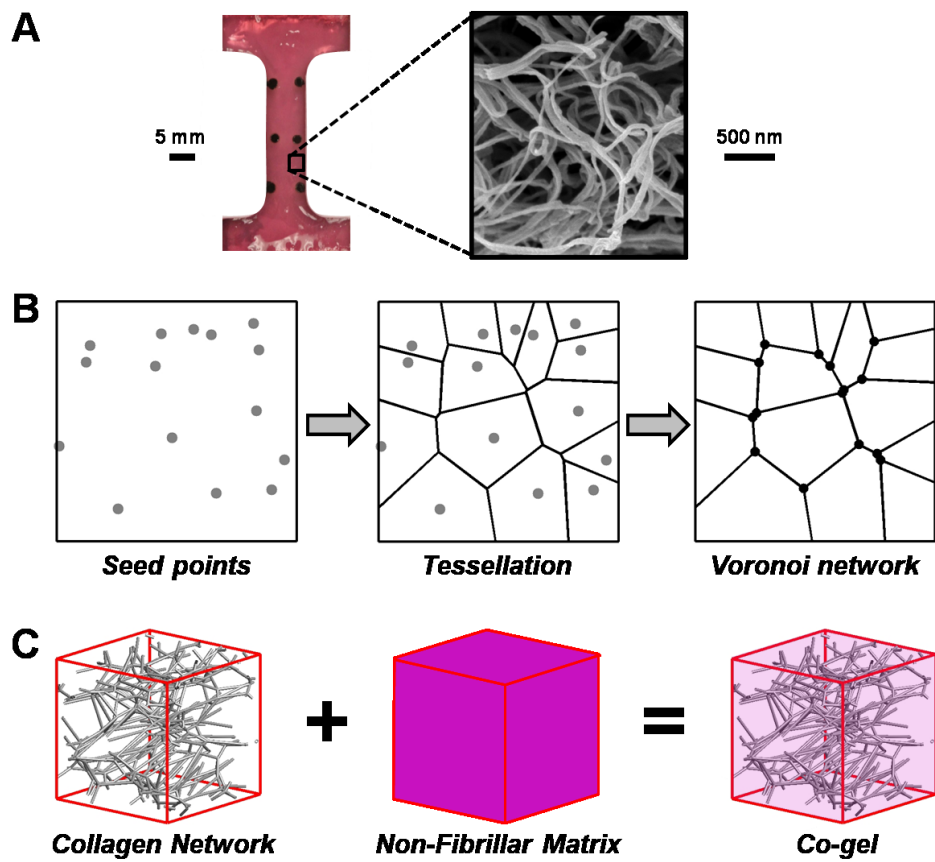
Figure A-1. A microscale network model was used to simulate the response of collagen-agarose soft tissue analogs. (A) Representative dog-bone shaped collagen gel tested experimentally[35] and scanning electron micrograph showing the reconstituted collagen network. (B) Computational networks were generated by randomly placing seed points within a representative volume element (RVE), generating a Voronoi tessellation about those seed points, and placing pin joint nodes at each fiber-fiber connection (schematic shows 2D network for clarity; actual Voronoi networks were 3D). (C) Collagen-agarose co-gels were modeled by adding the contributions from the collagen network and the non-fibrillar matrix in parallel.

throughout testing, and quantitative polarized light imaging (QPLI) was used to quantify collagen fiber alignment and kinematics. The present study focused on the equilibrium (relaxed) data from the final step of these tests, corresponding to ~10% tensile strain.

136

A.2.2 Model Formulation

While several different types of computational networks have been used to represent collagen (e.g., random growth [14,48], confocal microscopy reconstruction [107], scanning electron microscopy reconstruction [223]), Voronoi networks were used in this study. Such networks were recently shown to provide a close approximation to collagen gel behavior [80], and the sparse arrangement and low nodal degree of Voronoi networks allowed for generation of networks that exhibited very large Poisson's ratio values (~3) similar to those measured experimentally for our collagen-agarose co-gels [37]. Previous studies using other network types [39,167,207] have been unable to achieve Poisson's ratio values as large as those measured experimentally for tissue analogs, which are likely caused by significant network reorientation, compaction and densification of the network, and exudation of interstitial fluid. In the present study, networks were created by randomly placing seed points within a representative volume element (RVE), generating a 3D Voronoi tessellation about these points, and placing nodes at the intersections of Voronoi edges (Figure A-1B). Networks were created in Matlab (Natick, MA) using the VORONOIN function, an implementation of the widely-used Qhull code. In order to ensure that results were not dependent on a specific placement of seed points, five different networks were created and evaluated in this study (i.e., n=5 for each simulation group) with ~700 fibers per network. Using an assumed fiber diameter of 70 nm, collagen density of 1.34 g/mL, and the experimental collagen concentration (1 mg/mL), the average edge length in undeformed RVEs was computed [48] to be ~20 μm; consequently, average RVE volume was ~8,000 μm^3. Generated

Voronoi networks were isotropic, so a pre-stretch was applied along the x-axis, and the RVEs were clipped to the original size, such that initial network alignment approximated the anisotropic alignment of co-gels measured via QPLI. The number of seed points (and hence, number of fibers) was adjusted until the Poisson's ratio of stretched RVEs equaled values for NoAg gels. Nodes at fiber intersection points were modeled as freely rotating pin joints, and fibers were modeled as one-dimensional nonlinear springs, with the force on each fiber defined as [4,14,48,93,154]:

$$F = \frac{E_f A}{B}(e^{B\varepsilon} - 1) \tag{A-1}$$

where E_f is the elastic modulus of the fibers at infinitesimal strain, A is the fiber cross-sectional area, B is a nonlinearity constant, and ε is the fiber Green strain given by $\varepsilon = 0.5(\lambda_f^2 -1)$. Parameter values for the fiber constitutive equation were used as previously [14] (fiber radius=35 nm; B=3.8), where the fiber modulus value E_f was set at 6.5 MPa in order to produce total stress values (calculated as defined below) approximately equal to experimentally-measured values for the NoAg group. With the fiber forces thus defined, the volume-averaged Cauchy stresses from the collagen network at each RVE surface were computed by [38,39]:

$$\sigma_{ij}^{col} = \frac{1}{V} \sum_{bnd\ nodes} x_i F_j \tag{A-2}$$

with V as the RVE volume and x_i corresponding to the position of each fiber (with force F_j) on a given RVE boundary.

As done in our previous study [48], the non-fibrillar matrix (NFM) was represented using a compressible neo-Hookean solid formulation. Assuming no shear, Cauchy stress due to the NFM was defined as [108]:

$$\sigma^{nfm} = G\left(\frac{\lambda^2}{J} - J^{-2\beta-1}\right) \tag{A-3}$$

where G is the NFM shear modulus, λ is the RVE stretch, J is the Jacobian, $\beta = v_m/(1-2v_m)$, and v_m is the Poisson's ratio of the matrix. Since the model represents the mechanical response at equilibrium (after relaxation and drainage of any pressurized interstitial water), v_m was taken to be 0.1 [109]. Values for G were specified by extrapolating experimental data for the shear modulus of pure agarose gels [110] to concentration values used in our study such that $G = 0$, 110 and 720 Pa for NoAg, LoAg, and HiAg, respectively. In this way, the only difference between models representing the three experimental groups was in the specific value used for shear modulus. All other variables (e.g., organization of the Voronoi collagen network, parameter values for the fibers) were consistent across the three different co-gel models. The total stresses in the composite model were calculated by summing the contributions from the collagen network and the NFM (Fig. 1C) in a parallel manner:

$$\sigma^{tot} = <\sigma^{col}> + \sigma^{nfm} \tag{A-4}$$

A.2.3 Model Solution

A 10% strain was applied to each RVE in the 1-direction (λ_1=1.1), while the 2- and 3-directions had stress-free surfaces (Figure A-2). After the step displacement, the position of the internal nodes and the position of the unloaded boundaries (2- and 3-faces) were solved for using Newton's method to ensure force balance at each internal node and

139

1. Apply displacement

$\lambda_1 = 1.10$

2

1   3

2. Iterative minimization

Adjust position of internal nodes

Tolerance reached?

$$\sum_{\text{internal nodes}} F_{ij} = 0$$

Iterate

$\sigma_{22}^{nfm} + \langle\sigma_{22}^{col}\rangle = 0$

$\sigma_{33}^{nfm} + \langle\sigma_{33}^{col}\rangle = 0$

*Adjust position of 2- and 3-faces*
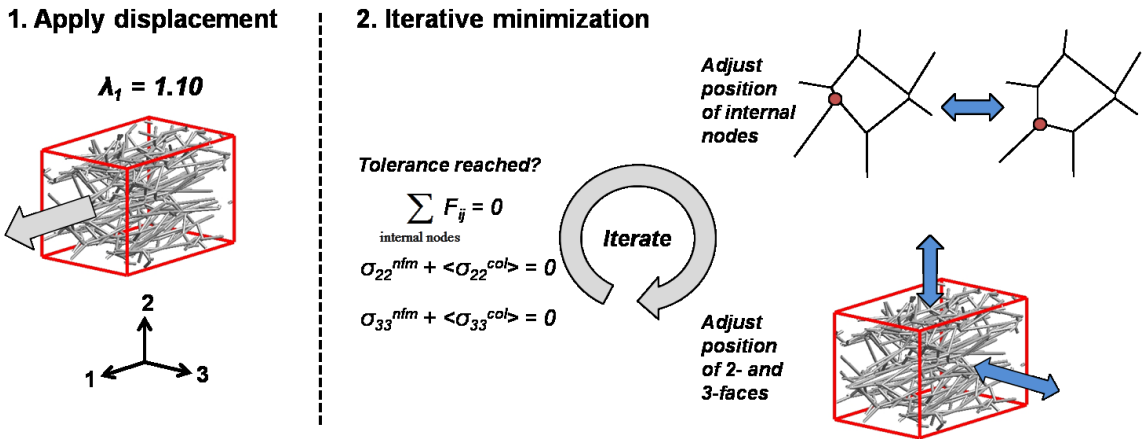
Figure A-2. After applying a stretch of 1.1 in the 1-direction, an iterative minimization scheme adjusted the position of the internal nodes and of the 2- and 3-direction surfaces until a tolerance was reached for the nodal force balance and stress-free boundaries.

minimal normal stresses on the free surfaces (i.e., σ_{22} and σ_{33}; Figure A-2). For all three groups (NoAg, LoAg, HiAg), simulations were evaluated for each of the five networks. For each run of the microscale model, the total normal stress in the loaded direction (σ_{11}) and the Poisson's ratio of the composite RVE were computed and compared to experimental co-gel data. In addition, the stresses due to each component ($\langle\sigma_{11}^{col}\rangle$, σ_{11}^{nfm}) and the amount of stretch on each fiber (λ_f) were evaluated along with 3D maps showing network orientation and fiber stretch. All model simulations were performed in Matlab, with a run time of a few minutes.

A second set of simulations was performed to explore the parameter space of the NFM neo-Hookean term. To characterize the parameter space, the shear modulus and Poisson's ratio were varied across a range of values ($G = 1, 10, 110, 330, 720, 1310$ Pa; $\nu = 0, 0.05, 0.1, 0.15, 0.2, 0.25, 0.3, 0.35, 0.4, 0.45, 0.49$), and RVEs were evaluated for each combination of parameter values.
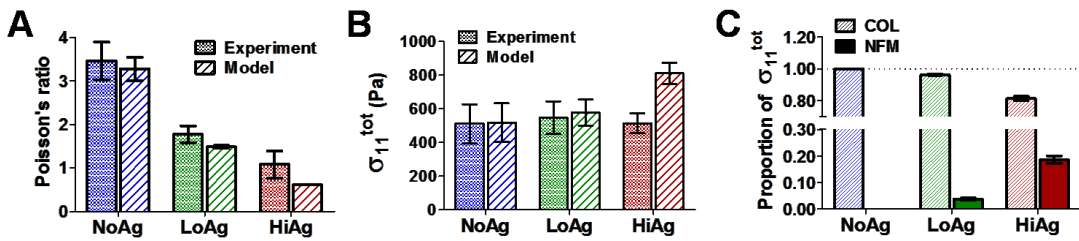
Figure A-3. Model-predicted values of (A) Poisson's ratio and (B) Cauchy stress in the 1-direction showed qualitative comparison with experimental values; (C) while stress in the NoAg samples was due (trivially) to collagen (COL) alone, the non-fibrillar matrix (NFM) contributed a small and moderate proportion of the total stress to the LoAg and HiAg groups, respectively (plots show mean ± 95%CI; n=5-7/group).

A.2.4 Statistical Analysis

A one-way ANOVA was utilized to compare mean fiber stretches across groups and post-hoc *t*-tests were used to identify statistically significant specific comparisons. Bonferroni corrections were applied when making multiple comparisons.

A.3 Results

The model-predicted values of Poisson's ratio and total stress (in the 1-direction) compared well with experimental values (Figure A-3A and Figure A-3B, respectively). Data trends showed qualitative agreement, indicating that the microscale model made good, if not exact, predictions of the experimental data. An examination of the relative proportion of the total stress contributed by each component (Figure A-3C) yielded a very small NFM contribution in the LoAg samples (average = 3.8% of total stress), and a larger NFM contribution for the HiAg samples (average = 18.6% of total stress).

Representative network maps at 10% strain showed that fiber orientation and fiber stretch varied significantly across different groups (Figure A-4). In these plots, gray fibers are unstretched relative to the undeformed case ($\lambda_f = 1$), red fibers are in tension ($\lambda_f > 1$), and blue fibers are in compression ($\lambda_f < 1$). As the amount of NFM increased (from
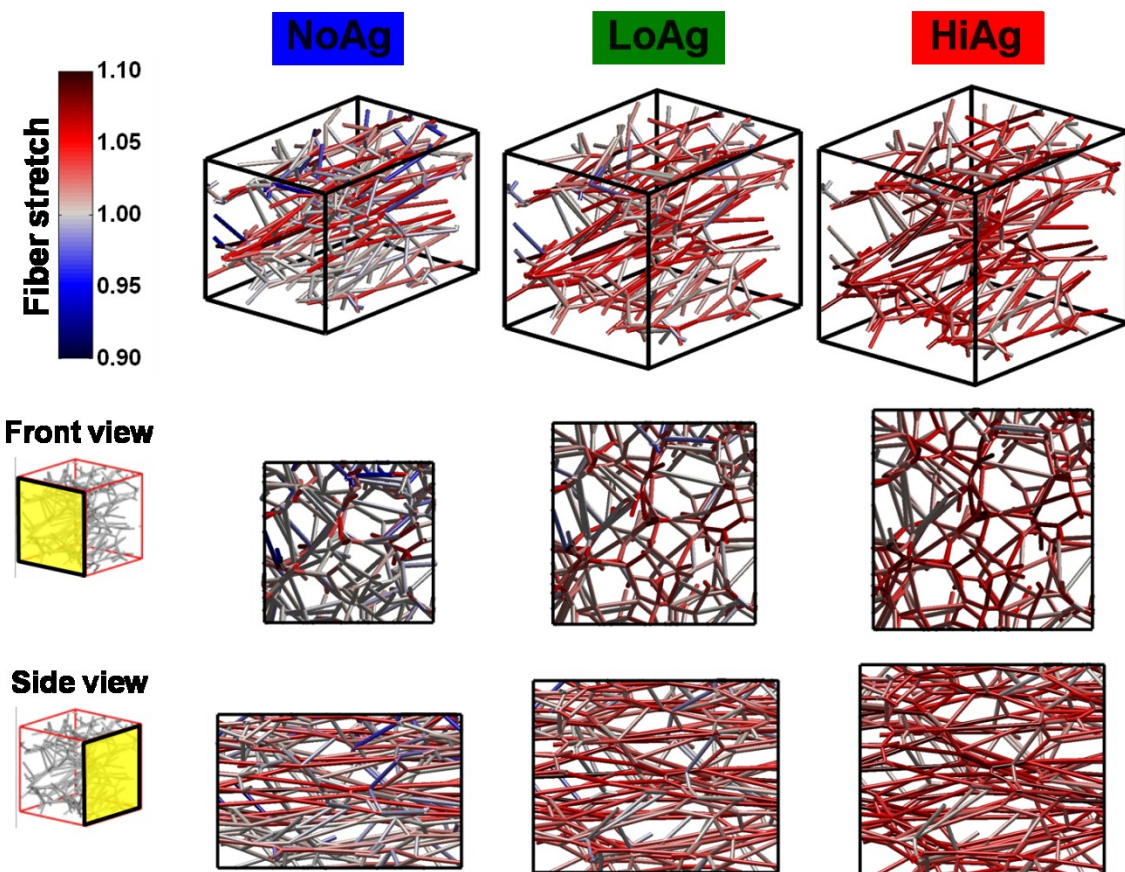
Figure A-4. 3D maps (and 2D projections) show how network organization and fiber stretch for a representative network changed as a function of NFM quantity: the amount of network compaction decreased and relative fiber stretch increased as NFM increased from NoAg to LoAg to HiAg (gray = unstretched relative to undeformed case, red = tensile stretch, blue = compressive stretch).
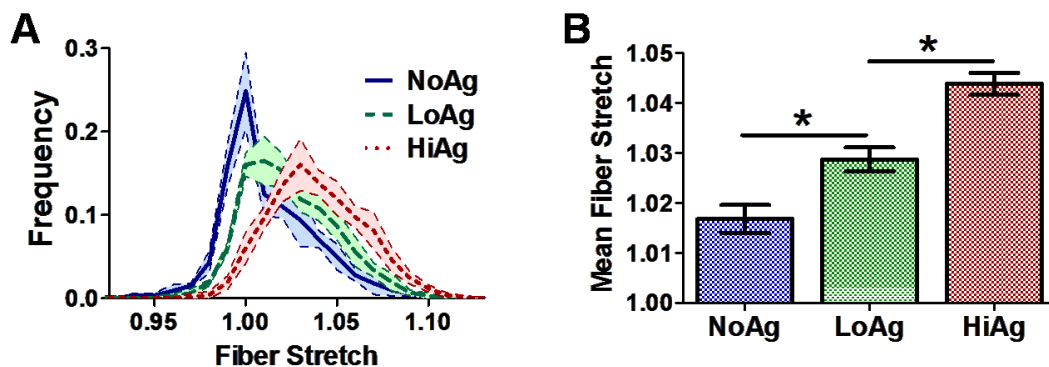

Figure A-5. Fiber stretch increased with increasing NFM composition, as demonstrated by (A) frequency distribution curves and (B) mean fiber stretch values (mean± 95%CI; n=5/group; * = significant differences).
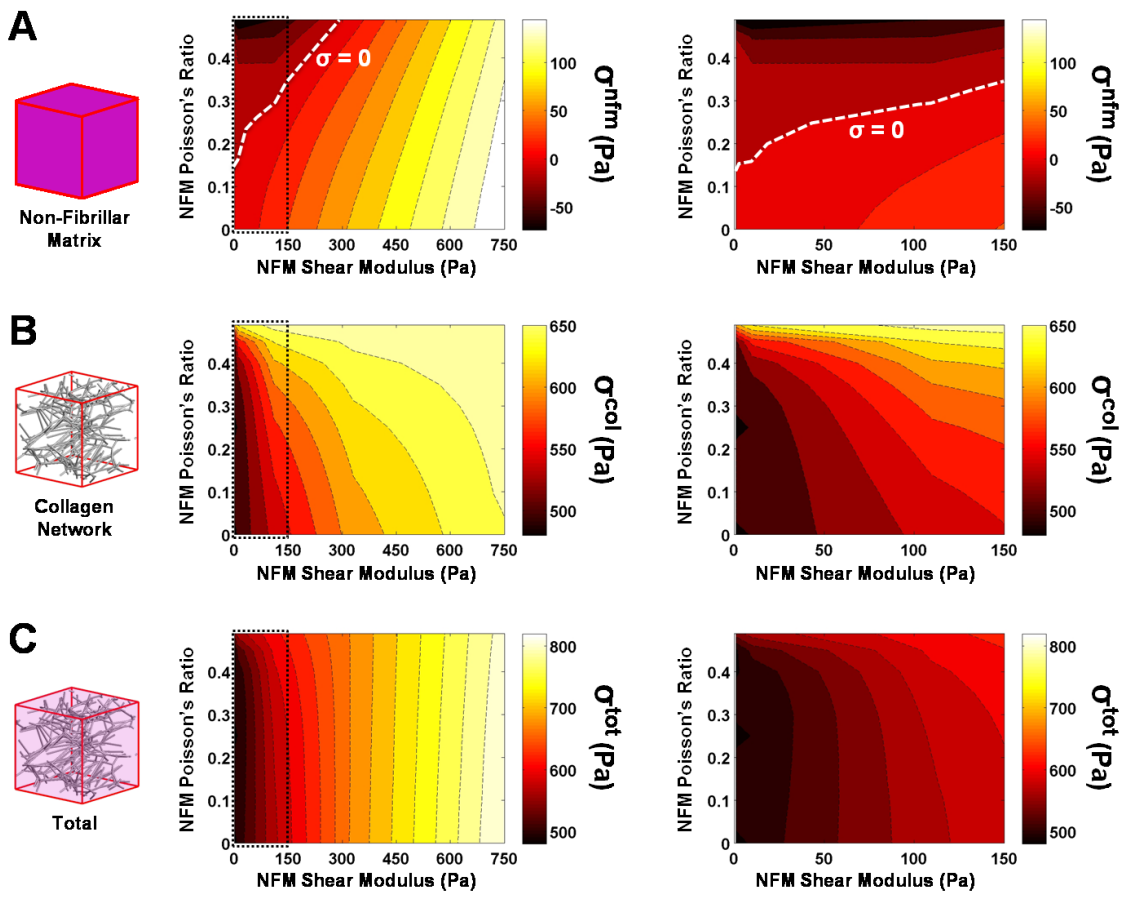
Figure A-6. Parameter space plots demonstrate how the (A) NFM stress, (B) collagen stress and (C) total stress changed as a function of varying the two NFM input parameters of shear modulus and Poisson's ratio (left = full parameter space; right = zoomed in low shear modulus region); of particular interest was the span of the NFM stress from negative to positive values, including the boundary (dashed line) where the contribution from the NFM was zero (mean values plotted; n=5/group).

NoAg to LoAg to HiAg), the number of blue and gray fibers decreased and the intensity

of red fibers increased, demonstrating an overall increase in fiber stretch due to the NFM.

Fiber stretch was also evaluated quantitatively by comparing frequency distributions

(Figure A-5A) and mean fiber stretch values (Figure A-5B), where significant differences

were observed between the groups ($p<0.001$). Another observation from the network

maps was the difference in volume change due to the presence/quantity of NFM; NoAg

RVEs compacted significantly in the lateral directions, while the HiAg RVEs strongly
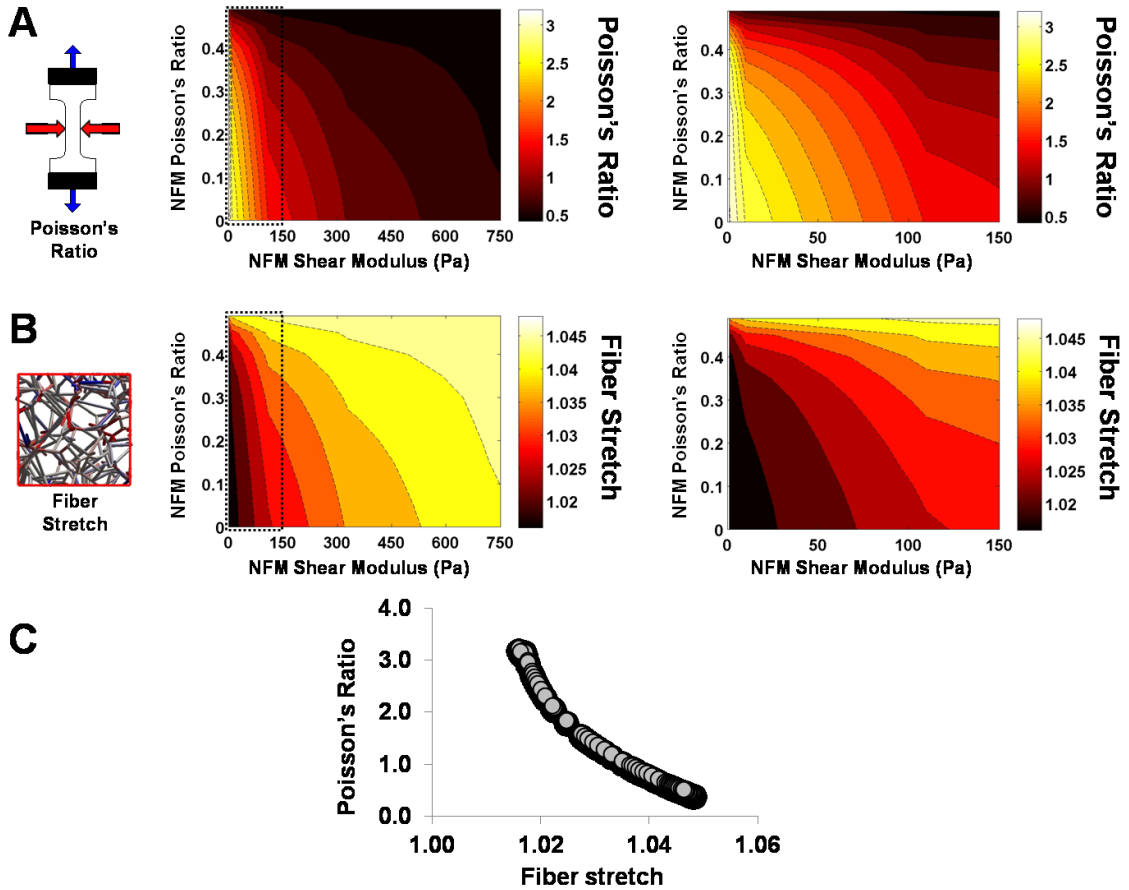
Figure A-7. Parameter space plots demonstrate how the (A) RVE Poisson's ratio and (B) fiber stretch changed as a function of varying the two NFM input parameters of shear modulus and Poisson's ratio (left = full parameter space; right = zoomed in low shear modulus region; mean values plotted; n=5/group); (C) there was a strong correlation between Poisson's ratio and fiber stretch values.

resisted volume change (Figure A-4). Importantly, the NFM's resistance to volume change (also demonstrated by decreasing Poisson's ratio) likely resulted in the increased fiber stretches by not allowing the fibers to reorient in the direction of loading and compact the lateral boundaries.

Parameter space plots (Figure A-6 and Figure A-7) demonstrate how output values changed as a function of the two parameters in the neo-Hookean NFM term (Poisson's ratio v_m and shear modulus G). Interestingly, at low G values and moderate v_m values, the NFM stress (σ^{nfm}) was negative (Figure A-6A), indicating a compressive stress

144

contribution from the NFM. With this transition from compressive to tensile stress, the parameter space for σ^{nfm} included a boundary along which the stress contribution from the NFM was zero (dashed line, Figure A-6A). The collagen network stress (σ^{col}) and the total stress (σ^{tot}) increased with increasing G (Figures A-6B and A-6C, respectively). For all stress measures, increasing the value of v_m had minimal impact at high G, but made a more significant impact at low values of G (Figure A-6, right column). In a similar manner, parameter maps for RVE Poisson's ratio and fiber stretch (Figures A-7A and A-7B, respectively) demonstrated relatively consistent values when $G>300$ Pa, but much greater variation in values at low G. As Poisson's ratio of the NFM (v_m) increased, the composite Poisson's ratio decreased and λ_f increased. Furthermore, there was an inverse relationship between RVE Poisson's ratio and mean fiber stretch (Figure A-7C).

A.4 Discussion

In this study, a network-based microscale model was developed and fit to experimental data from collagen-based tissue analogs. After adding (in parallel) a term to describe the mechanical contribution from the non-fibrillar matrix (NFM), the model was able to predict qualitatively the composition-dependent mechanical response of collagen-agarose co-gels in tension (Figures A-3A and A-3B). The microscale model utilized here allowed for the characterization of how the collagen fiber network (represented via Voronoi networks) was reoriented and stretched differentially as a function of increasing NFM.

Our experimental studies of collagen-agarose co-gels [37,111] suggested that agarose served a volume-preserving role in co-gel deformation. Similarly, the neo-

Hookean term representing the NFM contribution in our microscale model increased resistance to volume change. Specifically, lateral compaction in the 2- and 3-directions that occurred during a stretch in the 1-direction decreased as a function of NFM concentration, as measured by average Poisson's ratios from model simulations (Figure A-3A) and by comparing deformed dimensions of representative network maps (Figure A-4). As lateral compaction decreased, the reorientation of the fibers towards the direction of loading was limited, leading to increased stretching of the fibers (Figures A-4 and A-5). In fact, further simulations yielded data that showed a distinct correlation between Poisson's ratio of the RVE and mean fiber stretch (Figure A-7C). Parameter space plots show how these measures changed as parameter values for the NFM term (shear modulus G and NFM Poisson's ratio v_m) were varied across a full range of values (Figures A-7A and A-7B). At high G (~400 Pa and above), RVE Poisson's ratio and fiber stretch remained relatively consistent, even when v_m was varied significantly; however, at low G these values were highly dependent on changes in G and v_m.

The stress contribution due to the NFM was computed as predicted for the three sample groups: while trivially zero for the NoAg samples, the NFM stress was very small for the LoAg samples and moderate for the HiAg samples (Figure A-3C). Further exploration of the neo-Hookean NFM parameter space demonstrated a transition to negative (compressive) stress for the matrix at low shear modulus and moderate Poisson's ratio (Figure A-6A). Although a compressive state in the unloaded (2- and 3-) directions is intuitive (in opposition to the collapsing collagen network due to the Poisson effect), a compressive NFM stress in the 1-direction is somewhat unexpected. Such a

146
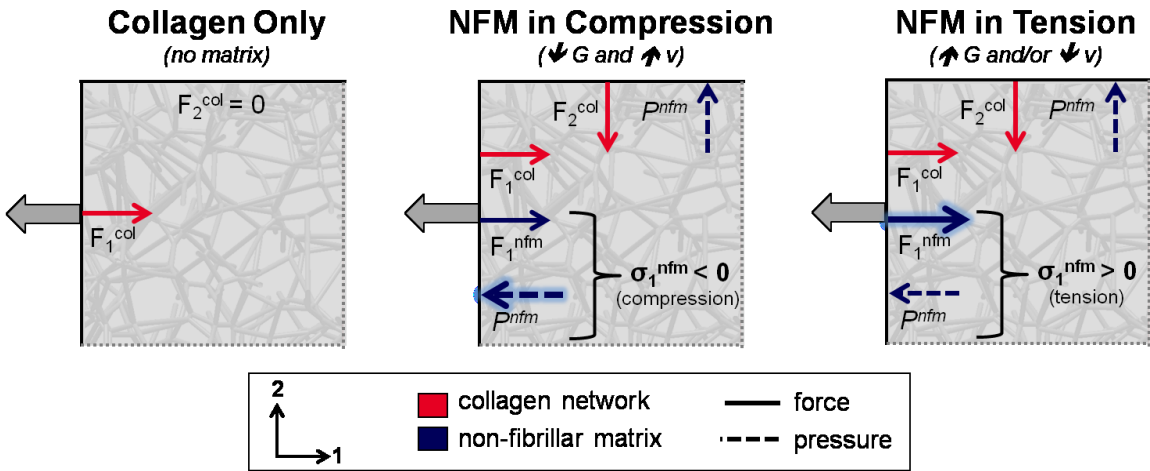
Figure A-8. 2D schematic demonstrating the proposed mechanism for the observed results. In the collagen-only (NoAg) case (left), collagen provided a reaction force (F_1^{col}) while the forces on the non-loaded boundary were zero. At low shear modulus and high Poisson's ratio (middle), the pressure due to the NFM resisting volume change (P^{nfm}) was greater than the NFM reaction force (F_1^{nfm}), resulting in a negative (compressive) stress from the NFM. At high shear modulus and/or low Poisson's ratio (right), the NFM reaction force (F_1^{nfm}) dominated over the pressure term (P^{nfm}), resulting in a positive (tensile) stress from the NFM.

result indicates that, instead of providing a reaction-force-type response to the deformation (as the collagen network does), the NFM force acts in the direction of the grip and decreases the magnitude of the composite tensile stress. While this notion is initially counterintuitive, previous computational studies [198,199] have demonstrated a similar result for the hydrostatic pressure term in a fiber-based incompressible model, and our experimental co-gel data [37] suggested this possibility since peak stress values decreased with increasing amounts of NFM (i.e., agarose). In addition, our previous fiber-matrix multiscale model of artery mechanics [48] predicted that the non-collagenous matrix would be in compression in order to prevent the collapse (i.e., lateral compaction) of the collagen network. Thus, a compressive NFM stress in the loading direction due to pressurization of the composite material is plausible at certain parameter values of the NFM component.

A possible mechanism for compression of the NFM, and for how the NFM transitions to a tensile stress at different parameter values, is represented using a simple schematic (Figure A-8). For simplicity, a 2D representation of the 3D physical system is used. When collagen-only (NoAg) samples are stretched (Figure A-8A), the collagen provides a reaction force (F_1^{col}) in resistance to the deformation in the 1-direction, while the stress-free 2-boundary exhibits no net force (i.e., F_2^{col} =0). When added to the collagen network, NFM contributes to the composite mechanical response in two ways (Figure A-8B): through a reaction force (F^{nfm}) that resists deformation and through an isotropic pressure (P^{nfm}) that resists volume change. The presence of P^{nfm} balances the transverse tension in the collagen network F_2^{col} to help maintain volume and satisfy the zero total stress condition on the 2-boundary. In samples with small shear modulus (G) and moderate to high Poisson's ratio (v_m) values (Figure A-8B), F_1^{nfm} is relatively small because of low G, so P^{nfm} dominates, resulting in a negative (i.e., compressive) total stress from the NFM (σ_1^{nfm}). On the other hand, at large G and/or small v_m (Figure A-8C), the high shear modulus increases the magnitude of F^{nfm} over that of the P^{nfm}, resulting in a positive (i.e., tensile) total σ_1^{nfm}.

Collagen-based tissue analogs and some collagenous native tissues (e.g., tendon and ligament) can exhibit very high Poisson's ratio in uniaxial tension experiments [37,175,224,225]. Poisson's values as high as 2-3 are due to a high degree of network reorientation towards the loading direction [37,226], significant compaction and densification of the network due to fibers buckling under transverse strain [205], and significant exudation of interstitial fluid [227,228]. Although one recent study presented

148

a micromechanical finite element model that was able to predict high Poisson's ratios using crimped fibers in a super-helical organization [229], previous regular-fiber-cell and large-network models have only been able to achieve maximum Poisson's ratio values of ~1 [39,167,207], thereby failing to replicate the high values measured experimentally [107,167]. Voronoi networks, which were previously reported to show quantitative agreement to collagen networks [80], contain fewer fiber-fiber crosslinks than other network types used in previous models, thereby allowing for greater fiber reorganization and subsequent network compaction under load. In the present study, Voronoi networks representing the collagen-only gels exhibited Poisson's ratios of ~3 in agreement with experimental data.

One difficultly in extending this modeling approach towards characterizing native tissues is identification of an appropriate mathematical formulation and corresponding material properties for the non-fibrillar matrix (NFM). As in several previous studies [48,93–97,109,201], the current work represented the NFM using a simple neo-Hookean solid with two input parameters: shear modulus and Poisson's ratio. The model was compared to experimental data at the equilibrium phase of a stress-relaxation test, so a low Poisson's value of 0.1 was used [109]. In addition, since the model was constructed to represent collagen-agarose co-gels, values for the shear modulus were based on properties of agarose-only gels tested experimentally [110], which are comparable to those used in other tissue modeling studies [93,94,200,219]. For native tissues, defining these parameters is more difficult because the NFM term, as presently defined, lumps all non-collagenous material together (i.e., there is no single definition of NFM), making

tissue-specific definition of these parameters challenging, and the experimental measurement of NFM properties very difficult. Certainly this topic merits further investigation.

This study is not without limitations. Due to the parallel construction of the microscale model, our approach did not allow for examination of fiber-matrix interactions internal to each RVE, which likely result in a heterogeneous strain and stress fields throughout the sample. Ongoing work by our group is developing a coupled fiber-matrix microscale model that will allow for characterization of these internal interactions. Another difficulty lies in appropriately matching the initial fiber orientation of the Voronoi networks to experimental data. We used a method described previously [14] to match 3D network organization to the 2D experimental measures of sample alignment (using polarized light imaging), but the appropriate definition for the proportionality constant used in this analysis remains unclear. In spite of these concerns, the model developed and used in this study matched experimental observations well and demonstrated a mechanism by which pressurization of the NFM reduces lateral contraction of the collagen network and leads to a negative (compressive) stress in the NFM (σ_{11}^{nfm}) even though the composite tissue is in tension.